universität wien

MASTERARBEIT / MASTER'S THESIS

Titel der Masterarbeit / Title of the Master's Thesis

Investigating Alkali Borate Glasses via Total X-ray Scattering

verfasst von / submitted by

Katharina Holzweber, BA, BSc

angestrebter akademischer Grad / in partial fulfilment of the requirements for the degree of

Master of Science (MSc)

Wien, 2017 / Vienna 2017

Studienkennzahl lt. Studienblatt / degree programme code as it appears on the student record sheet:	A 066 876
Studienrichtung lt. Studienblatt / degree programme as it appears on the student record sheet:	Masterstudium Physik
Betreut von / Supervisor:	ao. Univ.-Prof. Mag. Dr. Bogdan Sepiol

Abstract

Within the scope of this thesis the structure of alkali borate glasses is investigated by total scattering experiments. Different approaches in sample preparation, experimental setups and evaluation procedures are tested and the results are compared.
In the first chapter an introduction into the current state of research is given where results both from experiments and computer simulations are considered. In contrast to previous works which focused on selected alkali oxides or concentrations this work analyzes and compares the whole range of alkali oxides with different concentrations, starting from lithium oxide to caesium oxide.
A comprehensive theoretical background about polyatomic systems regarding the structure factor and the partial distribution function is provided in the second chapter together with a short introduction into X-ray diffraction theory. The former is required for an optimal application of the evaluation program PDFgetX and a correct analysis of the experimental results.
Additionally, it is pointed out that without the support of numerical simulations, a complete deciphering of polyatomic systems consisting of several partial structure factors and pair distribution functions is impossible or at least very elaborate, by experimental means. Nonetheless, one can still determine the alteration of the alkali borate structure with respect to interatomic distances and coordination numbers for different alkali concentrations or alkali types.
Some deficits of the highly automatable successor program PDFgetX3 for the evaluation of alkali borate glasses were shown and documented in detail.
The manufacturing process of alkali borate glasses and the preparation of thin platelets and powder samples are precisely explained in the chapter about the experimental approach. Due to the hygroscopic nature of alkali borate glasses which leads to crystallization on the surface, the usage of platelets is advantageous due to their small surface-area-to-volume ratio.
In the last chapter the results of the measurements at Petra III at the Deutsches Elektronensynchrotron (DESY) in Hamburg and at the Empyrean PANalytical X-ray diffractometer at the TU Wien were analyzed.
The profound structural analysis of alkali borate glasses, which is provided by this Master's thesis, is a good basis for further investigations concerning diffusion processes within these materials via X-ray photon correlation spectroscopy measurements.

Zusammenfassung

Diese Arbeit beschäftigt sich mit der Struktur von Alkaliboratgläsern, die mittels Röntgendiffraktometrie untersucht wurden.
In der Einleitung wird auf vorangegangene experimentelle als auch numerische Erkenntnisse bezüglich der Struktur von Alkaliboratgläsern eingegangen. Im Gegensatz zu vorhandenen Publikationen versucht diese Arbeit die ganze Bandbreite an Alkalioxiden, von Lithiumoxid bis Cäsiumoxid, mit verschiedenen Konzentrationsgehalt zu analysieren und zu vergleichen. Für eine optimale Auswertung mit dem Programm PDFgetX und einer korrekten Analyse der Messergebnisse bedarf es einer umfassenden Kenntnis über polyatomare Systeme und deren Strukturfaktoren und Paarverteilungsfunktionen, welche im Theorieteil Einzug finden.
Im Theorieteil wird besonders darauf Aufmerksam gemacht, dass ohne Unterstützung von Simulationen eine komplette Bestimmung polyatomarer Strukturen, die aus mehreren partiellen Strukturfaktoren und Paarverteilungsfuntkionen bestehen, experimentell nicht (oder nur sehr aufwendig) möglich ist. Nichts desto trotz lässt sich das Verhalten der Struktur im Bezug auf atomare Abstände und Koordinationszahlen bei Änderung des Alkalianteils bzw. des Alkalityps bestimmen.
Durch die intensive Beschäftigung mit den Auswertungsprogrammen PDFgetX2 und dessen Nachfolgerversion PDFgetX3 sind einige Defizite des hoch-automatisiereten Nachfolgerprogramms PDFgetX3 für die Auswertung von Alkaliboratgläsern ans Tageslicht gerückt, die ebenfalls in einem Kapitel dokumentiert wurden.
Das Herstellungsverfahren von Alkaliboratgläsern und die Präparation der Proben in Form von Pulver und dünnen Plättchen wird im experimentellen Teil genau erläutert. Da Alkaliborate hygroskopische Eingeschaften besitzen und sich kristalline Strukturen an der Oberfläche bilden, erweist sich die Probe in Form von einem Plättchen mit geringer Oberfläche im Verhältnis zum Volumen als geeigneter für die experimentelle Durchführung.
Im Kapitel der Diskussion und der Resultate werden die Messergebnisse von Petra III des Deutschen Elektronensynchrotrons in Hamburg und vom Empyrean PANalytical Röntgendiffraktometer an der TU Wien analysiert.
Die umfassende Strukturanalyse von Alkaliboratgläsern, die diese Arbeit zur Verfügung stellt, bietet die Grundlage für weitere Röntgenphotonenkorrelationsspektroskopie-Messungen zur Untersuchung von atomren Diffusionsprozessen in diesen Gläsern.

Motivation

Ion-conducting materials have a high technological potential for electrochemical devices such as solid-oxide fuel cells, solid-state batteries or chemical sensors [2]. In the contrast to conventional liquid lithium-ion-batteries, these materials have a low self-discharge, a fast load capacity, a high stability, a high energy density and a reasonable and easy producibility[3].
However, the biggest deficit is the low ionic conductivity, which corresponds to a low power density and is currently a hindrance for economic and industrial applications. In alkali-borate glasses the ion-conductivity is strongly correlated with the surrounding structure, which motivates for a complete understanding of all the structural properties of the material with the goal to enhance the ionic mobility.

Contents

Chapter 1

Introduction

1.1 The structure of glass

Glass is described as an amorphous material made from a liquid via sufficiently rapid cooling below the "glass transition temperature" T_g to prevent crystallization [10]. Consequently, glass lacks the long-range order but with a nonzero shear rigidity [30]. In contrast to a general opinion that glasses are randomly arranged, there exists a short-range and even an intermediate-range order in vitreous materials [16].
The short-range order defines the local structure; for instance, one silicon atom is surrounded by four oxygen atoms in SiO_2 glas. It provides information about the nearest neighbours, forming the so-called first coordination shell.
The intermediate-range order is related to the second or higher order coordination shell structure, which is in the range from 1 nm to 10 nm scale. The short-range as well as the intermediate-range order can be detected by neutron or X-ray scattering. But also Raman scattering, EXAFS[1], XANES[2], NMR[3], and infrared spectroscopy are suitable experimental methods.

1.2 The structure of borate glasses

Borate glasses are present in almost all commercially important glasses and are used as dielectric and insulating material. It is known that borate is a good shield against infrared radiation. They are also used as electro-optic modulators, electro-optic switches, solid-state laser materials, non-linear optical parametric converters and thermoluminescence dosimetry devices [18].
Borate glasses are one of the most studied and best understood network glasses. X-ray and neutron scattering studies as well as computer simulations like the Molecular Dynamics (MD) method indicate the existence of a short- and intermediate range order in the vitreous B_2O_3 structure (see figure 1.1).

In crystalline boron oxides, the boron atom is found in triangular coordination

[1] Extended X-ray Absorption Fine Structure
[2] X-ray Absorption Near Edge Structure
[3] Nuclear Magnetic Resonance

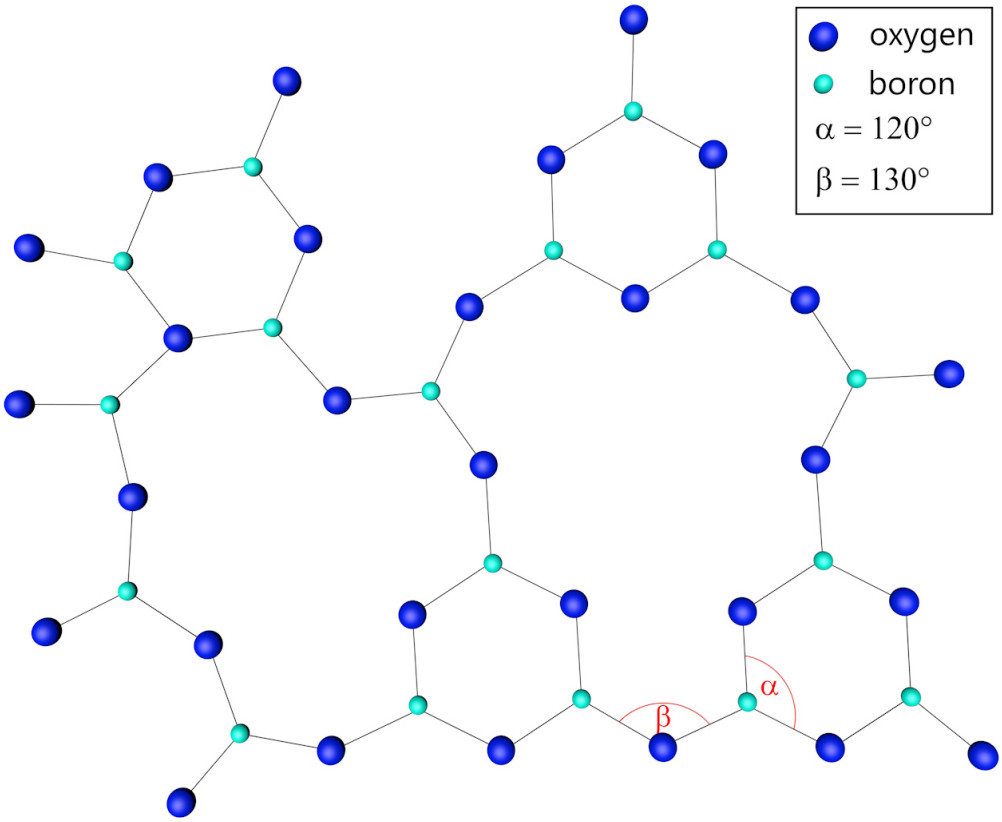

Figure 1.1: Two-dimensional representation of a random network model of vitreous B_2O_3. Boron and oxygen atoms are alternately arranged forming triangular coordinated structures (BO_3) and boroxol rings (B_3O_6), which are linked by shared oxygen atoms.

(one boron atom surrounded two-dimensionally by three oxygen atoms, which corresponds to a sp^2 hybridisation) with an average distance of
B-O=1.35 Å, and in tetrahedral coordination (one boron atom surrounded three-dimensionally by four oxygen atoms) with an average B-O distance of 1.44 Å [14]. In vitreous B_2O_3 the triangular coordination predominates and the interatomic B-O distance for triangles equals to 1.37 Å. For tetrahedrons the B-O distance also increases slightly to 1.47 Å [21]. The triangular coordination is visible in figure 1.2 (a) and the tetrahedral coordination in figure 1.2 (b).
75-80% of boron atoms are part of boroxol rings B_3O_6, which are representative for an intermediate-range order [12]. Boroxol rings are hexagonal structures of three boron atoms and three oxygen atoms connected with three corner oxygen atoms outside the ring (see figure 1.2 (c)).

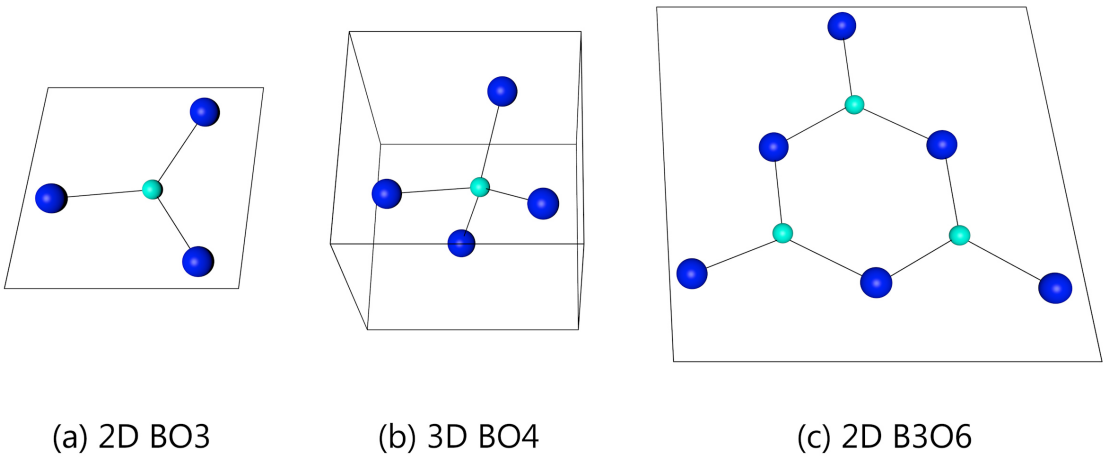

Figure 1.2: Three possible structures, which are responsible for the short- and intermediate-range order in B_2O_3: (a) The two-dimensional triangle, (b) the three-dimensional tetrahedron and (c) the two-dimensional boroxol ring.

MD simulations using simple pair potentials, however, could not reproduce the presence of B_3O_6 rings in borate glasses. In 1992 A.H. Verhoef and H.W. den Hartog added a three-body interaction potential, which was able to imitate the experimental data very well, in particular atomic distances and bond angle distributions. However, they also did not find any evidence of boroxol rings [27], which could be distinguished by a boron-oxygen next-nearest neighbour distance BO(2) of approximately 2.8 Å and distinct peaks of the pair distribution function (PDF) at distances out to about 6 Å. Later MD simulation methods using four-body potentials as well as polarizable bond charge models were able to demonstrate the formation of boroxol rings albeit at significantly lower concentration levels than were observed in experiments [12]. More recently energy minimization studies combined with the *ab initio* MD simulation method successfully reproduced the structure of borate glasses with the expected concentration of B_3O_6 groups [25], which is necessary in order to explain the intermediate-range order features and the proper density of B_2O_3 glass.
In contrast to vitreous B_2O_3, there is a total absence of boroxol rings within crystalline B_2O_3 materials. This interesting difference is believed to be responsible for the stability of vitreous B_2O_3. For crystal transformation the glass would require significant structural rearrangement demanding high energies [12].
The two-dimensional BO_3 and B_3O_6 molecules in vitreous boroxide glasses share one oxygen atom with each other (bridging oxygen) and have a complete randomness in orientation leading to the extension in three dimensions. The OBO-angle within a ring or a three-folded BO_3 arrangement is about 120°, whereas the BOB-angle between connected molecules is about 130° (see figure 1.3). Not every oxygen atom serves as a conjunction. There are also nonbridging oxygens (NBOs),which break the chain of connected molecules within the structure. There is only a small probability in vitreous boron oxide that one could cover a 10 Å interatomic distance by an unbroken path of B-O and O-B bonds, which is responsible for a low viscosity [21]. The bonding itself is largely of covalent nature, which is in agreement with the observed bond angles. This fact could later on lead to the question of the justification

of using atomic scattering factors, which are based on the assumption of a spherically symmetrical charge distribution. Due to the complete random orientation of the structure in vitreous B_2O_3, it is probable that the difference is not large enough to be important [21].

Table 1.1 shows a comparison between different evaluation methods regarding the interatomic distances.
A simple geometrical calculation needs fix starting values as the bond length of BO(1), the OBO-angle, the BOB-angle and a randomly chosen geometrical configuration, which is displayed in figure 1.3. Due to the amorphous feature of borate glasses the pair distribution functions (PDF) from experiments and simulations show kind of Gaussian distributions around these assumed interatomic distance values r_{max}. As expected there are growing discrepancies between the calculated interatomic distances from one random geometrical arrangement compared with the interatomic distances from experiments or simulations, where expectation values from many different arrangements are used.
The MD simulation data of sample number 3 were taken from [27], which used an additional OBO three-body interaction potential. The experimental data were taken from [21], which were obtained by the fluorescence excitation method. When there is no distinct peak found at the PDF for a certain distance, it is tabulated by a hyphen. The geometrical distance between two nearest boron atoms, BB(1), would be 2.37 Å for an angle of 120° and 2.48 Å for an angle of 130°. The PDF is not able to dissolve these values into two distinct peaks, hence it is more useful to take the average value.

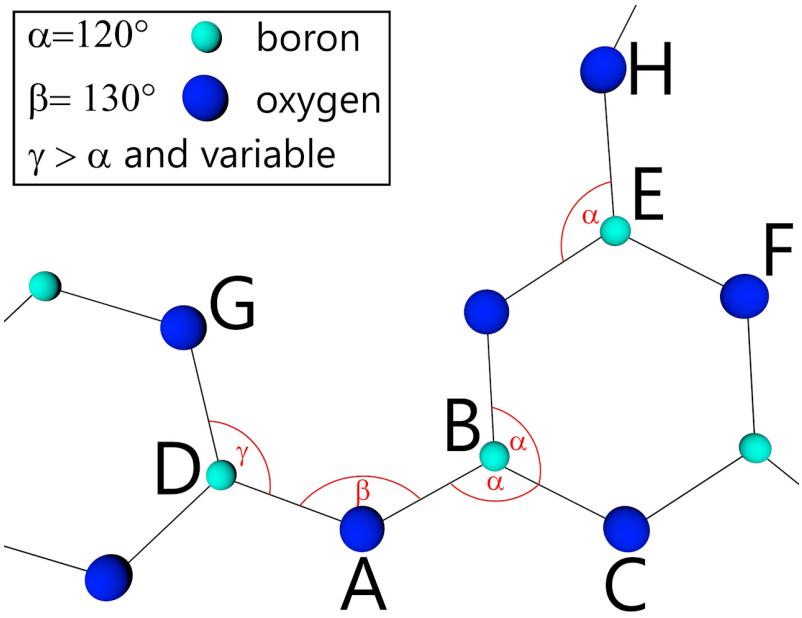

Figure 1.3: Two boroxol groups which are linked by a shared oxygen. There is random orientation around the γ angle which is placed between the points A, D and G. This specific geometrical configuration is the basis for the calculation of the interatomic distances shown in table 1.1.

atomic pair distances	Notation from figure 1.3	distances from figure 1.3 [Å]	r_{max} from experiment[Å]	r_{max} from MD simulation [Å]
BO(1)	A-B	1.37	1.37	1.37
OO(1)	A-C	2.37	2.40	2.37
BB(1)	B-D/B-E	2.43	2.48	2.67
BO(2)	A-E	2.74	2.70	-
BO(3)	B-G	variable	3.15	-
BO(4)	B-H	3.63	3.65	3.60
OO(2)	C-H	4.11	-	-
OO(3)	C-G	variable	4.3	4.5
OO(4)	A-H	4.75	4.70	-
BO(5)	D-F	5.25	5.30	5.70

Table 1.1: Comparison between the interatomic distances: third column geometrically calculated, fourth column experimentally evaluated [21] and last column simulated via MD method [27]. The interatomic distances r_{max} equal to the expectation values of the Gaussian distributions of the PDF.

1.3 The structure of alkali borate glass

Glasses doped with alkali atoms such as lithium, sodium, potassium, rubidum or caesium, are of strong scientific and economic interest due to their high technological potential for electrochemical devices such as solid-oxide fuel cells, solid-state batteries or chemical sensors [2].
The addition of so-called network modifiers, such as alkali oxides (A_2O) are responsible for the ionic conductivity of alkali borate glasses. The alkalis act like mobile ions and their mobility is dependent on their concentration, on the type of ion and on the surrounding B_2O_3 structure. To gain a better understanding of the ion's mobility, it is necessary to decipher the structural alteration due to the incorporation of A_2O.

Previous X-ray and neutron scattering experiments [14] [17] and MD simulations [28] on alkali borate glasses were only partly able to give an answer to the question of how the topology changes through doping.
1994 A.H. Verhoef and H.W. den Hartog [28] extended their MD simulation model from pure B_2O_3 glas to alkali borate glas. They doped their samples with certain concentrations of lithium and caesium atoms and observed a modification of the structure. They ascertained that the amount of tetrahedrally coordinated BO_4 molecules increase when increasing the alkali concentration. They deduced this phenomena from the altered boron-oxygen PDF, whose first peak slightly shifts to higher BO(1)-distances and exhibits a larger peak width, which coincide with the interatomic distance BO(1)=1.48 Å of the emerging tetrahedrons. Furthermore the coordination number B(O), which means the number of oxygen atoms surrounding a boron atom, increases from 3 to 4. There seems to be a relation between the amount of alkali concentration c_A and the number of tetrahedrons N_4 in the vitreous material:

$$N_4 = \frac{x}{1-x}. \tag{1.1}$$

The simulated data fits quite well to the equation 1.1 until the concentration c_A reaches approximately 30%. From that point on N_4 tends to decrease again. Through counting the tetrahedrons and the NBOs in the simulation box, they recognized that a reduction of BO_4 leads to an enhancement of NBOs. Obviously it is energetically more favourable for the alkali atoms to reside in the vicinity of negatively charged NBOs, which are mostly connected to BO_3 molecules, than in the vicinity of briging oxygens, which are connected to the BO_4 molecules. As a consequence, the A_2O structure tends to dock at triangles instead of sharing their oxygen atom with a tetrahedron.

Measuring the conductivity of the vitreous material leads to a similar behaviour. The conductivity increases with increasing alkali content until c_A reaches values of 30% [2]. Hence, the ionic conductivity is not just dependent on the concentration, but also on the number of existing NBOs, which seem to impair the mobility of the ions due to their strong local potential energy minima.
For the caesium-containing glasses the amount of BO_4 molecules is lower than for

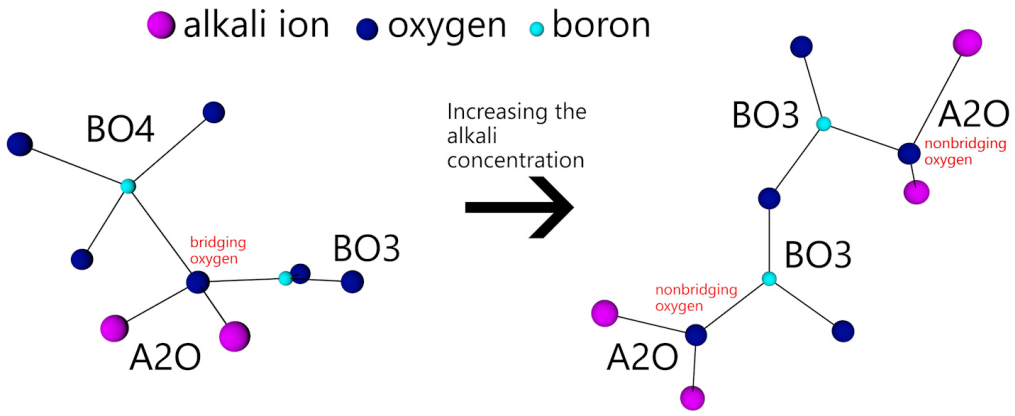

Figure 1.4: The supply of A_2O leads to the formation of BO_4 tetrahedrons until the alkali concentration reaches approximately 30%. Then the A_2O molecules tend to share their oxygen atom with BO_3 triangles due to potential energy efficiency.

lighter alkali borate glasses for all alkali concentrations. Evidently, glass doped with heavier ions contains more NBOs, which leads to smaller conductivity values. This is based on the assumption that the smaller sized lithium ions tend to reside next to BO_4 tetrahedrons, whereas for large caesium atoms this tendency decreases.
A.H. Verhoef and H.W. den Hartog pointed out that in their simulations of alkali borate glasses sixfold ring structures like B_3O_6 again were not found. In their opinion this configuration would be energetically unfavourable for all alkali concentrations. Raman spectroscopy measurements, however, were able to deliver the counterproof showing a strong intensity peak at 806 cm^{-1} in the Raman spectra, which is attributed to a totally symmetric vibration and belongs to the *breathing mode* of a boroxol ring [14]. This peak disappears when the concentration of the alkali content exceeds 30%.
Furthermore, scientists like H. Kentmotsu and Y. Iwadate, who scrutinized xRb_2O (1-x)B_2O_3 and xCs_2O (1-x)B_2O_3 suppose more complicated structures in vitreous alkali borate glasses like six-membered borate rings with BO_4 unit [17] or distorted octahedral units of CsO_6-type configuration [14].
Table 1.2 shows a comparison between the interatomic distances and the coordination number $\bar{n}$ of pure B_2O_3 and doped alkali borate glasses like 0.10Cs_2O 0.90B_2O_3 and 0.05Rb_2O 0.95B_2O_3 from X-ray and neutron scattering data [14], respectively [17].

atomic pair distances	r_{max} [Å] (a)	$\bar{n}$ (a)	r_{max} [Å] (b)	$\bar{n}$ (b)	r_{max} [Å] (c)	$\bar{n}$ (c)
BO(1) 3-folded	1.37	3	1.37	3	1.38	3
BO(1) 4-folded	-	-	1.48	4	1.48	4
OO(1)	2.37	4	2.37	4	2.46	4
BB(1)	2.43	3	2.43	3	2.56	3
BO(2)	2.74	1	2.74	1	3.00	1
BO(3)	3.20	2	3.10	2	-	-
AO(1)	-	-	3.23	4	3.08	6
BO(4)	3.63	2	3.63	2	3.75	4
AO(2)	-	-	3.66	2	-	-
OO(2)	4.10	1.33	4.10	1.33	4.33	1.33
OO(3)	4.20	2.66	4.37	2.66	4.71	1.33
OO(4)	4.75	1.33	4.75	1.33	5.19	2.66
AA(1)	-	-	4.91	1	-	-

Table 1.2: Comparison between the interatomic distances r_{max}, which are evaluated from the PDF and the coordination number $\bar{n}$ from pure B_2O_3 [14] (a), $0.10Cs_2O$ $0.90B_2O_3$ [14] (b) and $0.05Rb_2O$ $0.95B_2O_3$ [17] (c). AO and AA means the alkali-oxygen and the alkali-alkali distance, respectively.

Chapter 2

Diffraction Theory

2.1 Motivation

Examining polyatomic systems experimentally and gathering information about single types of atoms is quite tricky and often requires more than just experimental results.
Scientists working on polyatomic alkali borate glasses often compare their results obtained by experiments with simulation models and theoretical considerations to touch on the chance of differentiating between the atom types.
In a monoatomic system all the atoms are chemically identical and we assume no correlation between scattering length and atomic position. Gaining the structure factor, the PDF and the coordination number is quite simple. Whereas in polyatomic systems there is more than one kind of atom, which causes different scattering length distributions and different interatomic interactions [10].
Experimentally, a total structure factor is observed, which represents a distribution over all different kinds of atoms in the reciprocal space. The total structure factor is a weighted sum of several partial structure factors that are not accessible from experimental data only. For a complete decoding of the interatomic topology one needs to have information about the partial structure factors in a polyatomic system. Therefore, simulation methods are useful to compute the partial structure factors and compare their weighted sum with the experimentally gained total structure factor. Fitting procedures of the structure factor curve are also possible, but requires some constraints for the fitting parameters, which means that one should already have an idea about the interatomic structure.

The theoretical sections will present an overview of the diffraction theory concerning the scattering length, structure factor, PDF, radial distribution function and the coordination number in monatomic systems and eventually allows for the smooth transition to polyatomic systems. Comparing both systems, revealing difficulties of the polyatomic system and offering solutions for alkali borate glasses will be the main goal.

2.2 Experimental setup

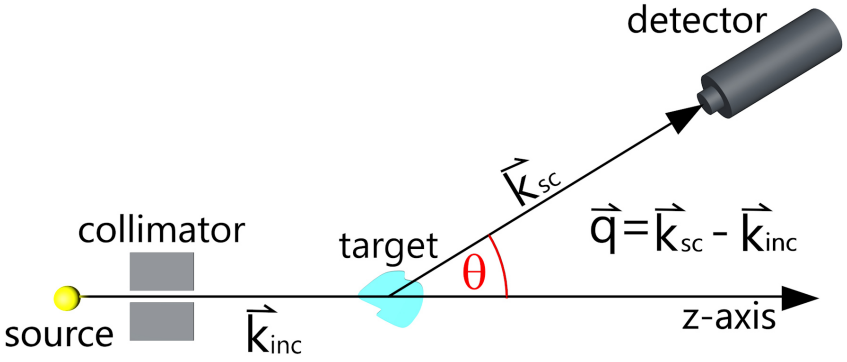

Figure 2.1: Setup of a typical diffraction experiment consisting of a particle source, a scattering target and a particle detector. The beam passes through a collimator with a slit of Δr.

A simple experimental setup for a diffraction experiment is shown in 2.1 and consists of a particle source, a scattering target (the sample) and a particle detector. The beam passes through a collimator with a beam opening of Δr. The beam of particles, respectively the electromagnetic wave propagates along the z-direction with a wave vector of $\mathbf{k} = \frac{2\pi}{\lambda}\hat{k}_z$ of wavelength λ (a bold letter describes a vector: $\boldsymbol{k} = \vec{k}$). The detector is simply counting the numbers of impinging particles which are diffracted into different angles (θ, ϕ) with respect to the axis of the propagating incident beam. We assume that the beam is perfectly monochromatic and perfectly collimated (which is of course according to the uncertainty principle impossible: $\Delta r > 0, \Delta k > 0$) and we also assume total elastic scattering, which leads to $k_{\text{inc}} = k_{\text{scat}}$ (a regular letter describes the absolute value of a vector: $k = |\vec{k}|$) and to the fact that all possible scattering vectors $\boldsymbol{q} = \boldsymbol{k}_{\mathbf{scat}} - \boldsymbol{k}_{\mathbf{inc}}$ are located on a sphere, called the *Ewald-sphere*. Structural investigations are always carried out by elastic scattering [5]. The magnitude q of the scattering vector can be calculated from the wavelength λ and the scattering angle θ as follows

$$q = \sqrt{k_{\text{inc}}^2 + k_{\text{scat}}^2 - 2k_{\text{inc}}\, k_{\text{scat}} \cos\theta} = \sqrt{2k_{\text{inc}}^2\,(1-\cos\theta)}$$

$$= \frac{4\pi}{\lambda}\sin\left(\frac{\theta}{2}\right). \tag{2.1}$$

Due to a collimator and the sufficient large distance L between the scatterer and the point source, the incident wave function at the point P can be described as a plane wave (see figure 2.2).

$$\text{At point P} : \psi_{\text{inc}}(t) = \psi_0 e^{i\boldsymbol{k}_{\text{inc}}\cdot(\boldsymbol{L}+\boldsymbol{r})-i\omega_0 t}. \tag{2.2}$$

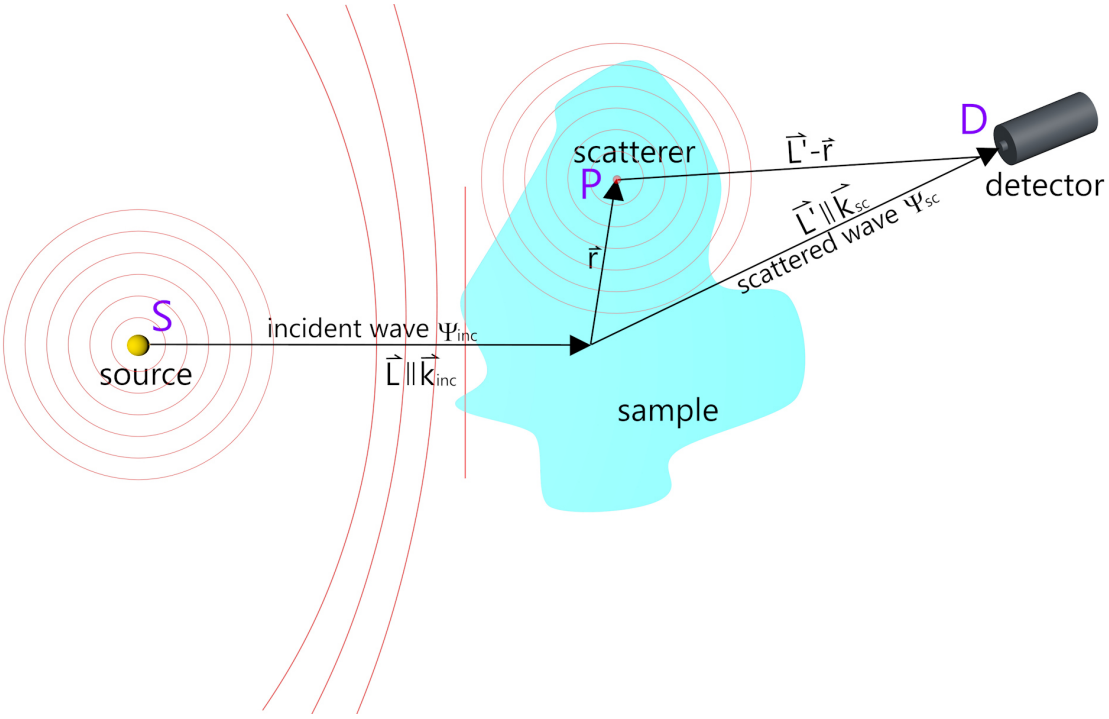

Figure 2.2: A schematic representation of a scattering event in a far-field approximation (Frauenhofer scattering). The source S and the detector D are sufficiently far away from the sample. The sample behaves like a scattering volume, in which the potential $V(r) \neq 0$.

The plane wave interacts with a scatterer, for instance an atom with its electron shell and an outgoing spherical wave is generated, originating from an atom of the sample at point P. The scattered spherical wave from point P propagates isoptropically and eventually reaches the detector at point D[1]:

$$\text{At point D} : \psi_{\text{scat}}(t) = \psi_{\text{inc}}(t) V(\boldsymbol{r}) \frac{e^{i\boldsymbol{k}_{\text{scat}} \cdot (\boldsymbol{L}' - \boldsymbol{r})}}{|\boldsymbol{L}' - \boldsymbol{r}|}. \tag{2.3}$$

$V(\boldsymbol{r})$ is the scattering potential of the atom at position $\boldsymbol{r}$ due to its electron density as discussed later. The distance r inside the sample is very small compared to L', hence $\psi_{\text{scat}}(t)$ simplifies to

$$\psi_{\text{scat}}(t) \cong \psi_{\text{inc}}(t) V(\boldsymbol{r}) \frac{e^{i\boldsymbol{k}_{\text{scat}} \cdot (\boldsymbol{L}' - \boldsymbol{r})}}{L'}. \tag{2.4}$$

Due to the small distance $r << L'$ we can also neglect the fact that actually $\boldsymbol{k}_{\text{inc}}$ and $\boldsymbol{k}_{\text{scat}}$ are varying with every point P in the scattering volume and assume that for all positions P the wave vectors $\boldsymbol{k}_{\text{inc}}$ and $\boldsymbol{k}_{\text{scat}}$ stay the same. Furthermore it is approximately valid that $\boldsymbol{k}_{\text{inc}} \parallel \boldsymbol{L}$ and $\boldsymbol{k}_{\text{scat}} \parallel \boldsymbol{L}'$.

$$\psi_{\text{scat}}(t) \cong \frac{\psi_0}{L'} e^{i(k_{\text{inc}} L + k_{\text{scat}} L')} e^{-i\omega_0 t} V(\boldsymbol{r}) e^{i(\boldsymbol{k}_{\text{inc}} - \boldsymbol{k}_{\text{scat}}) \cdot \boldsymbol{r}}. \tag{2.5}$$

[1] Probabilities that occur chronologically will be multiplied:
$|\psi_{\text{plane}}(S-P)|^2 |\psi_{\text{spherical}}(P-D)|^2 = |\psi_{\text{plane}}(S-P)\psi_{\text{spherical}}(P-D)|^2 = |\psi_{\text{scat}}(D)|^2$.

The total scattered wave at the detector's position D is a sum over all scattered points P with different vectors $\boldsymbol{r'}$ within the sample. Eventually we have to integrate over the whole scattered volume:

$$\psi_{\text{scat}}(t) \cong \frac{\psi_0}{L'} e^{i(k_{\text{inc}}L + k_{\text{scat}}L')} e^{-i\omega_0 t} \int_V V(\boldsymbol{r'}) e^{i(\boldsymbol{k}_{\text{inc}} - \boldsymbol{k}_{\text{scat}})\cdot \boldsymbol{r'}} \mathrm{d}^3 r' \ . \tag{2.6}$$

As we recognize the most important information about wave interference and hence structural features of the sample is packed in the integral of equation 2.6. For the total intensity at the detector's position D we obtain[2]:

$$\begin{aligned} \text{At point D} : I_{\text{total}} &= |\psi_{\text{inc}}(t)|^2 + |\psi_{\text{scat}}(t)|^2 \\ &\cong | \ \psi_0 e^{i\boldsymbol{k}_{\text{inc}}\cdot(\boldsymbol{L}+\boldsymbol{L'}) - i\omega_0 t} \ |^2 \\ + | \ \frac{\psi_0}{L'} e^{i(k_{\text{inc}}L + k_{\text{scat}}L')} e^{-i\omega_0 t} &\int_V V(\boldsymbol{r'}) e^{i(\boldsymbol{k}_{\text{inc}} - \boldsymbol{k}_{\text{scat}})\cdot \boldsymbol{r'}} \mathrm{d}^3 r' \ |^2 \ . \end{aligned}$$

Remember that the scattered wave vector $\boldsymbol{q}$ is defined as $\boldsymbol{q} = \boldsymbol{k}_{\text{scat}} - \boldsymbol{k}_{\text{inc}}$ and remember that $|\psi|^2 = \psi^* \psi$ with $|\mathrm{e}^{ia}|^2 = \mathrm{e}^{-ia}\mathrm{e}^{ia} = 1$:

$$\begin{aligned} &= \psi_0^2 + \frac{\psi_0^2}{L'^2} \left| \int_V V(\boldsymbol{r'}) e^{-i\boldsymbol{q}\cdot\boldsymbol{r'}} \mathrm{d}^3 r' \right|^2 \\ &= \psi_0^2 + \frac{\psi_0^2}{L'^2} |V(\boldsymbol{q})|^2. \end{aligned} \tag{2.7}$$

$$\text{with } V(\boldsymbol{q}) = \int_V V(\boldsymbol{r'}) e^{-i\boldsymbol{q}\cdot\boldsymbol{r'}} \mathrm{d}^3 r'. \tag{2.8}$$

As expected, the scattered intensity falls off with the distance $\frac{1}{L'^2}$. $V(\boldsymbol{q})$ describes the Fourier-transformation of the potential $V(\boldsymbol{r})$. We would obtain the same result by solving the Schrödinger equation via using the first Born approximation (which implies that no multiple scattering events between the points P and D occur) [11]. By solving the Schrödinger equation for X-ray scattering we gain a prefactor of $-\frac{m_{\text{xray}}}{2\pi\hbar^2}$, so I_{scat} turns to:

$$I_{\text{scat}} = -\frac{m_{\text{xray}}}{2\pi\hbar^2} \frac{1}{L'^2} \left| V(\boldsymbol{q}) \right|^2 = \frac{1}{L'^2} \left| f(\boldsymbol{q}) \right|^2. \tag{2.9}$$

The factor $f(\boldsymbol{q})$ is the so-called *scattering length*, which is also known from the differential cross section:

$$I_{\text{scat}} \propto \left(\frac{d\sigma}{d\Omega} \right) = |f(\boldsymbol{q})|^2. \tag{2.10}$$

Inserting the potential $V(\boldsymbol{r'})$ of the entire sample is generally not reliable. This would strongly lead to multiple scattering events that are excluded when making the assumptions for deducing the scattering length in this section. Multiple scattering is considered by higher order Born approximations [11], which is not inevitable

[2] Probabilities that occur simultaneously will be added (superposed):
$|\psi_{\text{inc}}(D)|^2 + |\psi_{\text{scat}}(D)|^2 = |\psi_{\text{total}}(D)|^2$.

in our experimental case.

Worth mentioning is the time-independence in the previous calculations (with the expectation of the single frequency ω_0 at the wave function ψ_{inc}). We assume a rigid lattice with the potential $V(\boldsymbol{r'})$, so the atoms will not get excited by the incident beam, which is equivalent to elastic scattering. Otherwise we would have to deal with a frequency-dependent potential $V(\boldsymbol{r'}, \omega)$ and a frequency-dependent scattered wave function $\psi_{\text{scat}}(\omega)$, where $\omega \neq \omega_0$. We also neglect thermal vibrations of the atoms, visualized by the time-dependency of the vector $\boldsymbol{r'}(t)$:

$$\psi_{\text{scat}}(\boldsymbol{q}, t) \propto \int_V V(\boldsymbol{r'}) e^{-i\boldsymbol{q}\cdot\boldsymbol{r'}(\boldsymbol{t})} \mathrm{d}^3 r'. \tag{2.11}$$

$$\boldsymbol{r'}(t) = \boldsymbol{u}(t) + \langle \boldsymbol{R} \rangle. \tag{2.12}$$

Here $\boldsymbol{u}(t)$ denotes the deviation of the atoms from its sites due to thermal vibrations and $\langle \boldsymbol{R} \rangle$ is the time-averaged position of the atom. Taking thermal vibrations into account leads to the so-called Debye-Waller factor that simply reduces the intensity of Bragg peaks by an exponential function [13]:

$$I = I_0 e^{-\frac{1}{3} q^2 \langle u(t)^2 \rangle}. \tag{2.13}$$

This missing intensity appears in between the Bragg peaks and becomes a part of the diffuse scattering. The diffuse intensity is widely spread over the q-space, and for high q-regions, where Bragg peaks are small due to the Debye-Waller factor, the scattering is predominately diffuse.

2.3 The static structure factor

In general there is a differentiation between a static structure factor and a dynamic structure factor. In our case of time-independent X-ray diffraction measurements we were only interested in the static structure factor $S(\boldsymbol{q})$ that is independent of the frequency ω. For time-dependent X-ray diffraction measurements the dynamic structure factor $S(\boldsymbol{q}, \omega)$ is used.

We obtained ψ_{scat} by superposing all scattered waves, originating from different points P, and expressed it by an integral over the volume of the sample (see equation 2.6). Using a sum over discrete points i instead of the integral and replacing the unknown potential $V(\boldsymbol{r})$ (from now on changing the designation from r' to r) of the entire sample by the so-called atomic form factor $f_{\text{at}}(q)$ corresponding to single scatterers, guides us to:

$$\psi_{\text{scat}}(\boldsymbol{q}) \propto \sum_{i}^{n} f_{\text{at},i}(\boldsymbol{q}) e^{-i\boldsymbol{q}\cdot\boldsymbol{r_i}}. \tag{2.14}$$

For the scattered intensity this means (assuming real numbered form factors $f_{\text{at}}(\boldsymbol{q})^* = f_{\text{at}}(\boldsymbol{q})$):

$$I_{\text{scat}}(\boldsymbol{q}) = \psi_{\text{scat}}(\boldsymbol{q})^* \psi_{\text{scat}}(\boldsymbol{q}) \propto \sum_{i,j}^{n} f_{\text{at},i}(\boldsymbol{q}) f_{\text{at},j}(\boldsymbol{q}) e^{-i\boldsymbol{q}\cdot(\boldsymbol{r_j}-\boldsymbol{r_i})}, \tag{2.15}$$

where $i, j = 1, 2, 3, ..n$ and n is the amount of atoms in the sample. The static structure factor is defined by this intensity normalized[3] by $\frac{1}{\sum_i^n f_{\text{at},i}(\boldsymbol{q})^2}$:

$$S(\boldsymbol{q}) = \frac{I_{\text{scat}}(\boldsymbol{q})}{\sum_i^n f_{\text{at},i}(\boldsymbol{q})^2}$$

$$= \frac{1}{\sum_i^n f_{\text{at},i}(\boldsymbol{q})^2} \sum_{i,j}^{n} f_{\text{at},i}(\boldsymbol{q}) f_{\text{at,j}}(\boldsymbol{q}) e^{-i\boldsymbol{q}\cdot(\boldsymbol{r_j}-\boldsymbol{r_i})}, \tag{2.16}$$

where the atomic form factor $f_{\text{at}}(\boldsymbol{q})$ representing the amplitude of the wavelet, is the Fourier-transformation of the atomic potential $V_{\text{at}}(\boldsymbol{r})$:

$$f_{\text{at}}(\boldsymbol{q}) = \mathcal{F}\{V_{\text{at}}(\boldsymbol{r})\} = \int_{atom} V_{\text{at}}(\boldsymbol{r}) e^{-i\boldsymbol{q}\cdot\boldsymbol{r}} \, \mathrm{d}^3 r. \tag{2.17}$$

[3] Because of the determination of $S(\boldsymbol{q} \to \infty) = 1$ a proper normalization $\mathcal{N}$ is necessary:

$$I_{\text{scat}}(\boldsymbol{q} \to \infty) = \sum_{i=j}^{n} f_{\text{at},i}(\boldsymbol{q}) f_{\text{at},j}(\boldsymbol{q}) + \sum_{i \neq j}^{n} f_{\text{at},i}(\boldsymbol{q}) f_{\text{at},j}(\boldsymbol{q}) e^{-\infty} = \sum_{i}^{n} f_{\text{at},i}(\boldsymbol{q})^2$$

$$S(\boldsymbol{q} \to \infty) = \frac{I_{\text{scat}}(\boldsymbol{q} \to \infty)}{\mathcal{N}} \stackrel{!}{=} 1,$$

when

$$\mathcal{N} = \sum_{i}^{n} f_{\text{at,i}}(\boldsymbol{q})^2.$$

In a mathematically more precise language the same result is achieved by separating $V(\boldsymbol{r})$ from 2.8 into a potential $h(\boldsymbol{r})$ of atomic positions within the sample, where $V(\boldsymbol{r}) \neq 0$ (everywhere else in the sample we assume $V(\boldsymbol{r}) = 0$) and a corresponding atomic potential $V_{\mathrm{at}}(\boldsymbol{r})$. This means a convolution of $h(\boldsymbol{r})$ and $V_{\mathrm{at}}(\boldsymbol{r})$ in real space and a multiplication of $\mathcal{F}\{h(\boldsymbol{r})\}$ and $\mathcal{F}\{V_{\mathrm{at}}(\boldsymbol{r})\}$ in reciprocal space:

$$\text{Real space}: \; V(\boldsymbol{r}) = V_{\mathrm{at}}(\boldsymbol{r}) * h(\boldsymbol{r}) \tag{2.18}$$

$$\text{Reciprocal space}: \; \psi_{\mathrm{scat}} \propto \mathcal{F}\{V(\boldsymbol{r})\} = \mathcal{F}\{V_{\mathrm{at}}(\boldsymbol{r})\}\mathcal{F}\{h(\boldsymbol{r})\}. \tag{2.19}$$

The potential $h(\boldsymbol{r})$ of the atomic positions r_i is expressed by a delta distribution:

$$h(\boldsymbol{r}) = \sum_{i}^{n} \delta^{(3)}(\boldsymbol{r} - \boldsymbol{r_i}). \tag{2.20}$$

Thus, the static structure factor $S(\boldsymbol{q})$ turns into:

$$\begin{aligned} S(\boldsymbol{q}) &= \frac{1}{\sum_i^n f_{\mathrm{at,i}}(\boldsymbol{q})^2} |\mathcal{F}\{V_{\mathrm{at}}(\boldsymbol{r})\}\mathcal{F}\{h(\boldsymbol{r})\}|^2 \\ &= \frac{1}{\sum_i^n f_{\mathrm{at,i}}(\boldsymbol{q})^2} \left| \left(\int_{atom} V_{\mathrm{at}}(\boldsymbol{r}) e^{-i\boldsymbol{q}\cdot\boldsymbol{r}} \, \mathrm{d}^3 r \right) \left(\int_V \sum_i^n \delta^{(3)}(\boldsymbol{r} - \boldsymbol{r_i}) e^{-i\boldsymbol{q}\cdot\boldsymbol{r}} \, \mathrm{d}^3 r \right) \right|^2 \\ &= \frac{1}{\sum_i^n f_{\mathrm{at,i}}(\boldsymbol{q})^2} \sum_{i,j}^{n} f_{\mathrm{at,i}}(\boldsymbol{q}) f_{\mathrm{at,j}}(\boldsymbol{q}) e^{-i\boldsymbol{q}\cdot(\boldsymbol{r_j} - \boldsymbol{r_i})}. \end{aligned} \tag{2.21}$$

For the case of crystals it is useful to split up $h(\boldsymbol{r})$ once more into a potential $g(\boldsymbol{r})$ of periodically arranged lattice points and a potential $b(\boldsymbol{r})$ of basis points within one lattice element. Then, the atomic potential $V_{\mathrm{at}}(\boldsymbol{r})$ belongs to a particular basis.

$$\text{Real space}: \; V(\boldsymbol{r}) = V_{\mathrm{at}}(\boldsymbol{r}) * h(\boldsymbol{r}) = V_{\mathrm{at}}(\boldsymbol{r}) * g(\boldsymbol{r}) * b(\boldsymbol{r}) \tag{2.22}$$

$$g(\boldsymbol{r}) = \sum_{R}^{N} \delta^{(3)}(\boldsymbol{r} - \boldsymbol{R}) \tag{2.23}$$

$$b(\boldsymbol{r}) = \sum_{i}^{n} \delta^{(3)}(\boldsymbol{r} - \boldsymbol{d_i}) \tag{2.24}$$

The periodic lattice vector is described by $\boldsymbol{R} = n_1\boldsymbol{a_1} + n_2\boldsymbol{a_2} + n_3\boldsymbol{a_3}$ (with $n_1, n_2, n_3 = 1, 2, 3, ..$). The basis vectors that span the Bravais lattice are described by $\boldsymbol{d_i}$. Eventually for the wave function ψ_{scat} of a crystal we obtain:

$$\psi_{\mathrm{scat}} \propto \mathcal{F}\{V(\boldsymbol{r})\} \overset{\boldsymbol{q}=\boldsymbol{G}}{=} F(\boldsymbol{G}) S_{hkl}(\boldsymbol{G}), \tag{2.25}$$

where the shape factor $F(\boldsymbol{G})$ and the structure factor $S_{hkl}(\boldsymbol{G})$ of crystals are defined as:

$$F(\boldsymbol{G}) = \mathcal{F}\{g(\boldsymbol{r})\} = \sum_{R}^{N} e^{-i\boldsymbol{G}\cdot\boldsymbol{R}} = N \tag{2.26}$$

$$S_{hkl}(\boldsymbol{G}) = \mathcal{F}\{b(\boldsymbol{r})\}\mathcal{F}\{V_{\text{at}}(\boldsymbol{r})\} = \sum_{i}^{n} f_{\text{at}}(\boldsymbol{G})_i e^{-i\boldsymbol{G}\cdot\boldsymbol{d_i}}. \tag{2.27}$$

$\boldsymbol{G}$ is defined as reciprocal lattice vector: $\boldsymbol{G} = h\boldsymbol{b_1} + k\boldsymbol{b_2} + l\boldsymbol{b_3}$ (with the Miller indices $h, k, l = 1, 2, 3, ...$).
So if the scattering vector $\boldsymbol{q} = \boldsymbol{G}$, the shape factor $F(\boldsymbol{G})$ of a perfect crystal (that means no deviation of the lattice vector $\boldsymbol{R}$, hence $\boldsymbol{G} \cdot \boldsymbol{R} = 2\pi n$; with $n = 1, 2, 3, ...$) is simply N, which is the total number of lattice elements within the sample. Due to the knowledge of all Bravais lattices with its corresponding basis vectors $\boldsymbol{d_i}$ (sc, fcc, bcc,...) only certain triples of h, k, l exists, that fulfil $S_{hkl}(\boldsymbol{G}) > 0$ and are related to the diffraction peaks (Bragg Peaks) in the reciprocal space.
Comparing the experimentally gained diffraction pattern of crystalline materials with the allowed triples of h, k, l yields the desired information of the structural arrangement.

Note that there are confusingly two different mathematical expressions in use for the structure factors $S(\boldsymbol{q})$ and $S_{hkl}(\boldsymbol{G})$. The static structure factor $S(\boldsymbol{q})$ is most useful for partially ordered or disordered systems, whereas $S_{hkl}(\boldsymbol{G})$ is only valid for systems with long-range positional order. $S_{hkl}(\boldsymbol{G})$ is a mathematical description of the interference pattern of one specific Bravais-lattice spanned by the basis vectors $\boldsymbol{d_i}$ and it is proportional to the wave function ψ_{scat}, whereas $S(\boldsymbol{q})$ is proportional to the scattered intensity $|\psi_{\text{scat}}|^2$. To avoid confusions the static structure factor is often called *total scattering structure function* [8].

The loss of long-range order becomes apparent in the $S(q)$-function. A perfect crystal exhibits definite delta distributions at values $q = G$, whereas only short- and middle range ordered materials show a sum of Gaussian shaped peaks at different values of q. Thus, the more disordered the material, the broader the peaks until they completely blur to some irregular noise around a constant $S(q) = 1$ constituting complete randomness (except for the first peak corresponding to the short-range order).

In our case we want to analyse the short- and middle-range structure of amorphous glasses. Hence, if we recognize sharp intensity peaks instead of some smooth buckles, our sample exhibits crystalline behaviour, which we actually want to prevent and, as explained in the next sections, is a problem of glass powder manufacturing.

2.3.1 Structure factor used by PDFgetX

The program PDFgetX that we used for evaluating our raw intensity data, is based on another definition of the static structure factor $S_{\text{PDFgetX}}(\boldsymbol{q})$. For this purpose we separate the intensity $I_{\text{scat}}(\boldsymbol{q})$ into a *coherent* term and an *incoherent* term [10]. Before we do so, we define the expectation value of the form factor square $\langle f_{\text{at}}^2 \rangle$ and the squared expectation value of the form factor $\langle f_{\text{at}} \rangle^2$ (for a faster notation the q-dependency of the form factor $f_{\text{at}}(\boldsymbol{q})$ is omitted):

$$\frac{1}{N}\sum_i f_{\mathrm{at},i}^2 = \frac{1}{N}\sum_\alpha N_\alpha f_{\mathrm{at},\alpha}^2 = \sum_\alpha c_\alpha f_{\mathrm{at},\alpha}^2 = \langle f_{\mathrm{at}}^2\rangle \tag{2.28}$$

The concentration c_α of the atomic species α is defined as:

$$c_\alpha = \frac{N_\alpha}{N}, \tag{2.29}$$

where N is the total number of atoms and N_α is the number of atoms of type α. The index i is counting every single atom in the sample, whereas the index α is summarizing all atoms of the same sort.

$$\langle f_{\mathrm{at}}\rangle^2 = \frac{1}{N^2}\sum_{i,j} f_{\mathrm{at},i} f_{\mathrm{at},j}$$

$$\frac{1}{N^2}\sum_{\alpha\beta} N_\alpha N_\beta f_{\mathrm{at},\alpha} f_{\mathrm{at},\beta} = \sum_{\alpha\beta} c_\alpha c_\beta f_{\mathrm{at},\alpha} f_{\mathrm{at},\beta}. \tag{2.30}$$

In the case of monatomic systems $\langle f_{\mathrm{at}}^2\rangle$ and $\langle f_{\mathrm{at}}\rangle^2$ simplifies to (for precise calculation see 2.47 and 2.48):

$$\langle f_{\mathrm{at}}^2\rangle = \langle f_{\mathrm{at}}\rangle^2 = f_{\mathrm{at}}^2. \tag{2.31}$$

Before we derive the correlation between the scattered intensity and the structure factor in the PDFgetX formalism, we define the structure factor $S_{\mathrm{PDFgetX}}(\boldsymbol{q})$. We differentiate between a polyatomic and a monatomic version of the structure factor. For the polyatomic version we have to define a partial structure factor $S_{\mathrm{PDFgetX},\alpha\beta}$ (the prefactor $\frac{N}{N_\alpha N_\beta}$ is explained in section 2.5.2):

$$S_{\mathrm{PDFgetX},\alpha\beta}(\boldsymbol{q}) := \frac{N}{N_\alpha N_\beta}\sum_{i_\alpha, j_\beta} e^{-i\boldsymbol{q}\cdot(\boldsymbol{r_{j_\beta}} - \boldsymbol{r_{i_\alpha}})}. \tag{2.32}$$

For the monatomic case the structure factor $S_{\mathrm{PDFgetX}}(\boldsymbol{q})$ is defined as:

$$S_{\mathrm{PDFgetX}}(\boldsymbol{q}) := \frac{1}{N}\sum_{i,j} e^{-i\boldsymbol{q}\cdot(\boldsymbol{r_j} - \boldsymbol{r_i})}. \tag{2.33}$$

Noticeable is that the atomic form factor is not included in the definition of the polyatomic structure factor $S_{\mathrm{PDFgetX},\alpha\beta}(\boldsymbol{q})$ or the monatomic structure factor $S_{\mathrm{PDFgetX}}(\boldsymbol{q})$ used by the PDFgetX formalism. In the monatomic case the atomic form factor is anyway the same for every atom, hence it is allowed to put it out of the sum. In the polyatomic case it is possible due to the sum over specific atomic types α and β at the positions i_α and j_β, hence the corresponding atomic form factors $f_{\mathrm{at},\alpha}$ and $f_{\mathrm{at},\beta}$ are also allowed to be extracted from the sum.
Furthermore $S_{\mathrm{PDFgetX},\alpha\beta}(\boldsymbol{q}) - 1$ is:

$$S_{\mathrm{PDFgetX},\alpha\beta}(\boldsymbol{q}) - 1 = \frac{N}{N_\alpha N_\beta}\sum_{i_\alpha \neq j_\beta} e^{-i\boldsymbol{q}\cdot(\boldsymbol{r_{j_\beta}} - \boldsymbol{r_{i_\alpha}})}. \tag{2.34}$$

As can be seen by equation 2.32 the partial structure factor is symmetric in its indices:

$$S_{\alpha\beta}(\boldsymbol{q}) = S_{\beta\alpha}(\boldsymbol{q}). \tag{2.35}$$

We now separate the intensity $I_{\text{scat}}(\boldsymbol{q})$ into a "self-scattering" term with $i = j$ and a "distinct-scattering" term where $i \neq j$ (we are investigating the polyatomic case, which can be easily and any time reduced to a monatomic system):

$$\begin{aligned} I_{\text{scat}}(\boldsymbol{q}) &= \sum_{i,j} f_{\text{at},i} f_{\text{at},j} e^{-i\boldsymbol{q}\cdot(\boldsymbol{r_j}-\boldsymbol{r_i})} = \sum_{i=j} f_{\text{at},i}^2 + \sum_{i\neq j} f_{\text{at},i} f_{\text{at},j} e^{-i\boldsymbol{q}\cdot(\boldsymbol{r_j}-\boldsymbol{r_i})} \\ &= N\langle f_{\text{at}}^2\rangle + \sum_{\alpha,\beta} f_{\text{at},\alpha} f_{\text{at},\beta} \sum_{i_\alpha \neq j_\beta} e^{-i\boldsymbol{q}\cdot(\boldsymbol{r_{j\beta}}-\boldsymbol{r_{i\alpha}})}. \end{aligned}$$

We expand the second part and use 2.34:

$$\begin{aligned} \sum_{\alpha,\beta} f_{\text{at},\alpha} f_{\text{at},\beta} \sum_{i_\alpha \neq j_\beta} e^{-i\boldsymbol{q}\cdot(\boldsymbol{r_{j\beta}}-\boldsymbol{r_{i\alpha}})} &= N \sum_{\alpha,\beta} f_{\text{at},\alpha} f_{\text{at},\beta} \frac{N_\alpha N_\beta}{N^2} \frac{N}{N_\alpha N_\beta} \sum_{i_\alpha \neq j_\beta} e^{-i\boldsymbol{q}\cdot(\boldsymbol{r_{j\beta}}-\boldsymbol{r_{i\alpha}})} \\ &= N \sum_{\alpha,\beta} f_{\text{at},\alpha} f_{\text{at},\beta} c_\alpha c_\beta \left(S_{\text{PDFgetX},\alpha\beta}(\boldsymbol{q}) - 1\right) \\ &= N \sum_{\alpha,\beta} f_{\text{at},\alpha} f_{\text{at},\beta} c_\alpha c_\beta S_{\text{PDFgetX},\alpha\beta}(\boldsymbol{q}) - N\langle f_{\text{at}}\rangle^2. \end{aligned}$$

We now introduce the *Faber-Ziman* structure factor $S_{\text{FZ}}(\boldsymbol{q})$:

$$S_{\text{FZ}}(\boldsymbol{q}) = \sum_{\alpha,\beta} \frac{f_{\text{at},\alpha} f_{\text{at},\beta} c_\alpha c_\beta}{\langle f_{\text{at}}\rangle^2} S_{\text{PDFgetX},\alpha\beta}(\boldsymbol{q}). \tag{2.36}$$

Applying the *Faber-Ziman* structure factor $S_{\text{FZ}}(\boldsymbol{q})$ in the derivation yields:

$$I_{\text{scat}}(\boldsymbol{q}) = N\langle f_{\text{at}}^2\rangle + N\langle f_{\text{at}}\rangle^2 S_{\text{FZ}}(\boldsymbol{q}) - N\langle f_{\text{at}}\rangle^2.$$

Eventually the scattered intensity $I_{\text{scat}}(\boldsymbol{q})$ per atom equals to:

$$\frac{I_{\text{scat}}(\boldsymbol{q})}{N} = \langle f_{\text{at}}^2\rangle - \langle f_{\text{at}}\rangle^2 + \langle f_{\text{at}}\rangle^2 S_{\text{FZ}}(\boldsymbol{q}). \tag{2.37}$$

The *incoherent* term of the intensity is given by the variance of the atomic form factor: $var(f_{\text{at}}) = \langle f_{\text{at}} - \langle f_{\text{at}}\rangle\rangle^2 = \langle f_{\text{at}}^2\rangle - \langle f_{\text{at}}\rangle^2$ and is the so-called *Laue monotonic scattering* [1]. It is a small, very slowly varying function, representing a continuous diffuse scattering and appears only if the sample consists of more than one type of atom. It is not distinguishable from background scattering, hence it has never been quantitatively evaluated in an experiment.
The *coherent* part of equation 2.37 is the ordinary reflection term of the sample containing the structure factor $S_{\text{FZ}}(\boldsymbol{q})$:

$$I_{\text{scat}}(\boldsymbol{q})/N = I_{\text{scat}}^{\text{incoh}}(\boldsymbol{q}) + I_{\text{scat}}^{\text{coh}}(\boldsymbol{q}) \tag{2.38}$$

$$I_{\text{scat}}^{\text{incoh}}(\boldsymbol{q}) = var(f_{\text{at}}) \tag{2.39}$$

$$I_{\text{scat}}^{\text{coh}}(\boldsymbol{q}) = \langle f_{\text{at}} \rangle^2 S_{\text{FZ}}(\boldsymbol{q}). \tag{2.40}$$

Comparing the *Faber-Ziman* structure factor with the structure factor $S(\boldsymbol{q})$ from [2.16]:

$$S_{\text{FZ}}(\boldsymbol{q}) = \frac{I_{\text{scat}}^{\text{coh}}(\boldsymbol{q})}{\langle f_{\text{at}} \rangle^2} \tag{2.41}$$

$$S(\boldsymbol{q}) = \frac{I_{\text{scat}}(\boldsymbol{q})}{\langle f_{\text{at}}^2 \rangle}. \tag{2.42}$$

The complete structural information is hidden in the *coherent* part of the intensity. Hence it makes sense to define the structure factor by $I_{\text{scat}}^{\text{coh}}(\boldsymbol{q})$ instead of defining it by the total intensity $I_{\text{scat}}(\boldsymbol{q})$ as we did before 2.16.
The second difference regarding equation 2.16 is the normalization term. Before we had the normalization factor[4] $\frac{1}{\langle f_{\text{at}}^2 \rangle}$ that now changes to $\frac{1}{\langle f_{\text{at}} \rangle^2}$, because again we have to insure that $S_{\text{FZ}}(\boldsymbol{q})$ reaches unity[5] for $\boldsymbol{q} \to \infty$.

The structure factor $S_{\text{FZ}}(\boldsymbol{q})$ is linked to the scattered intensity $I_{\text{scat}}(\boldsymbol{q})$ via:

$$\frac{I_{\text{scat}}(\boldsymbol{q})}{N} = \langle f_{\text{at}}^2 \rangle - \langle f_{\text{at}} \rangle^2 + \langle f_{\text{at}} \rangle^2 S_{\text{FZ}}(\boldsymbol{q})$$

$$S_{\text{FZ}}(\boldsymbol{q}) = \frac{\frac{I_{\text{scat}}(\boldsymbol{q})}{N} - (\langle f_{\text{at}}^2 \rangle - \langle f_{\text{at}} \rangle^2)}{\langle f_{\text{at}} \rangle^2}$$

$$S_{\text{FZ}}(\boldsymbol{q}) = \frac{\frac{I_{\text{scat}}(\boldsymbol{q})}{N} - var(f_{\text{at}})}{\langle f_{\text{at}} \rangle^2}. \tag{2.43}$$

It is evident that the program PDFgetX subtracts the *Laue monotonic scattering* term $var(f_{\text{at}})$ from the experimentally gained scattered intensity $I_{\text{scat}}(\boldsymbol{q})$, so that $S_{\text{FZ}}(\boldsymbol{q})$ consists only of the structural information of the sample.

---

[4] The normalization of equation 2.16 was actually $1/(N\langle f_{\text{at}}^2 \rangle) = 1/(\sum_i f_{\text{at},i}^2)$. If we define the unnormalized structure factor by the scattered intensity per atom $S(\boldsymbol{q}) = I_{\text{scat}}(\boldsymbol{q})/N$ like we did it for the deviation of 2.38, then the normalization yields $1/\langle f_{\text{at}}^2 \rangle$.

[5] Calculation of the normalization factor $\mathcal{N}$ for $S_{\text{FZ}}(\boldsymbol{q})$:

$$I_{\text{scat}}^{\text{coh}}(\boldsymbol{q} \to \infty) = \langle f_{\text{at}} \rangle^2 S_{\text{FZ}}(\boldsymbol{q} \to \infty) = \sum_{\alpha,\beta} f_{\text{at},\alpha} f_{\text{at},\beta} c_\alpha c_\beta S_{\text{PDFgetX},\alpha\beta}(\boldsymbol{q} \to \infty)$$

$$= \sum_{\alpha,\beta} c_\alpha c_\beta f_{\text{at},\alpha} f_{\text{at},\beta} = \langle f_{\text{at}} \rangle^2,$$

where $S_{\text{PDFgetX},\alpha\beta}(\boldsymbol{q} \to \infty) = 1$.

$$S_{\text{FZ}}(\boldsymbol{q} \to \infty) = \frac{I_{\text{scat}}^{\text{coh}}(\boldsymbol{q} \to \infty)}{\mathcal{N}} \stackrel{!}{=} 1,$$

when

$$\mathcal{N} = \langle f_{\text{at}} \rangle^2.$$

2.3.2 Structure factor for isotropic materials by Debye

Originally Debye expressed another notation for the structure factor if the material exhibits isotropic behaviour. Powder of crystals, nanoparticles, liquids or in our case glass ("frozen liquid") belong to isotropic samples. As explained in the introduction every structural orientation in glass exists with equal probability, so we can take an orientational average [9]. The scattering vector $\boldsymbol{q}$ should be placed along the ad hoc selected z-direction, thus we get:

$$\boldsymbol{q} \cdot \boldsymbol{r} = qr\cos\theta. \tag{2.44}$$

We are able to rewrite the orientational averaged structure factor (for faster notation we change $r_j - r_i$ to r_{ji}):

$$\begin{aligned} e^{-i\boldsymbol{q}\cdot\boldsymbol{r_{ji}}} &= \frac{\int_0^{2\pi}\mathrm{d}\phi\int_0^{\pi}\mathrm{d}\theta e^{-iqr_{ji}\cos\theta}r_{ji}^2\sin\theta}{\int_0^{2\pi}\mathrm{d}\phi\int_0^{\pi}\mathrm{d}\theta\, r_{ji}^2\sin\theta} \\ u = \cos\theta \rightarrow \mathrm{d}\theta &= \frac{1}{\sin\theta}\mathrm{d}u \\ &= \frac{-2\pi r_{ji}^2\int_0^{\pi} e^{-iqr_{ji}u}\frac{\sin\theta}{\sin\theta}\mathrm{d}u}{4\pi r_{ji}^2} \\ &= \frac{\sin(qr_{ji})}{qr_{ji}}. \end{aligned}$$

For the monatomic system we finally obtain:

$$S_{\mathrm{Debye}}(q) = \frac{1}{N}\sum_{i,j}\frac{\sin(qr_{ji})}{qr_{ji}}. \tag{2.45}$$

For the polyatmic system we obtain an isotropic version of the partial structure factor $S_{\mathrm{Debye},\alpha\beta}(q)$:

$$S_{\mathrm{Debye},\alpha\beta}(q) = \frac{N}{N_\alpha N_\beta}\sum_{i_\alpha,j_\beta}\frac{\sin(qr_{j_\beta i_\alpha})}{qr_{j_\beta i_\alpha}}. \tag{2.46}$$

2.3.3 Structure factor for monatomic systems

In the case of monatomic systems $\langle f_{\mathrm{at}}^2\rangle$ and $\langle f_{\mathrm{at}}\rangle^2$ turns into:

$$\langle f_{\mathrm{at}}^2\rangle = \frac{1}{N}\sum_{i}^{N} f_{\mathrm{at},i}^2 = \frac{1}{N}N f_{\mathrm{at}}^2 = f_{\mathrm{at}}^2 \tag{2.47}$$

$$\langle f_{\mathrm{at}}\rangle^2 = \frac{1}{N}\left(\sum_i f_{\mathrm{at},i}\right)\frac{1}{N}\left(\sum_i f_{\mathrm{at},i}\right) = f_{\mathrm{at}}^2. \tag{2.48}$$

Thus, $S_{\mathrm{FZ}}(\boldsymbol{q})$ and $S(\boldsymbol{q})$ yield the same solution:

$$S_{\mathrm{FZ}}(\boldsymbol{q}) = \frac{\frac{I_{\mathrm{scat}}(\boldsymbol{q})}{N} - f_{\mathrm{at}}^2 + f_{\mathrm{at}}^2}{f_{\mathrm{at}}^2} = \frac{I_{\mathrm{scat}}(\boldsymbol{q})}{N f_{\mathrm{at}}^2} \tag{2.49}$$

$$S(\boldsymbol{q}) = \frac{I_{\text{scat}}(\boldsymbol{q})}{N f_{\text{at}}^2}. \tag{2.50}$$

Consequently there exits no *Laue monotonic scattering* for monatomic systems. The destructive interference pattern has zero intensity, whereas for polyatomic systems due to $var(f_{\text{at}})$, there is still a remaining intensity even though the interference term cancels out.

2.4 Atomic form factor

As we already described in section 2.3 the amplitude of the wavelets is the so-called atomic form factor that is given by the Fourier-transformed atomic potential $V_{\text{at}}(\boldsymbol{r})$:

$$f_{\text{at}}(\boldsymbol{q}) = \mathcal{F}\{V_{\text{at}}(\boldsymbol{r})\} = \int_{atom} V_{\text{at}}(\boldsymbol{r}) e^{-i\boldsymbol{q}\cdot\boldsymbol{r}} \, \mathrm{d}^3 r. \tag{2.51}$$

For electron scattering the potential would contain an attractive part due to the positive charged core (Coulomb force) and a repulsive part, which can be expressed by an integration over the electron density $\rho(\boldsymbol{r})$ of the atom.
In the X-ray scattering the nucleus does not participate in the scattering intensity since it is too massive to accelerate. Only the orbital electrons influence the scattered wavelets. Hence, it is sufficient to replace the atomic potential $V_{\text{at}}(\boldsymbol{r})$ with the electron density $\rho(\boldsymbol{r})$ and the Thompson scattering prefactor $\frac{e^2}{E}$ with the electron charge e and the energy $E = m_{\text{xray}} c^2$ of the incident beam [11] (see equation 2.9).

$$f_{\text{at}}(\boldsymbol{q}) = \frac{e^2}{m_{\text{xray}} c^2} \int_0^\infty \rho(\boldsymbol{r}) e^{-i\boldsymbol{q}\cdot\boldsymbol{r}} \, \mathrm{d}^3 r. \tag{2.52}$$

The phenomenological function describing the atomic form factor can be approximated by four superposed Gaussians plus a constant giving a total number of nine parameters [6]:

$$f_{\text{at}}(q) = \sum_{i=1}^{4} a_i e^{-b_i \left(\frac{q}{4\pi}\right)^2} + c. \tag{2.53}$$

For $f_{\text{at}}(\boldsymbol{q} = 0)$ the atomic form factor equals to the atomic number Z that is the number of electrons for ions or neutral atoms.

2.5 Pair distribution function (PDF)

2.5.1 The monatomic case

The pair distribution function (PDF) $g(\boldsymbol{r})$ is proportional to the probability of finding an atom at a position $\boldsymbol{r}$ relative to a reference atom taken to be at the origin [10]:

$$g(\boldsymbol{r}) = \frac{1}{\rho N} \sum_{i \neq j} \delta^{(3)}(\boldsymbol{r} - \boldsymbol{r_{ji}}). \tag{2.54}$$

The PDF $g(\boldsymbol{r})$ is also defined as Fourier-transformation of the structure factor $S_{\mathrm{PDFgetX}}(\boldsymbol{q})$:

$$g(\boldsymbol{r}) - 1 = \frac{1}{\rho}\mathcal{F}\{S_{\mathrm{PDFgetX}}(\boldsymbol{q}) - 1\}$$

$$g(\boldsymbol{r}) - 1 = \frac{1}{\rho(2\pi)^3}\int_V (S_{\mathrm{PDFgetX}}(\boldsymbol{q}) - 1)\, e^{i\boldsymbol{q}\cdot\boldsymbol{r}}\, \mathrm{d}q^3 \tag{2.55}$$

The inverse Fourier-transformation yields the structure factor $S_{\mathrm{PDFgetX}}(\boldsymbol{q})$:

$$S_{\mathrm{PDFgetX}}(\boldsymbol{q}) - 1 = \rho\mathcal{F}\{g(\boldsymbol{r}) - 1\}$$

$$S_{\mathrm{PDFgetX}}(\boldsymbol{q}) - 1 = \rho\int_V (g(\boldsymbol{r}) - 1)\, e^{-i\boldsymbol{q}\cdot\boldsymbol{r}}\, \mathrm{d}r^3. \tag{2.56}$$

Due to the density normalization ρ, $g(\boldsymbol{r})$ and $S_{\mathrm{PDFgetX}}(\boldsymbol{q})$ are dimensionless. The "-1" term in the integrand of equation 2.56 represents the forward scattering at $\boldsymbol{q} = 0$.

$$S_{\mathrm{PDFgetX}}(\boldsymbol{q}) - 1 = \rho\int_V g(\boldsymbol{r}) e^{-i\boldsymbol{q}\cdot\boldsymbol{r}}\, \mathrm{d}r^3 \; - \rho\int_V e^{-i\boldsymbol{q}\cdot\boldsymbol{r}}\, \mathrm{d}r^3$$

$$S_{\mathrm{PDFgetX}}(\boldsymbol{q}) - 1 = \rho\int_V g(\boldsymbol{r}) e^{-i\boldsymbol{q}\cdot\boldsymbol{r}}\, \mathrm{d}r^3 \; - \rho\, V\, \delta(\boldsymbol{q}). \tag{2.57}$$

The delta distribution ensures that $\delta(\boldsymbol{q}) = 1$ when $\boldsymbol{q} = 0$ and $\delta(\boldsymbol{q}) = 0$ when $q \neq 0$.

The "-1" term at "$S_{\mathrm{PDFgetX}}(\boldsymbol{q}) - 1$" of equation 2.56 represents the coherent self-scattering:

$$S_{\mathrm{PDFgetX}}(\boldsymbol{q}) = \frac{1}{N}\sum_{i,j} e^{-i\boldsymbol{q}\cdot\boldsymbol{r_{ji}}} = \frac{1}{N}\sum_{i\neq j} e^{-i\boldsymbol{q}\cdot\boldsymbol{r_{ji}}} + \frac{1}{N}\sum_{i=j} e^{-i\boldsymbol{q}\cdot\boldsymbol{r_{ji}}}$$

$$= \frac{1}{N}\sum_{i\neq j} e^{-i\boldsymbol{q}\cdot\boldsymbol{r_{ji}}} + 1$$

$$\Rightarrow S_{\mathrm{PDFgetX}}(\boldsymbol{q}) - 1 = \frac{1}{N}\sum_{i\neq j} e^{-i\boldsymbol{q}\cdot\boldsymbol{r_{ji}}}, \tag{2.58}$$

or in Debye notation of equation 2.45:

$$S_{\mathrm{Debye}}(q) - 1 = \frac{1}{N}\sum_{i\neq j} \frac{\sin(qr_{ji})}{qr_{ji}}. \tag{2.59}$$

Fourier-transforming "$g(\boldsymbol{r}) - 1$" should yield 2.58.
To proof this we first change the PDF 2.54 and the Fourier-integrals from $\boldsymbol{r}$ to a direction-independent r (only possible if the sample is isotropic, which is the case for our glass samples) to facilitate the calculations. Thus, we should obtain the Debye notation 2.59 of $S_{\mathrm{Debye}}(q)$.
For an isotropic $g(r)$ we are able to replace $\rho(\boldsymbol{r})$, where the r-dependency was omitted for the sake of clarity, with a homogeneous density ρ_0, known as number density:

$$\rho_0 = \frac{N}{V}, \tag{2.60}$$

where V is the volume of the sample and N the number of atoms within the sample. Furthermore we have to normalize $g(r)$ with $4\pi r^2$ and obtain:

$$g(r) = \frac{1}{4\pi r^2 \rho_0 N} \sum_{i \neq j} \delta(r - r_{ji}). \tag{2.61}$$

The expression $e^{i\boldsymbol{q}\cdot\boldsymbol{r}}$ for isotropic samples yields:

$$e^{i\boldsymbol{q}\cdot\boldsymbol{r}} = \int_0^{2\pi} \mathrm{d}\phi \int_0^{\pi} q^2 \sin\theta e^{iqr\cos\theta}\, \mathrm{d}\theta = 4\pi q \frac{\sin(qr)}{r}, \tag{2.62}$$

respectively, for the inverse transformation:

$$e^{i\boldsymbol{q}\cdot\boldsymbol{r}} = \int_0^{2\pi} \mathrm{d}\phi \int_0^{\pi} r^2 \sin\theta e^{iqr\cos\theta}\, \mathrm{d}\theta = 4\pi r \frac{\sin(qr)}{q}. \tag{2.63}$$

Hence, we are able to rewrite the Fourier-transformations from 2.55:

$$g(r) - 1 = \frac{1}{2\pi^2 r \rho_0} \int_q q \left(S_{\mathrm{Debye}}(q) - 1\right) \sin(qr)\, \mathrm{d}q. \tag{2.64}$$

The isotropic description of the inverse Fourier-transformation of equation 2.56 is:

$$S_{\mathrm{Debye}}(q) - 1 = \frac{4\pi\rho_0}{q} \int_r r \left(g(r) - 1\right) \sin(qr)\, \mathrm{d}r. \tag{2.65}$$

Inserting euation 2.61 into 2.65 for q $\neq 0$ (see therefore equation 2.57) yields:

$$S_{\mathrm{Debye}}(q) - 1 = \frac{4\pi\rho_0}{q} \int_r \left(\frac{1}{4\pi r^2 \rho_0} \sum_{i \neq j} \delta(r - r_{ji}) \right) r \sin(qr)\, \mathrm{d}r$$

$$S_{\mathrm{Debye}}(q) - 1 = \frac{1}{q} \int_r \sum_{i \neq j} \delta(r - r_{ji}) \frac{\sin(qr)}{r}\, \mathrm{d}r$$

$$S_{\mathrm{Debye}}(q) - 1 = \frac{1}{N} \sum_{i \neq j} \frac{\sin(qr_{ji})}{qr_{ji}}. \tag{2.66}$$

The solution for the case $q \neq 0$ is identical with the Debye notation of 2.59[6].

[6] Applying L'Hôpital's rule for the case of $q = 0$ yields:

$$\lim_{q\to 0} \sum_{i \neq j}^{N} \frac{(\sin(qr_{ji}))'}{(qr_{ji})'} = \lim_{q\to 0} \sum_{i \neq j}^{N} \frac{\cos(qr_{ji}) r_{ji}}{r_{ji}} = N(N-1)$$

$$\rightarrow S_{\mathrm{Debye}}(q) - 1 = \frac{1}{N} N(N-1) - \rho_0 V \delta(\boldsymbol{q} = 0) = \frac{1}{N} N(N-1) - N = -1,$$

would yield $S_{\mathrm{Debye}} = 0$. This is not correct! For monatomic systems the structure factor $S(q = 0)$ is:

$$S(q = 0) = \rho_0 \chi_T k_B T,$$

where χ_T is the isothermal compressibility, k_B the Boltzmann constant and T the absolute temperature. This useful thermodynamical limit needs other basics (see literature [26]).

2.5.2 The polyatomic case

We have to consider partial pair distribution functions $g_{\alpha\beta}(\boldsymbol{r})$ if our sample consists of more than one type of atom:

$$g_{\alpha\beta}(\boldsymbol{r}) = \frac{1}{\rho_\beta N_\alpha} \sum_{i_\alpha \neq j_\beta} \delta\left(\boldsymbol{r} - \boldsymbol{r_{j_\beta i_\alpha}}\right). \tag{2.67}$$

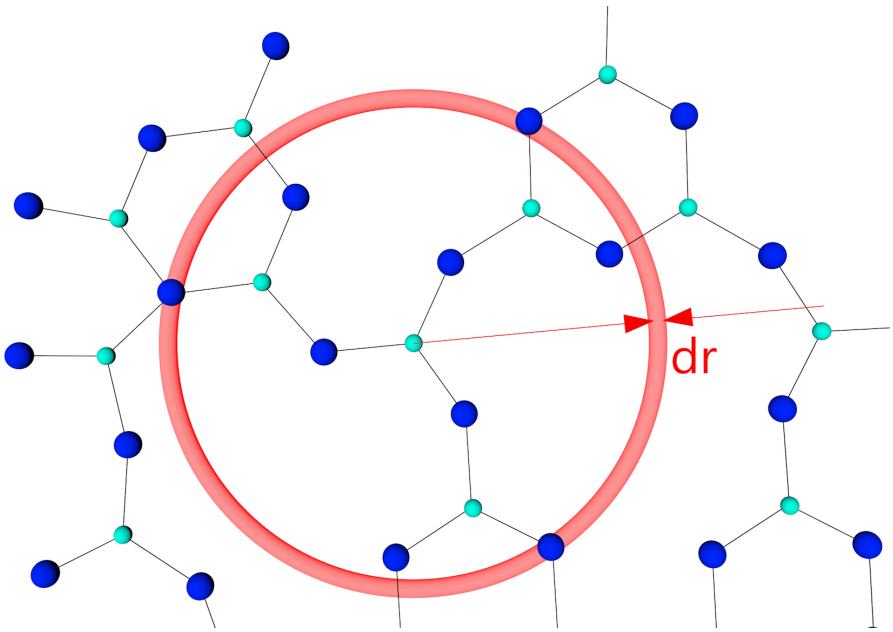

Figure 2.3: Construction of the PDF in a polyatomic system. Here we consider a borate glass structure. The reference atom is a boron atom. We are interested in the quantity of oxygen atoms surrounding this reference atom within a small interval Δr. The number density ρ_O has to be the number of oxygen atoms N_O times the volume V of the sample that is inverse proportional to the PDF g_BO. We are averaging over all boron atoms N_B. In this case we would get $g_\mathrm{OB}(\boldsymbol{r}) = \frac{1}{\rho_\mathrm{O} N_{\boldsymbol{B}}} \sum_{i_\mathrm{B} \neq j_\mathrm{O}} \delta\left(\boldsymbol{r} - \boldsymbol{r_{j_\mathrm{O} i_\mathrm{B}}}\right)$.

Metaphorically spoken we are counting the β-atoms surrounding one α-atom in every spherical shell, which corresponds to the delta-distribution $\delta\left(r - r_{j_\beta i_\alpha}\right)$. Therefore we have to set the density of the β-atoms ρ_β in relation to the delta distribution to obtain the probability of finding an β atom at a position $\boldsymbol{r}$ relative to a reference atom α. Averaging over all reference atoms α requires the number of α-atoms N_α. Again we can simplify the equation 2.67 due to isotropic behaviour of glass:

$$g_{\alpha\beta}(r) = \frac{1}{4\pi r^2 \rho_\beta N_\alpha} \sum_{i_\alpha \neq j_\beta} \delta\left(r - r_{j_\beta i_\alpha}\right). \tag{2.68}$$

This time ρ_β is the number density of β-atoms:

$$\rho_\beta = \frac{N_\beta}{V}, \tag{2.69}$$

where V is the volume of the sample.
Expanding equation 2.67 with $\rho_0 = N/V$ yields:

$$g_{\alpha\beta}(r) = \frac{\rho_0}{4\pi r^2 \rho_\beta \rho_0 N_\alpha} \sum_{i_\alpha \neq j_\beta} \delta\left(r - r_{j_\beta i_\alpha}\right) = \frac{\frac{N}{V}}{4\pi r^2 \frac{N_\beta}{V} \rho_0 \, N_\alpha} \sum_{i_\alpha \neq j_\beta} \delta\left(r - r_{j_\beta i_\alpha}\right)$$

$$= \frac{N}{N_\beta N_\alpha 4\pi r^2 \rho_0} \sum_{i_\alpha \neq j_\beta} \delta\left(r - r_{j_\beta i_\alpha}\right). \tag{2.70}$$

The partial PDF also exhibits symmetrical behaviour like the partial structure factor in equation 2.35:

$$g_{\alpha\beta}(r) = g_{\beta\alpha}(r). \tag{2.71}$$

The Fourier-transformation from the partial PDF $g_{\alpha\beta}(r)$ to the partial structure factor $S_{\alpha\beta}(q)$ still needs the number density ρ_0 as transformation measure:

$$g_{\alpha\beta}(r) - 1 = \frac{1}{2\pi^2 r \rho_0} \int_q q \left(S_{\text{Debye},\alpha\beta}(q) - 1\right) \sin(qr) \, \mathrm{d}q \tag{2.72}$$

$$S_{\text{Debye},\alpha\beta}(q) - 1 = \frac{4\pi\rho_0}{q} \int_r r \left(g_{\alpha\beta}(r) - 1\right) \sin(qr) \, \mathrm{d}r. \tag{2.73}$$

Inserting the partial PDF $g_{\alpha\beta}(r)$ from equation 2.70 into the equation 2.73 and following the same calculation procedure like we did it for the monatomic case leads to the partial structure factor $S_{\alpha\beta}(q)$ 2.32 for $q \neq 0$ with the non-intuitive prefactor $\frac{N}{N_\alpha N_\beta}$.

In principle, if we are evaluating our polyatomic samples experimentally, we have no access to the partial structure factors $S_{\alpha\beta}(q)$. We only gain the *Faber-Ziman* structure factor $S_{\text{FZ}}(q)$ via the evaluation program PDFgetX (see chapter 3.5), which contains all the partial structure factors. Fourier-transforming $S_{\text{FZ}}(q) - 1$ leads to $g_{\text{total}}(r) - 1$. Hence, the total pair distribution function (tPDF) $g_{\text{total}}(r)$ must be the counterpart of $S_{\text{FZ}}(q)$, containing all the partial PDFs $g_{\alpha\beta}(r)$.

$$\sum_{\alpha\beta} \left(g_{\alpha\beta}(r) - 1\right) = \sum_{\alpha\beta} \left(\frac{1}{2\pi^2 r \rho_0} \int_q q \left(S_{\text{Debye},\alpha\beta}(q) - 1\right) \sin(qr) \, \mathrm{d}q \right)$$

$$\sum_{\alpha\beta} \left(g_{\alpha\beta}(r) - 1\right) = \frac{1}{2\pi^2 r \rho_0} \int_q q \sum_{\alpha,\beta} \left(S_{\text{Debye},\alpha\beta}(q) - 1\right) \sin(qr) \, \mathrm{d}q.$$

Multiplying both sides with $\frac{f_{\text{at},\alpha} f_{\text{at},\beta} c_\alpha c_\beta}{\langle f_{\text{at}} \rangle^2}$ yields:

$$\sum_{\alpha\beta} \frac{f_{\text{at},\alpha} f_{\text{at},\beta} c_\alpha c_\beta}{\langle f_{\text{at}} \rangle^2} \left(g_{\alpha\beta}(r) - 1\right)$$

$$= \frac{1}{2\pi^2 r \rho_0} \int_q q \sum_{\alpha,\beta} \frac{f_{\text{at},\alpha} f_{\text{at},\beta} c_\alpha c_\beta}{\langle f_{\text{at}} \rangle^2} \left(S_{\text{Debye},\alpha\beta}(q) - 1\right) \sin(qr) \, \mathrm{d}q.$$

We are now defining $g_{\text{total}}(r)$:

$$g_{\text{total}}(r) = \sum_{\alpha\beta} \frac{f_{\text{at},\alpha} f_{\text{at},\beta} c_\alpha c_\beta}{\langle f_{\text{at}} \rangle^2} g_{\alpha\beta}(r). \tag{2.74}$$

With the definition of the *Faber-Ziman* structure factor $S_{\text{FZ}}(q)$ 2.36 we obtain:

$$g_{\text{total}}(r) - \sum_{\alpha\beta} \frac{f_{\text{at},\alpha} f_{\text{at},\beta} c_\alpha c_\beta}{\langle f_{\text{at}} \rangle^2}$$

$$= \frac{1}{2\pi^2 r \rho_0} \int_q q \left(S_{\text{FZ}}(q) - \sum_{\alpha,\beta} \frac{f_{\text{at},\alpha} f_{\text{at},\beta} c_\alpha c_\beta}{\langle f_{\text{at}} \rangle^2} \right) \sin(qr)\, \mathrm{d}q.$$

Due to $\sum_{\alpha\beta} \frac{f_{\text{at},\alpha} f_{\text{at},\beta} c_\alpha c_\beta}{\langle f_{\text{at}} \rangle^2} = \frac{\langle f_{\text{at}} \rangle^2}{\langle f_{\text{at}} \rangle^2} = 1$ we eventually gain:

$$g_{\text{total}}(r) - 1 = \frac{1}{2\pi^2 r \rho_0} \int_q q \left(S_{\text{FZ}}(q) - 1 \right) \sin(qr)\, \mathrm{d}q. \tag{2.75}$$

Note that we have made a forbidden step here: The atomic form factor f_{at} is still dependent on q: $f_{\text{at}}(q)$. Hence, multiplying both sides with $\frac{f_{\text{at},\alpha}(q) f_{\text{at},\beta}(q) c_\alpha c_\beta}{\langle f_{\text{at}}(q) \rangle^2}$ is not permitted. We have to create q-independent form factors, at least for the multiplication with $\sum_{\alpha\beta} \left(g_{\alpha\beta}(r) - 1 \right)$ to guarantee the validity of this calculation step.
Some authors [22] recommend the approximation $f_{\text{at}}(q) \sim f_{\text{at}}(q = 0) = Z$, thus we are able to replace all the atomic form factors with the atomic number Z:

$$g_{\text{total}}(r) = \frac{\sum_{\alpha\beta} f_{\text{at},\alpha} f_{\text{at},\beta} c_\alpha c_\beta}{\langle f_{\text{at}} \rangle^2} g_{\alpha\beta}(r) = \frac{\sum_{\alpha\beta} Z_\alpha Z_\beta c_\alpha c_\beta}{\left(\sum_{\alpha\beta} Z_\alpha Z_\beta c_\alpha c_\beta \right)} g_{\alpha\beta}(r). \tag{2.76}$$

Furthermore inserting the expression for $g_{\alpha\beta}(r)$ 2.70 leads to:

$$g_{\text{total}}(r) = \frac{1}{4\pi r^2 \rho_0 N} \frac{\sum_{\alpha\beta} Z_\alpha Z_\beta}{\left(\sum_{\alpha\beta} Z_\alpha Z_\beta c_\alpha c_\beta \right)} \sum_{i_\alpha \neq j_\beta} \delta \left(r - r_{j_\beta i_\alpha} \right). \tag{2.77}$$

2.6 Radial distribution function (RDF)

The monatomic radial distribution function RDF_{mon} is defined by:

$$RDF_{\text{mon}}(r) = 4\pi r^2 \rho_0\, g(r) = \frac{1}{N} \sum_{i \neq j} \delta(r - r_{ji}). \tag{2.78}$$

The monatomic RDF_{mon} corresponds to the unnormalized $g(r)$. At small r the function is fluctuating around $4\pi r^2 \rho_0$ and for $r \to \infty$ (with $g(r \to \infty) = 1$) it finally adjust to the quadratic curve $4\pi r^2 \rho_0$ due to the missing long-range order.
For the polyatomic case the definition of the RDF stays the same except of changing the $g(r)$ into $g_{\text{total}}(r)$, respectively into $g_{\alpha\beta}(r)$ if a partial $RDF_{\alpha\beta}(r)$ is of interest:

$$RDF_{\text{poly}}(r) = 4\pi r^2 \rho_0 \, g_{\text{total}}(r) = \frac{1}{N} \frac{\sum_{\alpha\beta} Z_\alpha Z_\beta}{\left(\sum_{\alpha\beta} Z_\alpha Z_\beta c_\alpha c_\beta\right)} \sum_{i_\alpha \neq j_\beta} \delta\left(r - r_{j_\beta i_\alpha}\right) \tag{2.79}$$

$$RDF_{\alpha\beta}(r) = 4\pi r^2 \rho_0 \, g_{\alpha\beta}(r) = \frac{N}{N_\alpha N_\beta} \sum_{i_\alpha \neq j_\beta} \delta\left(r - r_{j_\beta i_\alpha}\right). \tag{2.80}$$

Due to $g_{\text{total}}(r \to \infty) = 1$ and $g_{\alpha\beta}(r \to \infty) = 1$, $RDF_{\text{poly}}(r)$ and $RDF_{\alpha\beta}(r)$ converge to $4\pi r^2 \rho_0$ for large r as in the monatomic case.

2.7 Coordination number

The first coordination number of a central atom is the number of its nearest neighbours. The second coordination number is the number of its next nearest neighbours and so on.
In crystalline substances counting the nearest neighbours yield the first coordination number. In disordered materials the coordination number is rather an average of nearest neighbours and is defined as:

$$\bar{n} = \int_{r_1}^{r_2} RDF(r) \, \mathrm{d}r = 4\pi\rho_0 \int_{r_1}^{r_2} g(r) r^2 \, \mathrm{d}r. \tag{2.81}$$

This average corresponds to an integration over the first coordination shell $[r_1, r_2]$ of the unnormalized $g(r)$. The first coordination shell is a spherical shell around the central atom. In fluids there exists only the first coordination shell because of their short-range order. In intermediate-range order materials like glass it is possible to define a second $[r_2, r_3]$, a third $[r_3, r_4]$,..., a n-th coordination shell $[r_n, r_{n+1}]$, whereby $n \neq \infty$ regarding its limited order.

If we integrate from 0 to ∞ we expect as a result the number of atoms except of the reference atom, thus:

$$\bar{n} = 4\pi\rho_0 \int_0^\infty g(r) r^2 \, \mathrm{d}r = N - 1. \tag{2.82}$$

Entering $g(r)$ 2.61 should lead to this prediction:

$$\begin{aligned} \bar{n} &= 4\pi\rho_0 \int_0^\infty \left(\frac{1}{4\pi r^2 \rho_0 N} \sum_{i \neq j} \delta(r - r_{ji}) \right) r^2 \, \mathrm{d}r \\ &= \frac{1}{N} \sum_{i \neq j} \delta(r - r_{ji}) = \frac{1}{N} N(N-1) = N - 1. \end{aligned}$$

In the case of a polyatomic system we should gain:

$$\bar{n}_\alpha^\beta = 4\pi\rho_0 \, x \int_0^\infty g_{\alpha\beta}(r) r^2 \, \mathrm{d}r = N_\beta. \tag{2.83}$$

This time there is no symmetry between $\bar{n}_\alpha^\beta$ and $\bar{n}_\beta^\alpha$:

$$\bar{n}_\alpha^\beta \neq \bar{n}_\beta^\alpha. \tag{2.84}$$

The coordination number $\bar{n}_\alpha^\beta$ expresses the α-atom as reference atom and the β-atoms as neighbours. So we obtain the averaged β-atom neighbourhood of an α-atom if we calculate $\bar{n}_\alpha^\beta$. Taking the β-atom as reference atom and looking for the surrounding α-atoms yields a different result $\bar{n}_\beta^\alpha$. The x in equation 2.83 stands for the missing factor that has to be determined when integrating from 0 to ∞. In the case of $\bar{n}_\alpha^\beta$ this leads to the entire amount of surrounding β-atoms: N_β.
Determining the missing factor x:

$$\begin{aligned}
\bar{n}_\alpha^\beta &= 4\pi\rho_0\, x \int_0^\infty \left(\frac{N}{N_\alpha N_\beta 4\pi r^2 \rho_0} \sum_{i_\alpha \neq j_\beta} \delta\left(r - r_{j_\beta i_\alpha}\right) \right) r^2 \,\mathrm{d}r \\
&= x \frac{N}{N_\alpha N_\beta} \sum_{i_\alpha \neq j_\beta} \delta\left(r - r_{j_\beta i_\alpha}\right) \\
&= x \frac{N}{N_\alpha N_\beta} N_\alpha N_\beta = xN \stackrel{!}{=} N_\beta \\
&\Rightarrow x = N_\beta / N = c_\beta.
\end{aligned} \tag{2.85}$$

Finally for the first coordination shell of a polyatomic system we obtain

$$\bar{n}_\alpha^\beta = 4\pi\rho_0\, c_\beta \int_{r_1}^{r_2} g_{\alpha\beta}(r) r^2 \,\mathrm{d}r, \tag{2.86}$$

respectively

$$\bar{n}_\beta^\alpha = 4\pi\rho_0\, c_\alpha \int_{r_1}^{r_2} g_{\alpha\beta}(r) r^2 \,\mathrm{d}r. \tag{2.87}$$

Thus, the coordination numbers $\bar{n}_\alpha^\beta$ and $\bar{n}_\beta^\alpha$ are connected with the concentration c_β, respectively c_α:

$$\frac{\bar{n}_\alpha^\beta}{c_\beta} = \frac{\bar{n}_\beta^\alpha}{c_\alpha}. \tag{2.88}$$

2.8 Difficulties in polyatomic systems

In general, if no computer simulation is implemented imitating the structure of the sample, there is no access to the partial structure factors $S_{\alpha\beta}(q)$ and hence no access to the partial PDFs $g_{\alpha\beta}(r)$. Without the partial PDF one has no information about the structural arrangements of the individual atoms.
In practice, experimental results for diffraction by liquids and glasses should be compared with theory and simulation in both r-space and q-space, as well as with results from other experimental techniques, so as to obtain the possibility of understanding the structure [10].

In the case of alkali borate glasses, there already exists knowledge of the structure that allows us making a useful comparison with our results. Additionally simulations were performed in our group that helps restricting unknown variables [26].
For instance, we are able to calculate the coordination number of the first coordination shell, because we know from literature and simulation results that the next-nearest neighbours of boron atoms are oxygen atoms and vice versa. There are no other type of atoms within this distance. Hence, the first peak of $g_{\mathrm{total}}(r)$ only consists of g_{OB}, respectively g_{BO}. The other partial PDFs are approximately zero. Eventually we are able to calculate $\bar{n}_{\mathrm{B}}^{\mathrm{O}}$, respectively $\bar{n}_{\mathrm{O}}^{\mathrm{B}}$ in this area. Using 2.76 we obtain:

$$g_{\mathrm{total}}(r) = \frac{1}{\langle Z\rangle^2}\Bigg(Z_{\mathrm{O}}^2 c_{\mathrm{O}}^2 g_{\mathrm{OO}}(r) + Z_{\mathrm{B}}^2 c_{\mathrm{B}}^2 g_{\mathrm{BB}}(r) + Z_{\mathrm{A}}^2 c_{\mathrm{A}}^2 g_{\mathrm{AA}}(r)$$
$$+ 2Z_{\mathrm{O}} Z_{\mathrm{B}} c_{\mathrm{O}} c_{\mathrm{B}} g_{\mathrm{OB}}(r) + 2Z_{\mathrm{O}} Z_{\mathrm{A}} c_{\mathrm{O}} c_{\mathrm{A}} g_{\mathrm{OA}}(r) + 2Z_{\mathrm{B}} Z_{\mathrm{A}} c_{\mathrm{B}} c_{\mathrm{A}} g_{\mathrm{BA}}(r)\Bigg). \tag{2.89}$$

The index A is denoted as alkali atom. In the area $[r_1, r_2]$ that includes the nearest neighbours NN (BO(1) or OB(1)), the equation 2.89 reduces to:

$$g_{\mathrm{total}}^{\mathrm{NN}}(r) = \frac{1}{\langle Z\rangle^2} 2Z_{\mathrm{O}} Z_{\mathrm{B}} c_{\mathrm{O}} c_{\mathrm{B}} g_{\mathrm{OB}}^{\mathrm{NN}}(r). \tag{2.90}$$

Hence we are able to obtain an expression for the partial structure factor $g_{\mathrm{OB}}^{\mathrm{NN}}(r)$ in the area $[r_1, r_2]$:

$$g_{\mathrm{OB}}^{\mathrm{NN}}(r) = \frac{g_{\mathrm{total}}^{\mathrm{NN}}(r)\langle Z\rangle^2}{2Z_{\mathrm{O}} Z_{\mathrm{B}} c_{\mathrm{O}} c_{\mathrm{B}}}. \tag{2.91}$$

Inserting this expression into the equation for the polyatomic coordination number 2.86 yields:

$$\bar{n}_{\mathrm{B}}^{\mathrm{O}} = 4\pi\rho_0\, c_{\mathrm{O}} \int_{r_1}^{r_2} g_{\mathrm{OB}}^{\mathrm{NN}}(r) r^2\, \mathrm{d}r$$
$$\bar{n}_{\mathrm{B}}^{\mathrm{O}} = \frac{2\pi\rho_0\langle Z\rangle^2}{Z_{\mathrm{O}} Z_{\mathrm{B}} c_{\mathrm{B}}} \int_{r_1}^{r_2} g_{total}^{\mathrm{NN}}(r) r^2\, \mathrm{d}r, \tag{2.92}$$

and

$$\bar{n}_{\mathrm{O}}^{\mathrm{B}} = 4\pi\rho_0\, c_{\mathrm{B}} \int_{r_1}^{r_2} g_{\mathrm{OB}}^{\mathrm{NN}}(r) r^2\, \mathrm{d}r$$
$$\bar{n}_{\mathrm{O}}^{\mathrm{B}} = \frac{2\pi\rho_0\langle Z\rangle^2}{Z_{\mathrm{O}} Z_{\mathrm{B}} c_{\mathrm{O}}} \int_{r_1}^{r_2} g_{total}^{\mathrm{NN}}(r) r^2\, \mathrm{d}r, \tag{2.93}$$

with

$$\langle Z\rangle^2 = \sum_{\alpha\beta} Z_\alpha Z_\beta c_\alpha c_\beta$$
$$= Z_{\mathrm{O}}^2 c_{\mathrm{O}}^2 + Z_{\mathrm{B}}^2 c_{\mathrm{B}}^2 + Z_{\mathrm{A}}^2 c_{\mathrm{A}}^2$$

$$+2Z_{\mathrm{O}}Z_{\mathrm{B}}c_{\mathrm{O}}c_{\mathrm{B}} + 2Z_{\mathrm{O}}Z_{\mathrm{A}}c_{\mathrm{O}}c_{\mathrm{A}} + 2Z_{\mathrm{B}}Z_{\mathrm{A}}c_{\mathrm{B}}c_{\mathrm{A}}$$
$$= \left(Z_{\mathrm{O}}c_{\mathrm{O}} + Z_{\mathrm{B}}c_{\mathrm{B}} + Z_{\mathrm{A}}c_{\mathrm{A}}\right)^2 . \tag{2.94}$$

This uniqueness belongs only to the first coordination shell. The tPDF $g_{\mathrm{total}}(r)$ for other r-regions is always a composition of more than one unknown partial structure factor $g_{\alpha\beta} \neq 0$.
Hence, the other coordination shells could not be distinctively assigned to particular atom pairs.

Chapter 3

Experimental approach

3.1 Sample preparation

The aim is to analyse and compare diffraction experiments of alkali borate glasses with different alkali concentrations. The alkalis that were incorporated ranges from the lightest atom, lithium to the heaviest, caesium. Different alkali borate glass samples were already prepared in our group. We additionally prepared 15 g of $10Cs_2O\ 90B_2O_3$ to extend the existing sample collection:

alkali element	low alkali concentration	high alkali concentration
lithium	$5Li_2O\ 95B_2O_3$	$20Li_2O\ 80B_2O_3$
sodium	$5Na_2O\ 95B_2O_3$	$20Na_2O\ 80B_2O_3$
potassium	$5K_2O\ 95B_2O_3$	$20K_2O\ 80B_2O_3$
rubidium	$2Rb_2O\ 98B_2O_3$	$15Rb_2O\ 85B_2O_3$
caesium	$2Cs_2O\ 98B_2O_3$	$15Cs_2O\ 85B_2O_3$

Table 3.1: The existing alkali borate glass collection.

The raw material used are boron oxide[1] B_2O_3 and caesium carbonate[2] Cs_2CO_3. The raw material exists in powder form and is separately weighted to obtain the correct proportion and afterwards thoroughly mixed together. Bit by bit the mixed powder is tipped into a crucible that is surrounded by a furnace system. During the melting process, the reaction

$$Cs_2CO_3 \Longrightarrow CO_2 + Cs_2O \tag{3.1}$$

takes place. The carbon dioxide CO_2 vaporizes, whereas the caesium carbonate and boron oxide form a homogeneous melt. The tendency of gas inclusions is decreased by stirring at regular time steps. When the melt seems to be bubble free, the crucible is emptied quickly into a circular immersion on top of a brass cylinder kept at

[1] 99.98% purity, total metal impurity: max. 0.02%, CAS: 1303-86-2
[2] 99.94% purity, total metal impurity: max. 0.06%, CAS: 534-17-8

room temperature emulating a fast cooling procedure.

Due to the chemical reaction 3.1 the weighting fraction of the material for the glass component Cs_2O has to be multiplied by the gravimetric factor given as the ratio between the atomic weights of the raw material and the respective glass component [26]:

$$\text{gravimetric factor} = \frac{\text{raw material}}{\text{material for glass component}}. \tag{3.2}$$

Thus, for the case of 15 g from $10Cs_2O\ 90B_2O_3$ we need:

$$15\text{ g} \times \frac{0.1\ Cs_2O\text{ g}}{\text{entire mass g}} \times \text{gravimetric factor}, \tag{3.3}$$

and

$$15\text{ g} \times \frac{0.9\ B_2O_3\text{ g}}{\text{entire mass g}}, \tag{3.4}$$

where the gravimetric factor and the entire mass is:

$$\text{gravimetric factor} = \frac{Cs_2CO_3\text{ g}}{Cs_2O\text{ g}} \tag{3.5}$$

$$\text{entire mass} = 0.1\ Cs_2O\text{ g} + 0.9\ B_2O_3\text{ g}. \tag{3.6}$$

Depending on the X-ray diffractometer, the glass is either cut into platelets of appropriate thickness or ground into powder for the application in powder diffraction experiments. Due to the hygroscopy of borate glasses the samples should be stored in airtight containers in addition to the use of a drying agent.
Despite the careful storage, inclusions of hydrogen, above all in powder samples, are hard to avoid. The more surface the sample is offering, which is the case of many small grains instead of a bulk sample, the more hydrogen atoms could connect to the glass structure and is partly responsible for an unwanted recrystallization process noticeable as Bragg peaks at the intensity-curve. Additionally the inconvenient manufacturing method of powder samples (glass capillary filled with powder) favours the contact with air: We pestled glass pieces in a ceramic mortar. Depending on the alkali type and the alkali concentration the pestling was short and easy or very tedious. Therefore we put the mortar in a styrofoam container filled with nitrogen at room temperature replacing the air. Afterwards we spooned the powder into a soda glass capillary with a diameter of 1 mm and finally melted the opening of the capillary via a lighter. At the beginning we performed this manufacturing steps in air, then we switched to an argon filled glove bag, but the usage of a glove bag did not improve our results concerning hydrogen contaminations.
Besides we think that during a long storage the crystallization process progresses. This is noticeable when two time-displaced measurements were performed with the same capillary. The structure changes dramatically from amorphous to an amorphous background plus distinct crystalline features. The question is if the capillary is leaky or if the existing hydrogen atoms inside the capillary due to imperfect manufacturing, slowly form crystallites. The manufacturing of bulk samples requires less

care. Shortly before a diffraction experiment takes place the glass platelets have to be treated with sandpaper and ethanol to get rid of a white haze (that emerge due to hydrogen crystallization processes) and some dirt on the surface and are cut and polished.

The powder samples were used for the *PANalytical instrument* at the TU Wien. The bulk samples were used for *Petra III* at DESY (Deutsches Elektronen Synchrotron) in Hamburg.

Measuring the masses m of our samples and calculating the density ρ via Archimedes' method is necessary for obtaining the number density ρ_0 and eventually the tPDF $g_{\text{total}}(r)$. The derivation of Archimedes' method and the density results can be found in the appendix A.

The calculation of the number density ρ_0 is demonstrated in the case of $10Cs_2O\,90B_2O_3$.

Choosing numbers of boron atoms, oxygen atoms and caesium atoms matching the proportion of $10Cs_2O\,90B_2O_3$ and calculating the corresponding mass m_{atoms} and the volume V with the knowledge of the density ρ yields ρ_0:

$$N_{\text{atoms}} = (90 \times 2)\ \text{B} + (90 \times 3 + 10)\ \text{O} + (10 \times 2)\ \text{Cs} = 480\ \text{atoms} \tag{3.7}$$

$$\begin{aligned} m_{\text{atoms}} &= \big(180\ \text{B} \times 10.81\ \text{u} + 280\ \text{O} \times 15.999\ \text{u} + 20\ \text{Cs} \times 132.91\ \text{u}\big) \\ &\quad \times 1.66053904020 \times 10^{-27}\ \text{kg} = 1.50839 \times 10^{-23}\ \text{kg}. \end{aligned} \tag{3.8}$$

Note the conversion factor from u to kg:

$$1\ \text{u} = 1.66053904020 \times 10^{-27}\ \text{kg}$$

$$V = \frac{m_{\text{atoms}}\ [\text{kg}]}{\rho\ [\text{kg/m}^3]} = \frac{1.50839 \times 10^{-23}\ \text{kg}}{2364\ \text{kg/m}^3} = 6.38067 \times 10^{-27}\ \text{m}^3 \tag{3.9}$$

$$\begin{aligned} \rho_0 = \frac{N_{\text{atoms}}}{V} &= \frac{480\ \text{atoms}}{6.38067 \times 10^{-27}\ \text{m}^3} = 7.5227 \times 10^{28}\ \frac{1}{\text{m}^3} \\ &= 0.075227\ \frac{1}{\text{Å}^3}. \end{aligned} \tag{3.10}$$

The number density ρ_0 of all samples:

sample	ρ_0 [1/Å^3]	sample	ρ_0 [1/Å^3]
$5Li_2O\,95B_2O_3$	0.083	$20Li_2O\,80B_2O_3$	0.095
$5Na_2O\,95B_2O_3$	0.084	$20Na_2O\,80B_2O_3$	0.110
$5K_2O\,95B_2O_3$	0.081	$20K_2O\,80B_2O_3$	0.079
$2RB_2O\,98B_2O_3$	0.082	$15RB_2O\,85B_2O_3$	0.074
$2Cs_2O\,98B_2O_3$	0.078	$10Cs_2O\,90B_2O_3$	0.075
$15Cs_2O\,85B_2O_3$	0.065		

Table 3.2: Number densities ρ_0 of $xA_2O\ (100-x)B_2O_3$.

3.2 X-ray scattering techniques

Scattering techniques were developed in the early 20^{th} century when X-rays were proven to be electro-magnetic waves with wavelength of about $\lambda \approx 10^{-9}$ m [26]. X-ray scattering reveals information about the crystalline, respectively amorphous structure, chemical compositions and physical properties of materials.
Scattering techniques can be categorized into techniques with **elastic scattering**, where $|\boldsymbol{k}_{\mathbf{inc}}| = |\boldsymbol{k}_{\mathbf{scat}}|$ and the structure factor $S(\boldsymbol{q})$ only depends on $\boldsymbol{q}$. Examples are:

- Wide-angle X-ray scattering (WAXS): Probes structure in an interval of $(10^{-10} - 10^{-9})$ m by measuring the intensity of a large q-range,
- Small-angle X-ray scattering (SAXS): Probes structure in an interval of $(10^{-9} - 10^{-6})$ m by measuring the intensity of q close to 0°.
- X-ray reflectivity: Is an analytic technique for determining thickness, roughness and density of single layer and multilayer thin films,

and **inelastic scattering**, where $|\boldsymbol{k}_{\mathbf{inc}}| \neq |\boldsymbol{k}_{\mathbf{scat}}|$ and the structure factor $S(\boldsymbol{q}, \omega)$ depends on $\boldsymbol{q}$ and ω. Examples are:

- Compton scattering: Information on Fermi surface shape
- Resonant inelastic X-ray scattering (RIXS): Information on electronic structure and excitations,
- Non-resonant inelastic X-ray scattering (NRIXS): Information on electronic structure and excitations,
- X-ray Raman scattering: Information on absorption edge structure, bonding, valence,

- High-resolution inelastic X-ray scattering (HRIXS): Information on atomic dynamics, phonon dispersion.

The intermediate-range order of $x\mathrm{A_2O}$ $(100-x)\mathrm{B_2O_3}$ occurs at distances of 10^{-10} m, consequently our measurements have to be WAXS-experiments.

Regarding figure 2.1 or figure 3.1 the scattered intensity $I(\theta)$ is collected with the diffraction angle θ that relates to the absolute value of the scattering vector q. Via the Bragg and the Laue condition a relation between scattering vector q and diffraction angle $\frac{\theta}{2}$ is deducible:

$$\text{Bragg's law:}\quad n\lambda = 2d\sin\left(\frac{\theta}{2}\right), \tag{3.11}$$

where λ is the wavelength of the incident beam, n is an integer (corresponding to the n-th diffraction order) and d is the distance between two coplanar lattice planes. Constructive interference appears only if the Laue condition is fulfilled:

$$G = q. \tag{3.12}$$

G is the absolute value of the reciprocal lattice vector. The lattice plane distance d is expressed by the inverse of G:

$$d = \frac{2\pi}{|h\boldsymbol{b_1} + k\boldsymbol{b_2} + l\boldsymbol{b_3}|} = \frac{2\pi}{G} = \frac{2\pi}{q}. \tag{3.13}$$

Thus, the correlation between $\frac{\theta}{2}$ and q is given by:

$$n\lambda = 2\left(\frac{2\pi}{q}\right)\sin\left(\frac{\theta}{2}\right) \rightarrow q = \frac{4\pi\sin\left(\frac{\theta}{2}\right)}{\lambda}. \tag{3.14}$$

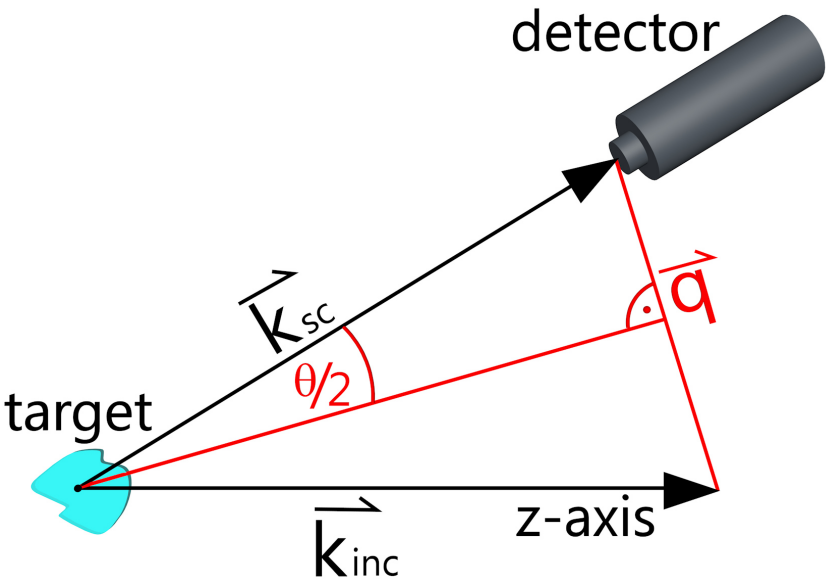

Figure 3.1: Geometrical illustration of $q(\theta/2)$.

Another geometrical derivation of $q(\theta/2)$:

$$\frac{q}{2} = k_{\text{inc}} \sin\left(\frac{\theta}{2}\right) \tag{3.15}$$

$$k_{\text{inc}} = \frac{2\pi}{\lambda} \rightarrow q = \frac{4\pi}{\lambda} \sin\left(\frac{\theta}{2}\right). \tag{3.16}$$

In figure 3.2 the actual experimental setup at the *PANalytical* instrument is shown. As one can see instead of θ an angle of 2θ is marked between the incident beam and the scattered one. These so-called 2θ-measurements have a fixed source and a fixed target. Only the detector is moving from 2θ near $0°$ to large values of 2θ (in our case $2\theta_{\text{max}}$ was approximately $130°$). The detector measures in 2θ-steps. Therefore the conversion to the absolute value of q is:

$$q = \frac{4\pi \sin\theta}{\lambda}. \tag{3.17}$$

Basically it is preferable to have a large q-range that is on the one hand achieved by a large 2θ-range and on the other hand by a high energy incident beam with small λ. We used different sources:

Where	Source	λ [Å]	E [keV]
TU Wien	Ag	0.5608	22.1085
TU Wien	Cu	1.5431	8.0347
DESY Hamburg	synchrotron radiation	0.2067	59.9827

Table 3.3: Wavelength λ and energy E of the incident beam from various sources.

The energy E is defined as:

$$E = \frac{hc}{\lambda} \tag{3.18}$$

The Cu-anode was inappropriate. It yields a $q_{\max}$ of 7.381 Å^{-1}, which was a too short range for a meaningful PDF $g_{\text{total}}(r)$.

Available detectors scanning the intensity $I(2\theta)$ are point detectors, line detectors and area detectors.
As one can imagine point detector-measurements are the most
time-consuming measurements. The detector has to stay for a certain time at the same angle with respect to the sample as to guarantee a good signal-to-noise ratio. One measurement at the *PANalytical* instrument took approximately 24 h. The line detector is able to scan more points at once, hence less time is needed for one sample measurement (approximately 12 h for one measurement at the *PANalytical* instrument). The area detector we used at Petra III was fixed positioned. Due to the large area of the detector itself a 2θ-movement in relation to the target was not necessary. A short exposure was sufficient to achieve a large q-range and a good signal-to-noise ratio.
The glass samples produce diffuse diffraction rings (Debye-Scherrer rings) due to the random orientation inside the glass. Via the program *FIT2D* this rings with the intensity $I(2\theta, \phi)$ were integrated over ϕ to gain the averaged intensity $I(2\theta)$.

3.3 PANalytical instrument

Powder diffraction 2θ-measurements were carried out by the *PANalytical* instrument at the TU Wien. Using glass capillaries require a transmission geometry, also known as Debye-Scherrer geometry.
The capillary filled with powder is constantly spinning during the measurement to get an additional average over all incident directions.
Before a measurement starts one has to align the capillary with the capillary holder, also called "spinner". The alignment should be done with respect to rotation and translation, otherwise the capillary is adversely wobbling falsifying the results. A

camera, displaying an optical magnification of the capillary with an overlaying cross hair, is provided in the *PANalytical* software for the alignment.

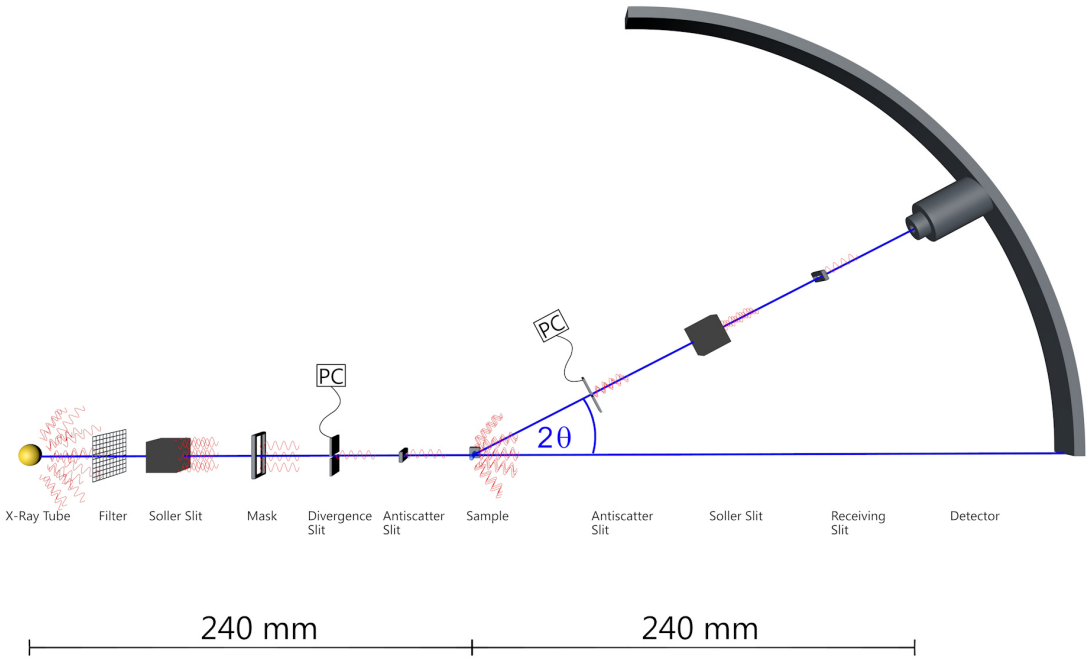

Figure 3.2: The experimental setup for a 2θ-measurement at the *PANalytical* instrument with an Ag-source and a scintillator detector. The assembly from left to right: Source, filter, soller slit, mask, programmable divergence slit, anti-scatter slit, capillary, programmable antiscatter slit, soller slit, receiving slit, detector.

Figure 3.2 shows the typical configuration we used in combination with a scintillation detector (point detector) and an Ag-anode. The Ag-anode requires a rhodium beta-filter cutting out the κ_β- wavelength of 0.4970 Å. The wavelength λ of the actual incident beam is composed by $\frac{2}{3}$ of the $\kappa_{\alpha 1}$-wavelength and $\frac{1}{3}$ of the $\kappa_{\alpha 2}$-wavelength:

$$\lambda = \frac{2}{3}\kappa_{\alpha 1} + \frac{1}{3}\kappa_{\alpha 2} \tag{3.19}$$

$$\lambda_{Ag} = \frac{2}{3}0.55942\ \text{Å} + \frac{1}{3}0.56381\ \text{Å} = 0.5608\ \text{Å}. \tag{3.20}$$

The wavelength $\kappa_{\alpha 1}$ and $\kappa_{\alpha 2}$ for a Cu-anode is:

$$\lambda_{Cu} = \frac{2}{3}1.540598\ \text{Å} + \frac{1}{3}1.544426\ \text{Å} = 1.5431\ \text{Å}. \tag{3.21}$$

The soller slit collimates the beam. Non-parallel rays are blocked by a very tight arrangement of thin metal plates, so-called lamellaes, with an opening angle of 0.04 rad.

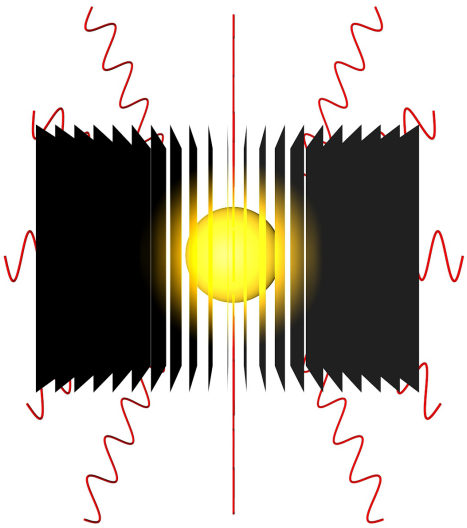

Figure 3.3: Soller slit for collimated light.

The continuing parallel rays were restricted in the y-direction via the mask and in the x-direction via the divergence slit and anti-scatter slit. On the diffracted side of the beam there is a similar arrangement focusing the rays to the detector.
The divergence slit on the left side and the anti-scatter slit on the right side have to be set by the *PANalytical* software, whereas the other slits have to be set manually. For a maximum illumination of the capillary the heights of the slits should be adjusted adequately. The slit height depends on the distance to the sample and on the capillary dimensions. The capillaries used have a diameter of 1 mm, hence the programmable divergence slit on the left side and the programmable anti-scatter slit on the right side that are both 140 mm away from the target center, should have a maximum height of 0.436 mm due to an opening angle of $\alpha = 0.25°$. Otherwise the beam spills over the capillary and produces unwanted diffraction of the environment. Too less slit height means a waste of intensity, because only a small area within the capillary gets illuminated.
Taking one scan of an absorption-profile of the capillary before a measurement series starts, is advisable to check the adequacy of the beam components.

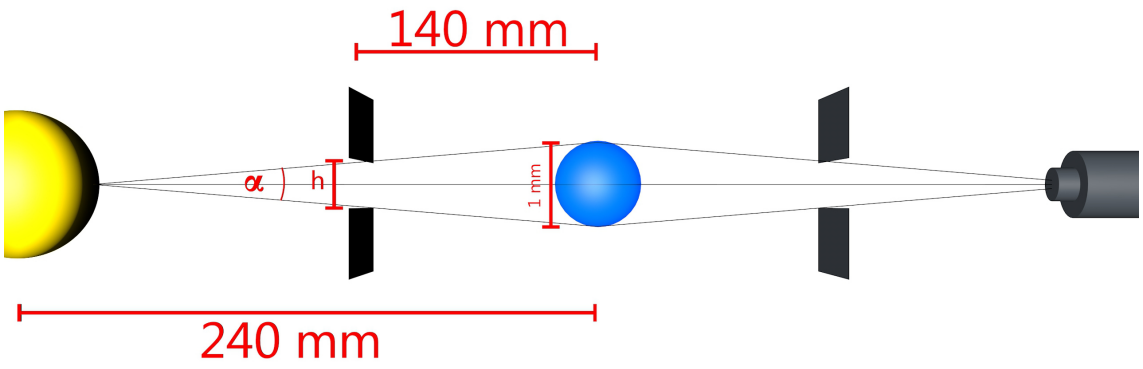

Figure 3.4: The opening angle of the beam is $\alpha = 0.25°$. The distance source until capillary,respectively detector until capillary is 240 mm and the distance divergence slit until capillary on the left side, respectively anti-scatter slit until capillary on the right side is 140 mm. From theses values the adequate slit height h can be determined.

3.4 Petra III

We operated at the beamline $P02.1$ for high-resolution and high-energy diffraction experiments. Bulk samples were prepared and simply fixed at the edges via tape on a metal plate. The metal plate was placed perpendicular with respect to the incident beam.
Due to transmission geometry the sample covered a small hole in the metal plate, where the beam propagated through and eventually hit an area detector. Due to the high energy of 60 keV of the beam, the absorption coefficient of our thin glass samples did not play a role.
To create optimal coherent and monochromatic light for diffraction the beam has to travel through diverse optical elements: An undulator produces synchrotron X-ray radiation that propagates through a slit system and two monochromator crystals, one mode of diamond and another of silicon. While the first slit system defines the beam size, the second one acts as a clean-up slit, before the beam penetrates the sample.

An aligned laser for optical pre-positioning of the specimen is also provided.
The detector as well as the sample table are mounted on a structural rail system for easy movement along the beam axis. The sample table is additionally mobile in the vertical axis [7].
All this devices are located in a so-called experimental hutch. Before a measurement starts, one has to leave this area for safety reasons. The evaluation is done in a different hutch, which belongs to that beamline $P02.1$.

We performed two measurements: During the first measurement series we placed the area detector very close to the specimen to gain a wide angle resolution, afterwards we placed it far away to gain a small angle resolution. Finally we were able to patch up both curves and obtained an $I(q)$-diagram with a large q-range.

3.5 Evaluation software PDFgetX

The software packages PDFgetX2 [23] and PDFgetX3 [15] were used for evaluating the raw data. PDFgetX2 as well as PDFgetX3 require the measured intensity $I_{\mathrm{M}}(q)$ and the background intensity $I_{\mathrm{B}}(q)$ for the output data. They produce four output-files:

- **file.iq**: Intensity $I(q)$ versus scattering vector q

  The program converts the angle 2θ to the scattering vector q. Therefore the presetting of the wavelength λ is necessary, see equation 3.14. The intensity $I(q)$ can be expressed by:

$$I(q) = I_{\mathrm{M}}(q) - I_{\mathrm{B}}(q). \tag{3.22}$$

  For calculating the structure factor $S_{\mathrm{FZ}}(q)$, the intensity $I_{\mathrm{scat}}(q)$ is needed that is modified by more correction terms than just the background scattering

$I_{\mathrm{B}}(q)$. $I_{\mathrm{scat}}(q)$ is a completely "cleaned-up" version of the intensity, which should contain only the structural information[3].

$$I_{\mathrm{M}}(q) = a(q)I_{\mathrm{scat}}(q) + b(q). \tag{3.23}$$

The parameter $a(q)$ and $b(q)$ are multiplicative and additive corrections to the measured intensity. Examples of the additive contributions are incoherent Compton scattering and background scattering from the sample container. Examples of the multiplicative contributions are sample self-absorption and polarization of the X-ray beam [15].

- **file.sq**: *Faber-Ziman* structure factor $S_{\mathrm{FZ}}(q)$ versus scattering vector q

  The *Faber-Ziman* structure factor $S_{\mathrm{FZ}}(q)$ is described by 2.43. Hence, the types of atoms and the respective concentrations have to be specified, so that the program is able to calculate with the correct atomic form factors $f_{\mathrm{at}}(q)$.

- **file.fq**: Reduced structure factor $F(q)$ (also known as reduced structure function) versus scattering vector q

  The reduced structure factor is defined as:

$$F(q) = q\left(S_{\mathrm{FZ}}(q) - 1\right). \tag{3.24}$$

  $F(q)$ should oscillate around zero and approaches it with increasing q.

- **file.gr**: Density function $D(r)$ versus radial distance r

  The data ending **.gr** causes confusion due to $g_{\mathrm{total}}(r)$. The density function $D(r)$ does not equal to the tPDF $g_{\mathrm{total}}(r)$ and is defined as:

$$\begin{aligned} D(r) &= \frac{2}{\pi}\int_q q\left(S_{\mathrm{FZ}}(q) - 1\right)\sin(qr)\,\mathrm{d}q \\ &= \frac{2}{\pi}\int_q F(q)\sin(qr)\,\mathrm{d}q. \end{aligned} \tag{3.25}$$

  The relation between $g_{\mathrm{total}}(r)$ and $D(r)$ is:

$$D(r) = 4\pi\, r\rho_0\left(g_{\mathrm{total}}(r) - 1\right). \tag{3.26}$$

  If we assume that $g_{\mathrm{total}}(r) = 0$ until the first Gaussian distribution with the average value of the first bond length of $r_{\mathrm{BO}} = 1.37$ Å arises, then $D(r)$ should exhibit a slope of

$$D(r) = 4\pi\rho_0\left(0 - 1\right) = -4\pi\rho_0, \tag{3.27}$$

[3] In PDFgetX manuals and descriptions the cleaned-up scattered intensity $I_{\mathrm{scat}}(q)$ is often called coherent scattered intensity $I_{coh}(q)$. In accordance with the theoretical section of the structure factor and intending no more confusions the designation $I_{\mathrm{scat}}(q)$ stays.

Comparing the number density ρ_0 of the slope from the experimental evaluation with the calculated number density from 3.3, delivers the first evidence of a successful or failed experimental evaluation.

Compton scattering is the most important correction we have to consider in our glass samples. Compton scattering belongs to inelastic scattering, hence a transfer of energy occurs within the target and the wavelength of the incident beam increases $\lambda_{Compton} > \lambda_{inc}$. If these long-wavelength contributions are not correctly removed they result in correspondling long-wavelength abberations to $S_{\mathrm{FZ}}(q)$ that appear in $D(r)$ as peaks in the very low r region below any physically meaningful PDF peaks [4]. One way of correcting the data from Compton scattering is to set the PDF-values to zero up to the region of the first important peak. The inverse Fourier-transformation yields a corrected version of the structure factor $S_{\mathrm{FZ}}(q)'$. The difference between $S_{\mathrm{FZ}}(q)'$ and $S_{\mathrm{FZ}}(q)$ equals to the Compton-scattering contribution.

3.5.1 PDFgetX2 versus PDFgetX3

PDFgetX3 provides only two parameters for adjustment: The parameter b_{g} determines the scaling of the background scattering subtraction:

$$I(q) = I_{\mathrm{M}}(q) - b_{\mathrm{g}} I_{\mathrm{B}}(q). \tag{3.28}$$

The parameter r_{poly} defines the n-th degree of a polynomial function P_n, which optimizes $F(q)$.

$$r_{\mathrm{poly}} = \frac{\pi\, n}{q_{\mathrm{maxinst}}}. \tag{3.29}$$

A maximum signal q_{maxinst} is determined for the correction curve $\Delta F(q)$. The value q_{maxinst} can be adjusted as well, but as equation 3.29 shows, both parameters are correlated with each other. Hence, if n should decrease, one can either adjust r_{poly} or q_{maxinst} to lower values.
Additionally the boundaries q_{min} and q_{max} of $S_{\mathrm{FZ}}(q)$ and $F(q)$ can be truncated influencing the density function $D(r)$. Truncating q_{max} so that the last value of $F(q) \sim 0$, respectively $S_{\mathrm{FZ}}(q) \sim 1$, is advantageous to reduce non-physical artefacts at $D(r)$.

PDFgetX3 has been designed for ease of use, speed and automated operation requiring few input variables. However, for the evaluation of our datasets this highly automated procedure leading to a non-transparency of the program concerning correction and optimization parameters yields to one's fate. In PDFgetX2 one is able to choose different corrections like sample self-absorption, multiple scattering, oblique incidence, fluorescence, X-ray polarization, Laue diffuse scattering and Compton scattering. PDFgetX2 also provides different optimization procedures like $S(q) \to 1$, $F(q) \to 0$ or $G_{\mathrm{low}}(r)$ (smoothing of peaks at unphysical low r-values). The possibility of choosing different "window-functions" that are damping $F(q)$ to zero is also

very valuable. All this information ought to be packed in the parameter r_{poly} at PDFgetX3.
Consequently, in our point of view, the evaluation of vitreous materials by the use of PDFgetX2 is more expedient than the application of the latest software PDFgetX3.

3.5.2 Recommended PDFgetX2 setting

For the evaluation of $x\mathrm{A_2O}$ $(100-x)\mathrm{B_2O_3}$-platelets in transmission geometry measured with synchrotron radiation at Petra III a recommended PDFgetX2 setting is described in this section.
The sample file, $I_{\mathrm{M}}(q)$, and the background file, $I_{\mathrm{B}}(q)$, have to be uploaded. By default the data file format is set to SPEC, which requires an input file.dat ending of the uploaded files and a header information within the file.

```
#### start data
#F D:\Users\katharina\Probenmessungen\PDF_DESY_September_2016\pdfgetx_Auswertungen\2Rb_pdfgetx\zusammengeflickte_Kurve\2Rb_plusBg.dat
#D Don Sep 22 15:50:00 2016
#C
#S 1    CHI file: 2Rb_plusBg.dat
#D
#L q    Intensity
  0.683976297243762        15256.7265692314
  0.704109798162508        15292.6041381146
  0.724243299081254        15299.2770457616
  0.744376800000000        15258.2749025713
  0.764510400000000        15193.7194457544
  0.784643900000000        15166.5207012341
  0.804777400000000        15112.7152485884
```

Figure 3.5: Example of a SPEC-file with a required header information before the columns $I_{\mathrm{M}}(q)$ and q starts. In the case of $2\mathrm{Rb_2}O$ $98\mathrm{B_2O_3}$ examined at Petra III, the 2θ values were converted to q before evaluating the data with PDFgetX2.

- **Experimental configuration**

  For the experimental cofiguration one has to fill in the wavelength λ of the incident beam in Å and the polarization factor P (see figure 3.6).

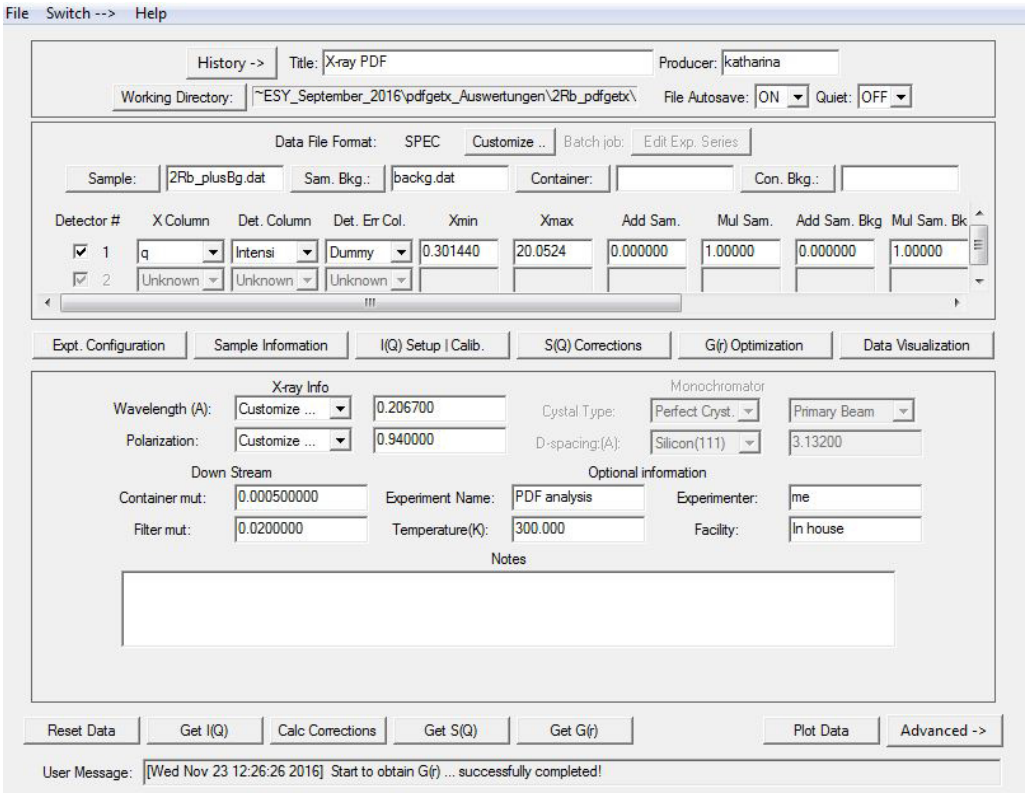

Figure 3.6: The wavelength $\lambda = 0.2057$ Å and the polarization factor $P = 0.94$ of the incident beam at the beamline P02.1 [23].

- **Sample information**

  The "add/remove atoms" button leads to a periodic table from where the atoms occupying the investigated material can be chosen. The specification of the fraction of the atoms is also very important. The attenuation coefficient for glass samples penetrated by a high-energy beam is very low, hence no entry is needed. Filling out the number density of 3.3 could be useful due to an additional plot of the slope $-4\pi\rho_0$ to the density function $D(r)$. The other parameters do not affect the output much and are therefore not quoted.
  The "sample geometry" next to the "add/remove atoms" should be filled in correctly. A wrong specification leads to completely different results.

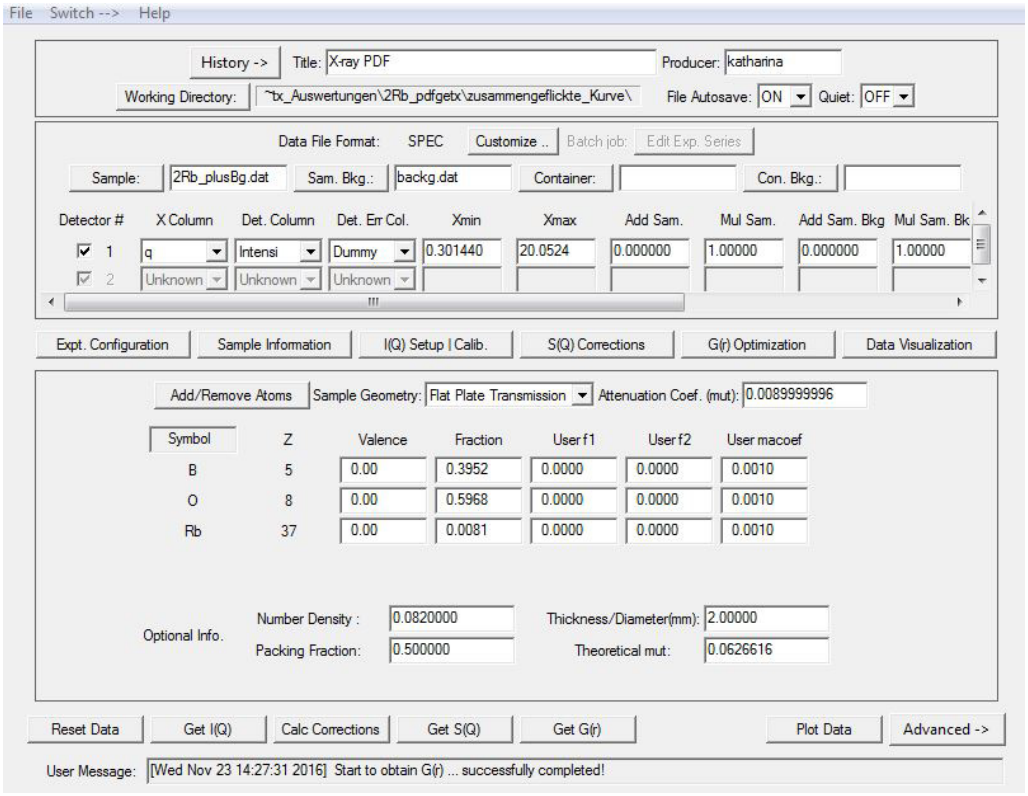

Figure 3.7: $2Rb_2O$ $98B_2O_3$ with its appropriate types of atoms, fractions and number density. The sample geometry was a flat plate in transmission. Filling in the number of valence electrons (ionized atoms, see section 4.1.7) does not affect the output very much.

- **I(q) setup|calibration**

  The only information that is important in this section is the x column format.

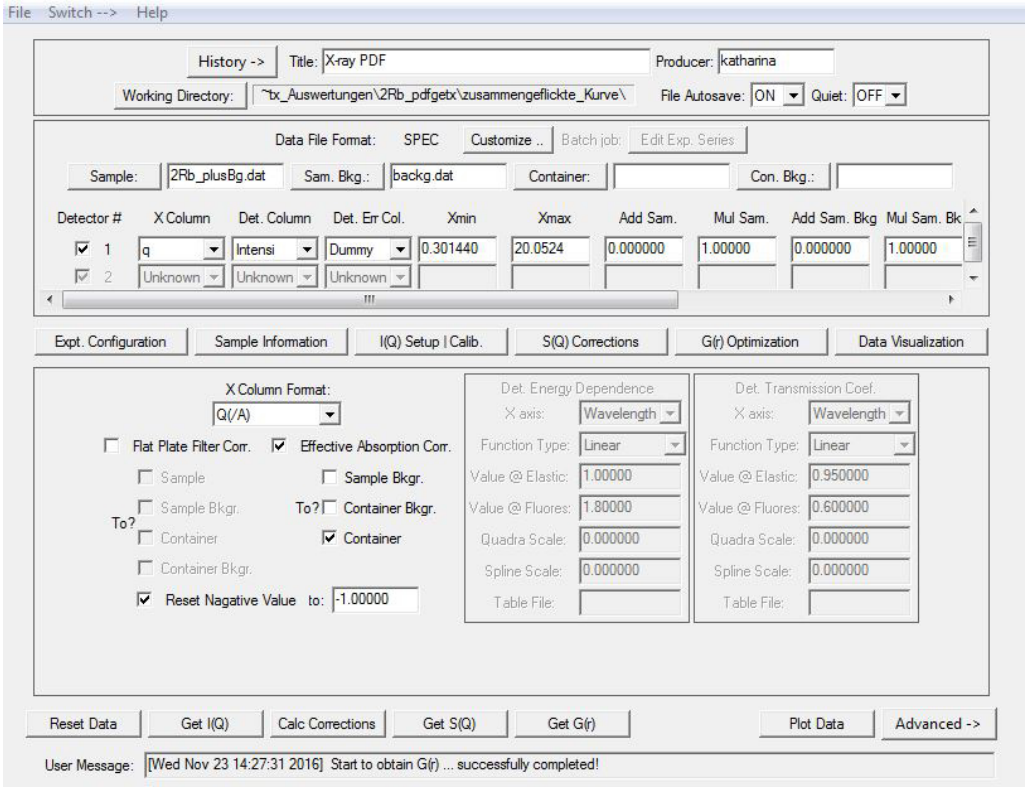

Figure 3.8: The x-column belongs to the scattering vector q in Å.

- **S(q) corrections**

  In this section the most important decisions concerning corrections have to be specified. At the present evaluation Compton scattering shows to have the largest impact on the data. Using one of the profiles (there is almost no difference between the profiles "tabulated data", "empirical form" or the "form of Wentzel", which is explained in details below), a Breit-Dirac factor of 3 and an energy dependency of E is the most efficient specification[4]. The simplest description of the Compton scattering contribution during X-ray measurements is revealed by the physicist Wentzel [24]. He suggested a simple equation for the Compton scattering per atom $C(q)$:

$$C(q) = Z - \sum_i f_{\mathrm{at}}(q), \tag{3.30}$$

[4]If the detector is energy-dependent like an image plate, one should definitely apply the "energy dependency" to the data. In our case we actually had an energy-independent area detector, which means that the detector was counting every arriving photon regardless of its energy. However, if no "energy dependency" was applied the artefacts of the PDF were very large and the peak positions do not coincide with BO(1)= 1.37 Å ,respectively OO(1)= 2.37 Å. Hence, an "energy dependency" of E was chosen and we assume that the detector is not completely counting energy-independently.

where Z is the atomic number and $f_{\text{at}}(q)$ the atomic form factor. For $q = 0$ the Compton scattering $C(q) = 0$, hence no contribution in the forward direction. For $q \to \infty$ the Compton scattering converges to a constant value of Z.

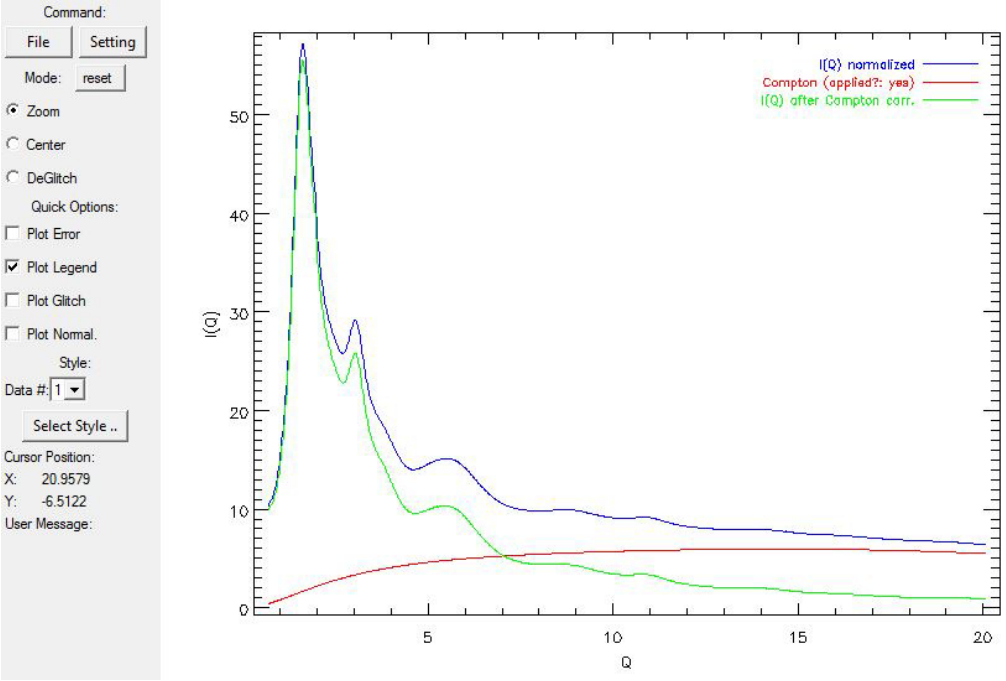

Figure 3.9: The influence of the theoretically calculated Compton scattering to the intensity $I(q)$.

The "Ruland" window is a typical damping function, which means, when applying it to a function $f(x)$, a gradual damping to $f(x) = 0$ for high x-values.
If ticking off the "Ruland" window, the Compton scattering increases to a maximum at low q-values and eventually falls off to zero. Thus, only for low q-values there is a significant Compton-scattering contribution (see figure 3.10).

The "Ruland" window function is only of interest if there is a monochromator between specimen and detector that filters out the wavelengths of the Compton scattering $\lambda_{\text{Compton}} > \lambda_{\text{inc}} + \Delta\lambda$. If the loss of energy during the Compton scattering is very small, λ_{Compton} falls in the interval of $[\lambda_{\text{inc}} - \Delta\lambda, \lambda_{\text{inc}} + \Delta\lambda]$, thus getting through the monochromator and reaching the detector. These λ_{Compton} values belongs to small angles of the inelastic scattered beam, hence to small q-values[20].
There was no monochromator in our experimental setup between specimen and detector, consequently no "Ruland" window-function is needed.

Furthermore it is advisable to tick off the sample self-absorption, the X-ray polarization, the Laue diffusion scattering and the weighting function. The Laue diffusion scattering $var(f_{\text{at}})$ and the weighting function of type $\langle f \rangle^2$ were explained in the theoretical section of the structure factor2.3.1 and are absolutely necessary to apply for receiving the correct *Faber-Ziman* structure factor S_{FZ}. The smoothing of the curves $S_{\text{FZ}}(q)$ and $F(q)$ and the interpolation

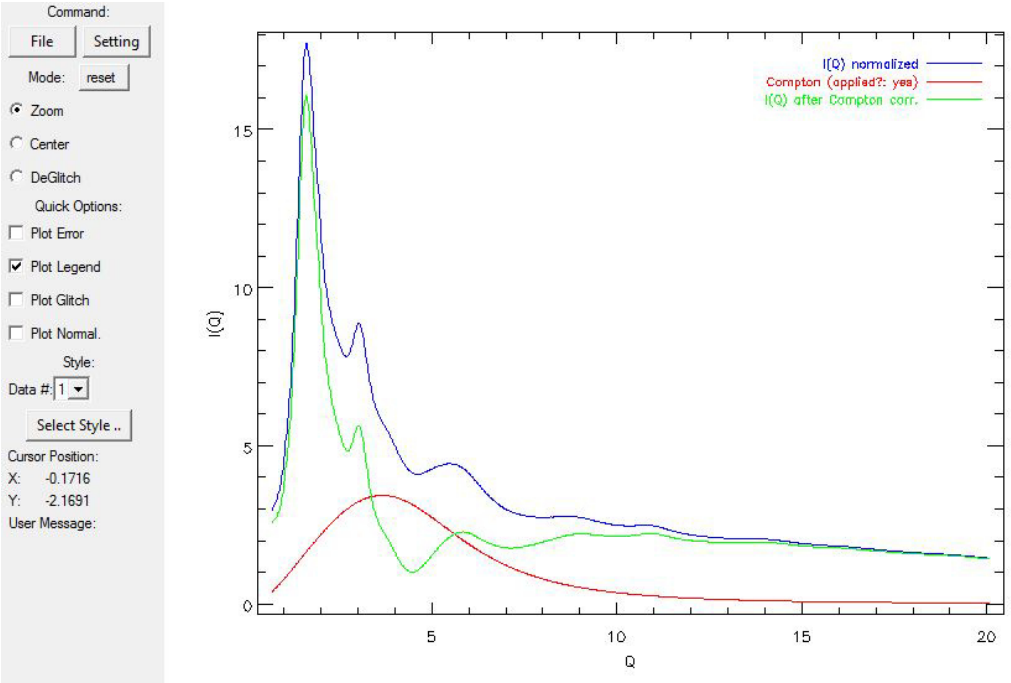

Figure 3.10: The "Ruland" window applied to the Compton scattering.

of $q_{\min}$ to zero are optional.
Also very important concerning the Fourier-transformation $D(r) \propto \mathcal{F}\{F(q)\}$ is the choice of the "window function" for $F(q)$. $F(q)$ could be damped via a Lorch or a Gaussian function. The Gaussian function pushes $D(r)$ down to very unphysical low values. Calculating the coordination numbers would then make no sense at all. Hence, the Lorch-function is a better choice.

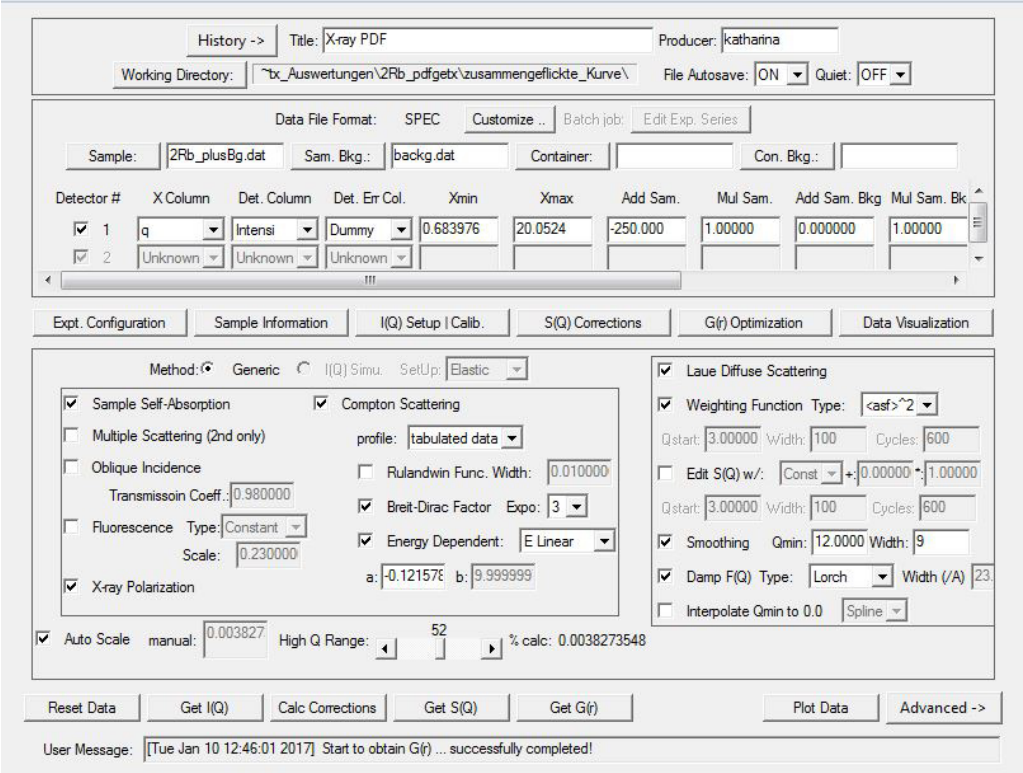

Figure 3.11: The choice of corrections, weighting functions and damping functions for the sample $2Rb_2O\ 98B_2O_3$.

- **G(r) optimization**

  In this section the "function to optimize" is the most relevant input information one has to adjust. Choosing "$S(q) \Leftrightarrow 1.0$" or "$F(q) \Leftrightarrow 0.0$" does not make any difference. It becomes apparent that optimizing the function within the whole measured range of q (in our case: $q_{\min} \sim 0.6$ and $q_{\max}$ could be any value above the measured $q_{\max}$) generates the most adequate density function $D(r)$. If a small $q_{\min}$ is chosen then the function $S(q)$ shows an oscillatory behaviour around $S(q) = 1$ at lower values of q.

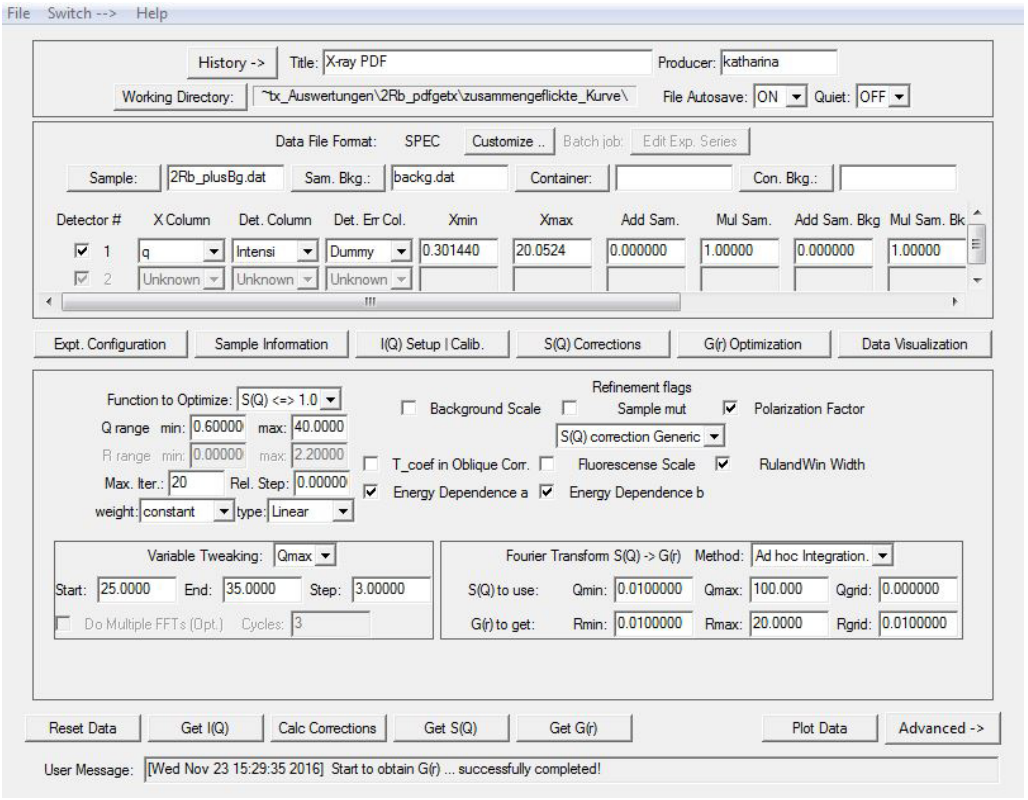

Figure 3.12: The optimization adjustments of the density function $D(r)$

.

Via data visualization, the intensity $I(q)$, the *Faber-Ziman* structure factor $S_{\mathrm{FZ}}(q)$, the reduced structure factor $F(q)$ and the density function $D(r)$ are plotted, see figures 3.13, 3.14, 3.15 and 3.16. The corrections can be plotted as well. After a modification of the setting, the "optimize G(r)" command should be applied, which is subordinated to the "Advanced" button.

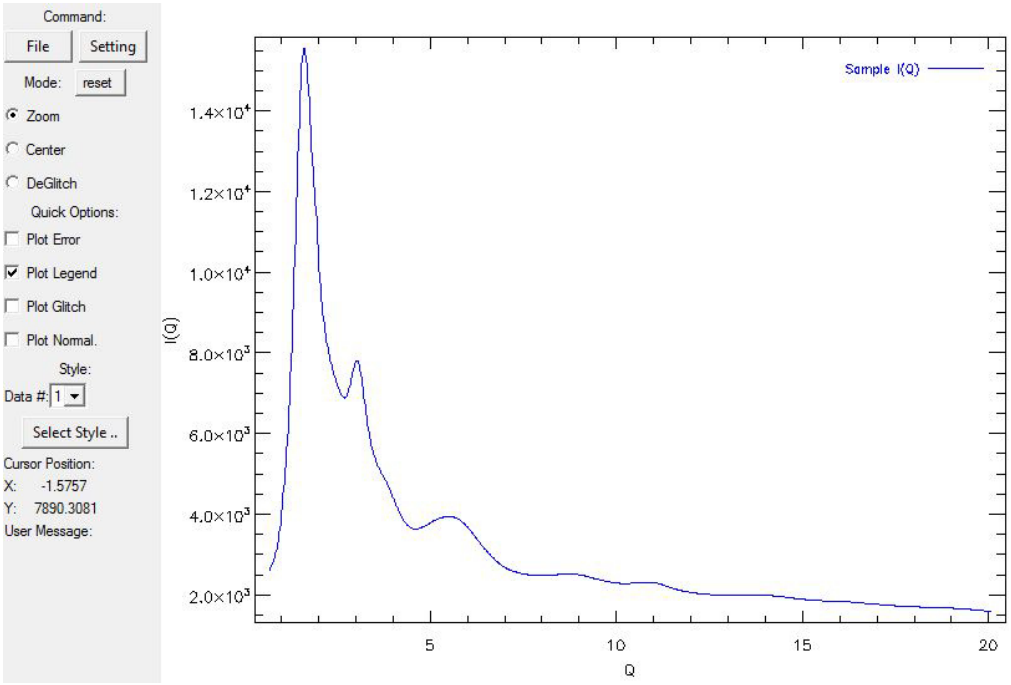

Figure 3.13: The intensity $I(q)$ versus the scattering vector q plotted by the PDFgetX2 program and evaluated for the sample $2Rb_2O\ 98B_2O_3$. The background intensity $I_B(q)$ is subtracted.

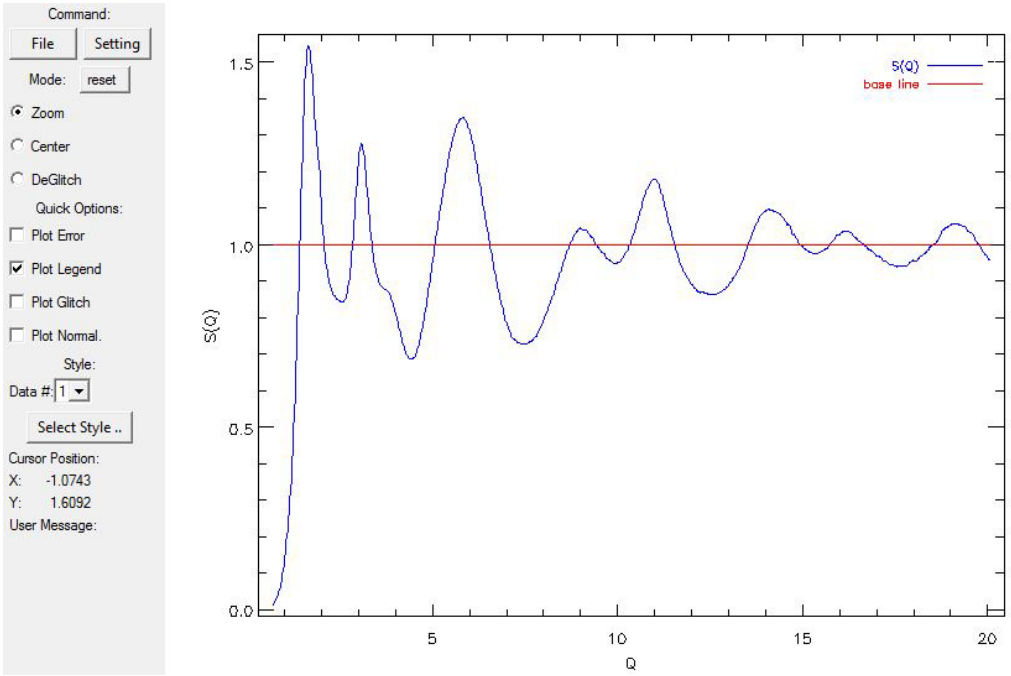

Figure 3.14: The structure factor $S_{FZ}(q)$ versus the scattering vector q plotted by the PDFgetX2 program and evaluated for the sample $2Rb_2O\ 98B_2O_3$. The corrections were applied to $S_{FZ}(q)$.

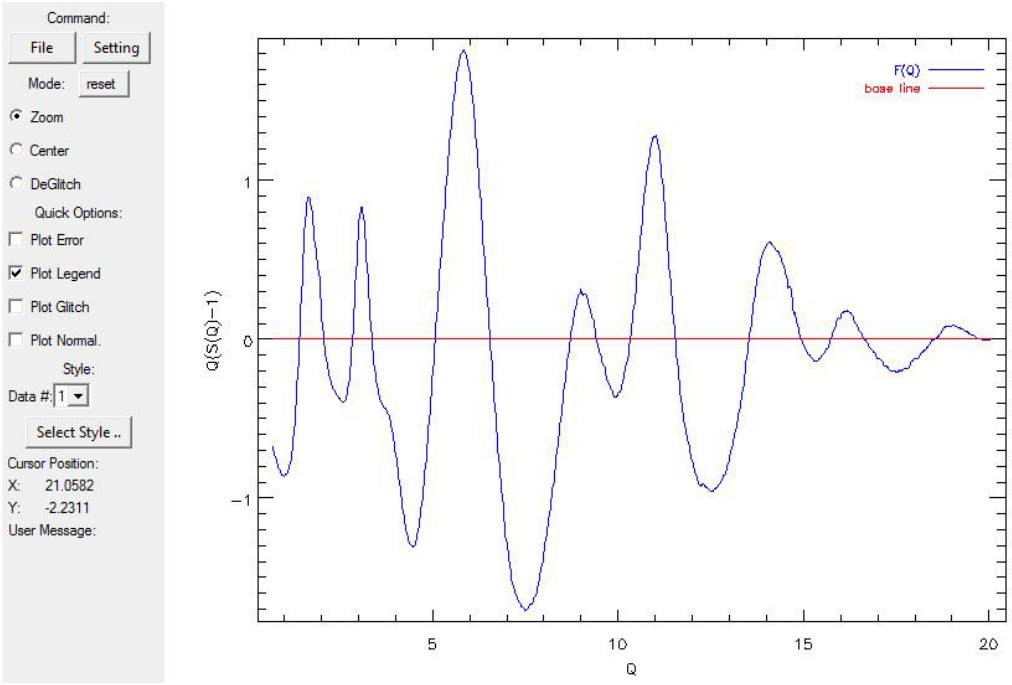

Figure 3.15: The reduced structure factor $F(q)$ versus the scattering vector q plotted by the PDFgetX2 program and evaluated for the sample $2Rb_2O\ 98B_2O_3$. The optimization "$F(q) \Leftrightarrow 0.0$" is applied.

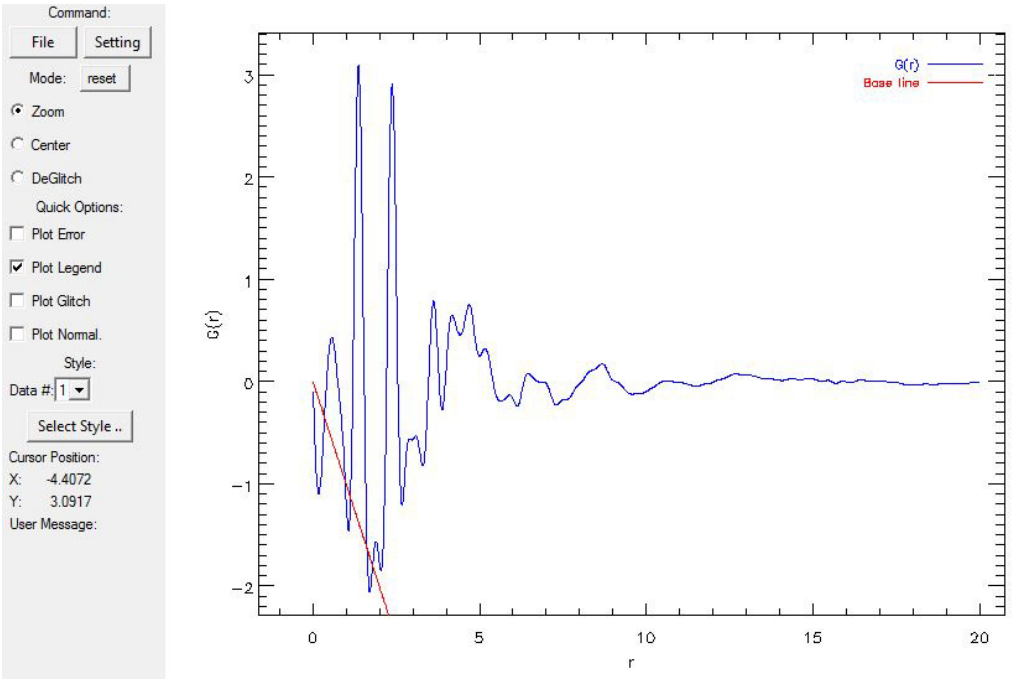

Figure 3.16: The density function $D(r)$ versus the radial distance r plotted by the PDFgetX2 program and evaluated for the sample $2Rb_2O\ 98B_2O_3$. Additionally the slope of $-4\pi\rho_0$ is plotted in red. Mistakenly the program marks the y-axis with $G(r)$, which in literature describes the PDF.

Chapter 4

Results and discussion

4.1 Measurement results with synchrotron radiation

The X-ray diffraction experiments were performed at Petra III in Hamburg (DESY) with $x\mathrm{A_2O}$ $(100-x)\mathrm{B_2O_3}$-bulk samples in transmission geometry utilizing a beam with wavelength of $\lambda = 0.5608$ Å and an area detector[1].

4.1.1 Intensity I(q)

The intensities are plotted with no multiplicative and additive corrections $a(q)$ and $b(q)$ applied, only the background intensity $I_\mathrm{B}(q)$ is subtracted from the measured intensity $I_\mathrm{M}(q)$ (see equation 3.22).
In general, there is a rather small correlation between the intensity yield and the concentration of alkali ions. After closer examination one can find small varying features due to low or high alkali concentration, respectively lighter or heavier alkali incorporations:

- With the increase of the alkali concentration the first peak position around $q \sim 1.6$ Å^{-1} slightly shifts to higher q-values.
- With the increase of the alkali concentration the second peak around $q \sim 3$ Å^{-1} increases with respect to the first peak.
- The third peak around $q \sim 6$ Å^{-1} gradually disappears at heavier alkalis: $15\mathrm{Rb_2O}$ $85\mathrm{B_2O_3}$, $2\mathrm{Cs_2O}$ $98\mathrm{B_2O_3}$, $10\mathrm{Cs_2O}$ $90\mathrm{B_2O_3}$, $15\mathrm{Cs_2O}$ $85\mathrm{B_2O_3}$. For this samples a new small peak is emerging at $q \sim 3.7$ Å^{-1} instead.

The intensities $I(q)$ were normalized by the total scattered intensity.

[1] Fast area detector PerkinElmer XRD1621

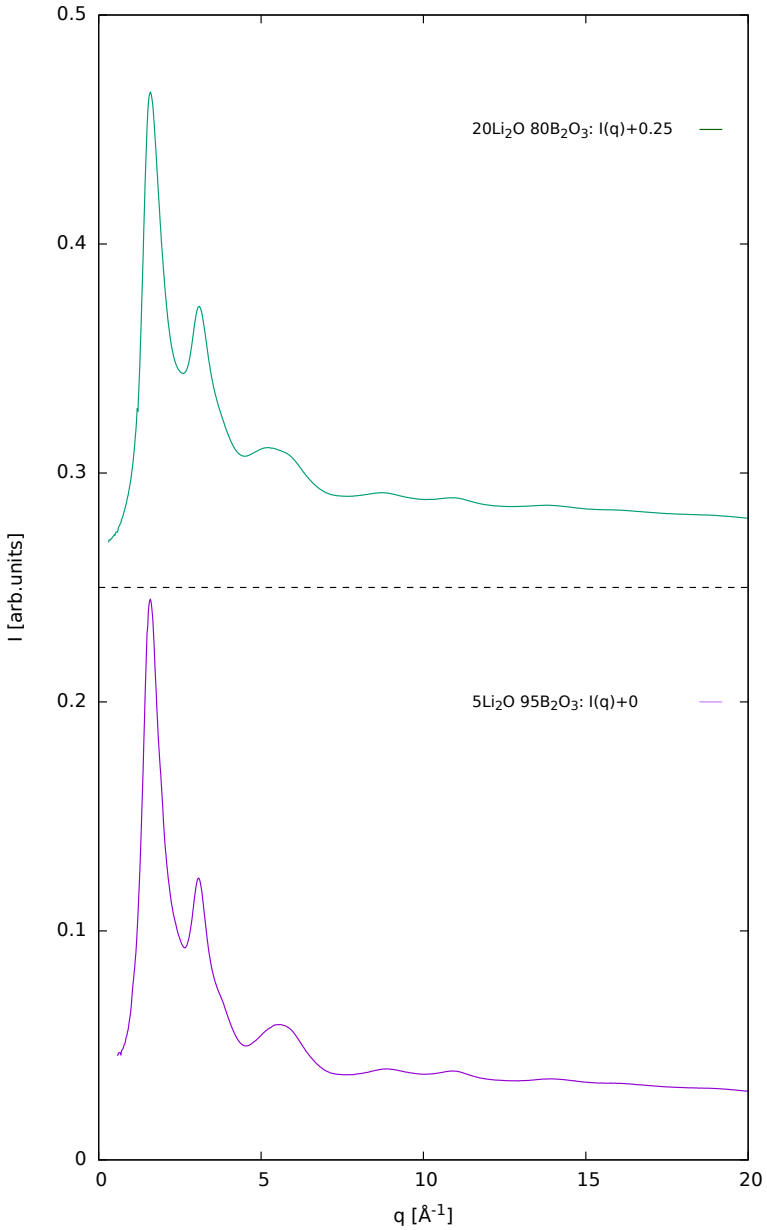

Figure 4.1: The normalized intensity $I(q)$ of $x\mathrm{Li_2O}$ $(100-x)\mathrm{B_2O_3}$. The 20Li-diagram is shifted by 0.25.

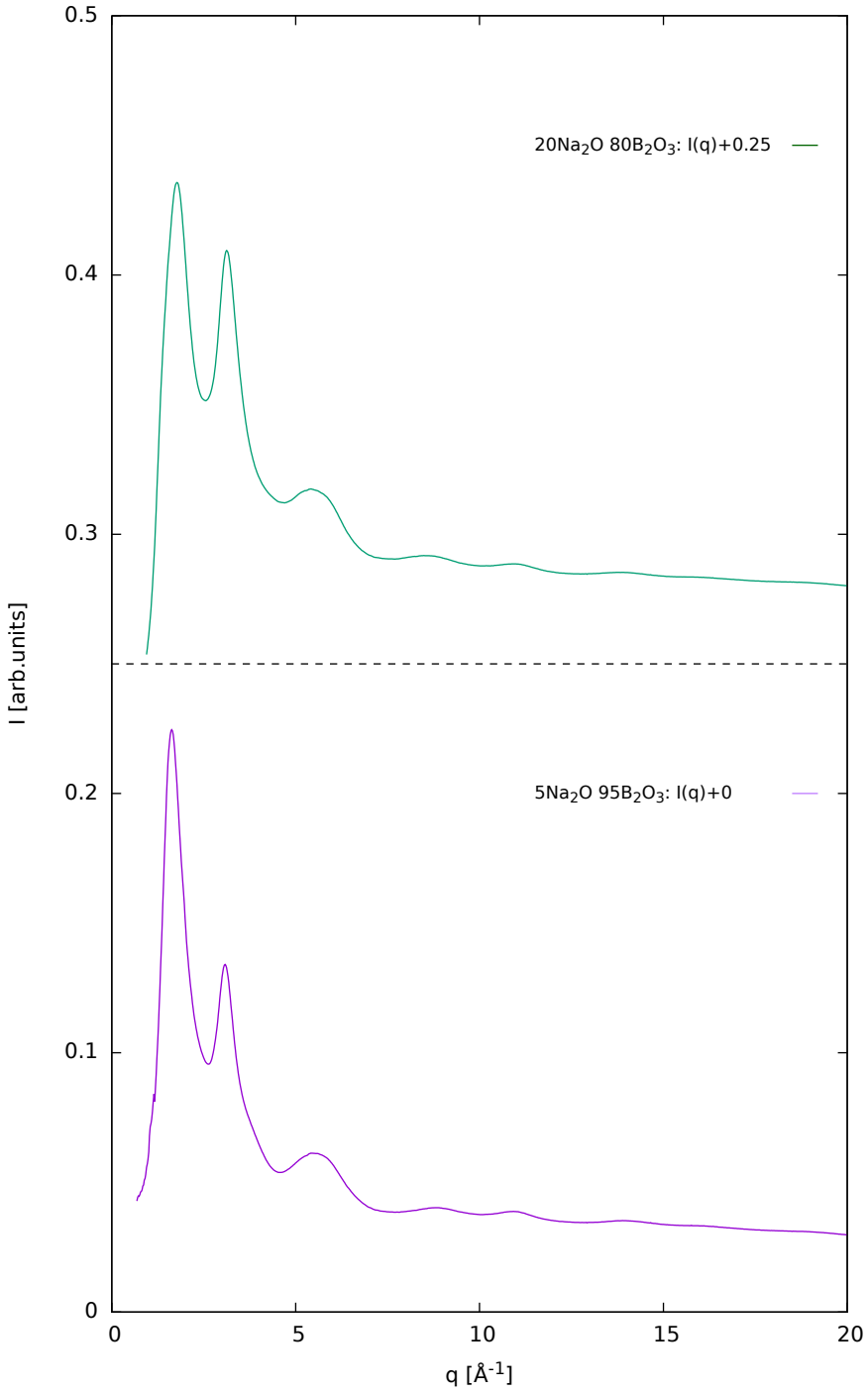

Figure 4.2: The normalized intensity $I(q)$ of $x\mathrm{Na_2O}$ $(100-x)\mathrm{B_2O_3}$. The 20Na-diagram is shifted by 0.25.

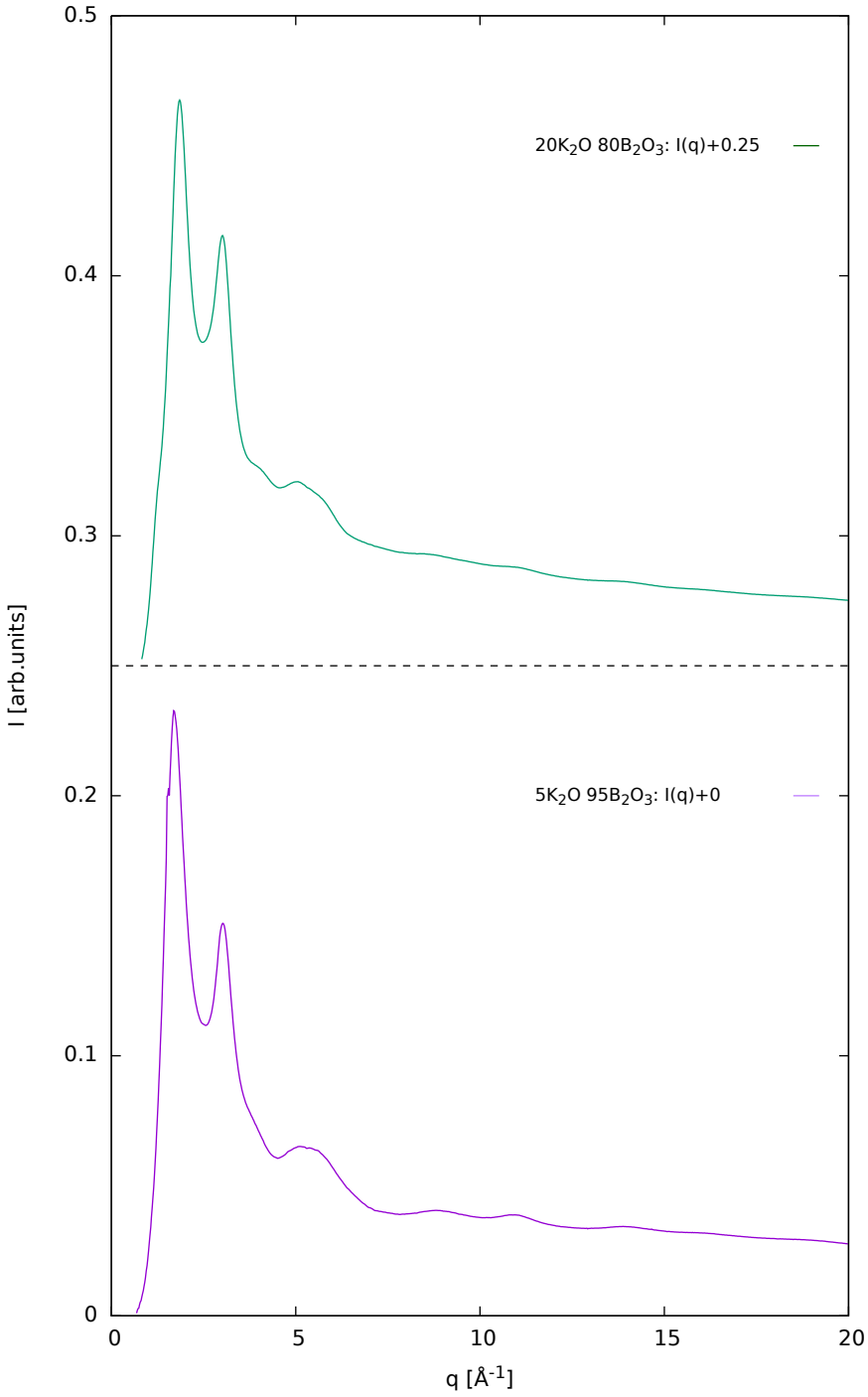

Figure 4.3: The normalized intensity $I(q)$ of $x\mathrm{K_2O}$ $(100-x)\mathrm{B_2O_3}$. The 20K-diagram is shifted by 0.25.

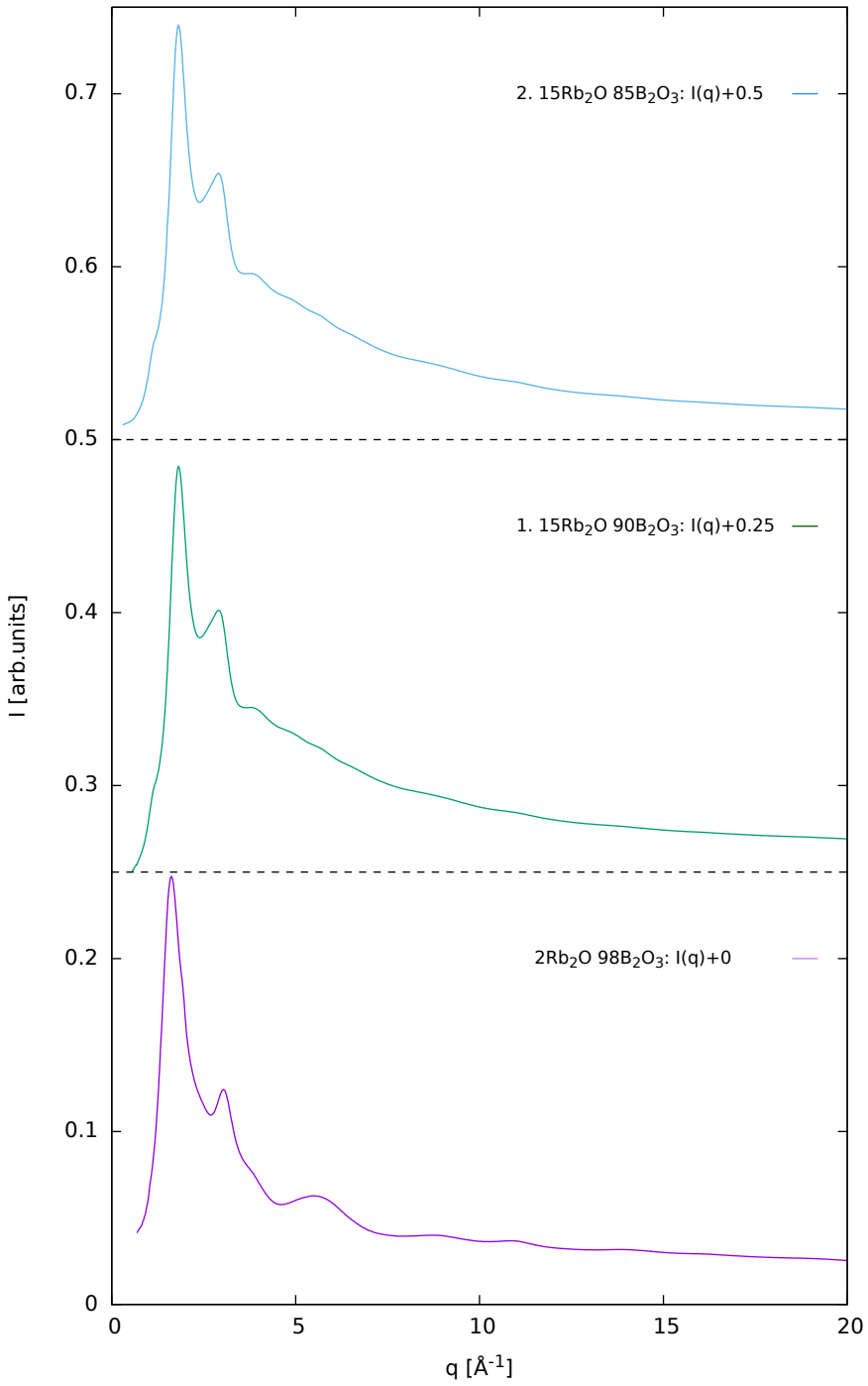

Figure 4.4: The normalized intensity $I(q)$ of $x\mathrm{Rb_2O}$ $(100-x)\mathrm{B_2O_3}$. Two specimen of the concentration $15\mathrm{Rb_2O}$ $85\mathrm{B_2O_3}$ with different thickness were measured: Sample number 1 had a thickness of approximately 238 μm. Sample number 2 had a thickness of approximately 881 μm. The diagrams are shifted by 0.25.

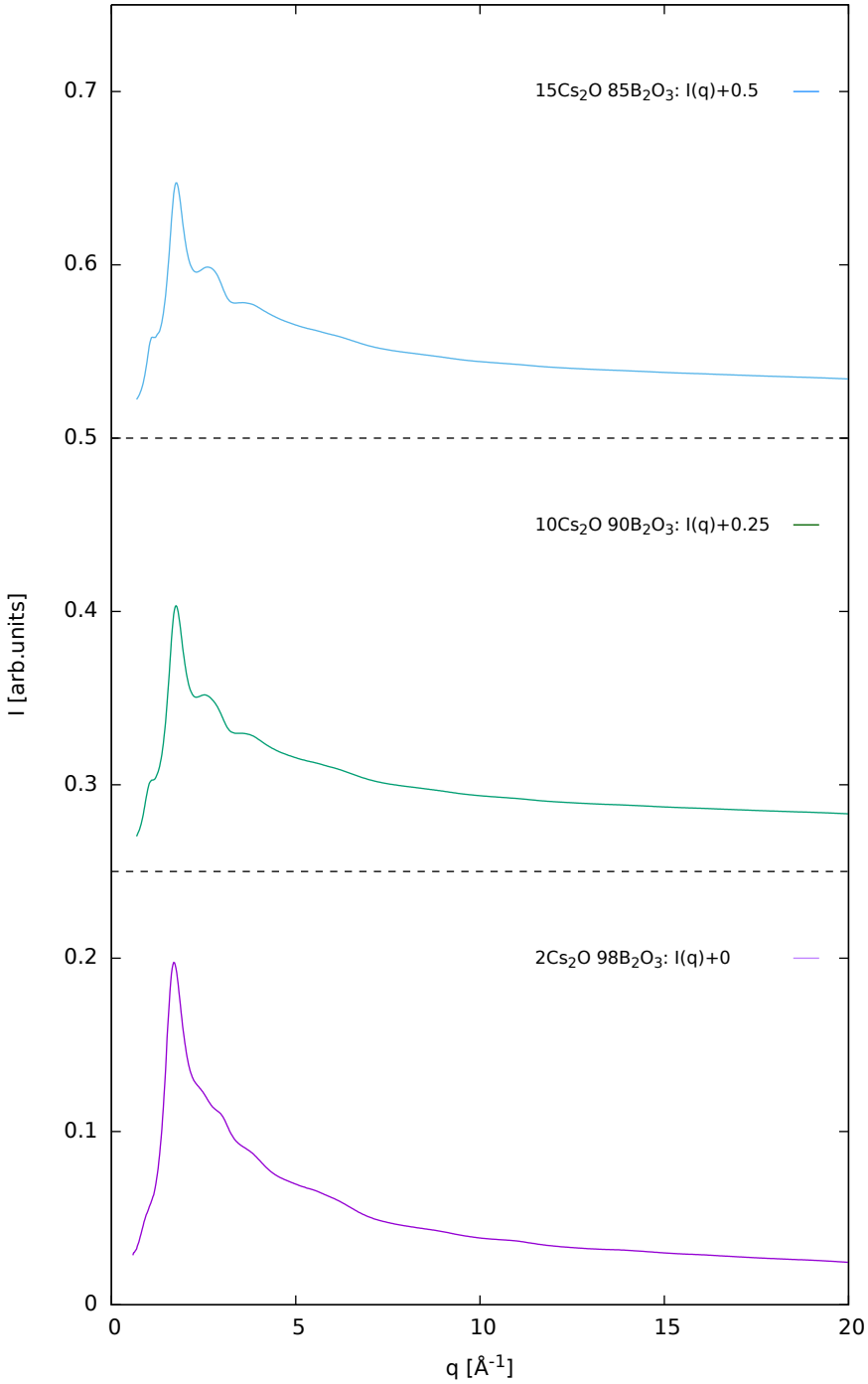

Figure 4.5: The normalized intensity $I(q)$ of $x\mathrm{Cs_2O}$ $(100-x)\mathrm{B_2O_3}$. The diagrams are shifted by 0.25.

4.1.2 Structure factor $S_{FZ}(q)$

The corrections, see chapter 3.5.2, were applied to the *Faber-Ziman* structure factor $S_{\mathrm{FZ}}(q)$.
The curve is oscillating around unity for high q-values as expected. Due to the multiplication by q the reduced structure factor $F(q)$ is emphasizing features at high q-values better than $S_{\mathrm{FZ}}(q)$. Hence, the peak-analysis is performed on the reduced structure factor $F(q)$, see section 4.1.3.

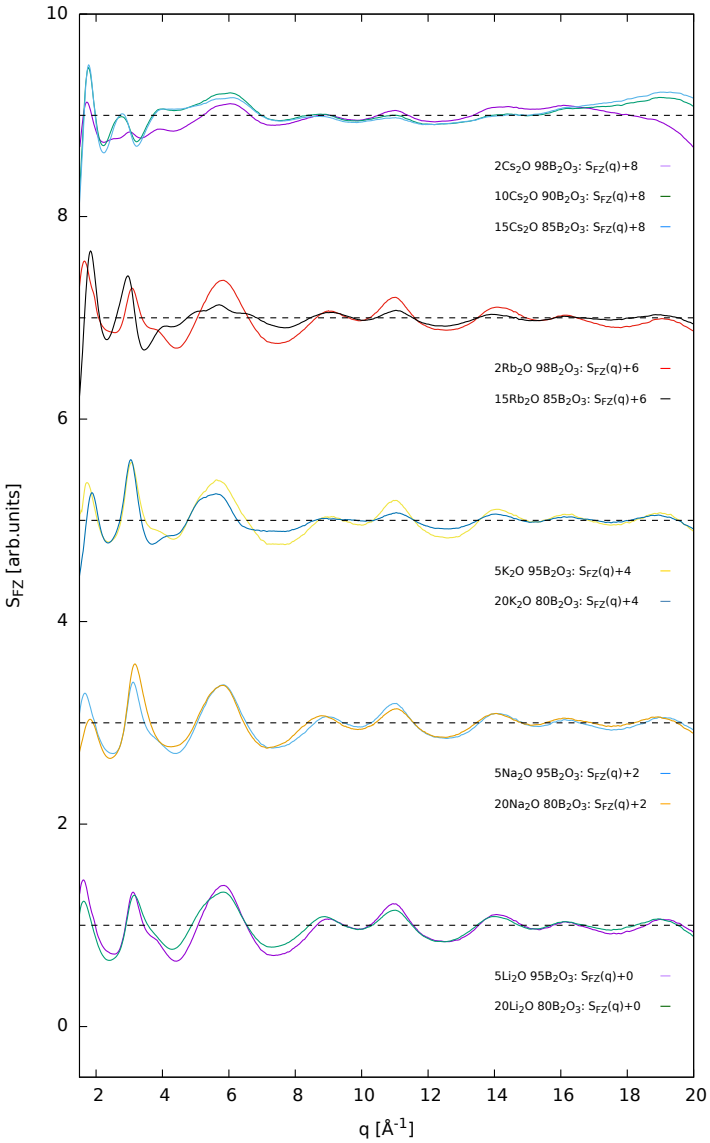

Figure 4.6: The *Faber-Ziman* structure factor $S_{\mathrm{FZ}}(q)$ of the alkali borate glasses $x\mathrm{A_2O}\ (100-x)\mathrm{B_2O_3}$ with A=Li, Na, K, Rb and Cs. The diagrams are shifted by 2.

4.1.3 Reduced structure factor F(q)

To avoid artefacts of the density function $D(r) \propto \mathcal{F}\{F(q)\}$, the reduced structure factor $F(q)$ must be optimized for $F(q_{\max} \to 0)$. The peak-position and peak-height variations are almost identical to the observations, already described in section 4.1.1 for $I(q)$:

- With the increase of the alkali concentration the first peak position around $q \sim 1.6$ Å^{-1} slightly shifts to higher q-values. The first peak height increases for samples with higher alkali concentrations, except for the lighter ions: Li and Na.
- With the increase of the alkali concentration the second peak at $q \sim 3$ Å^{-1} increases.
- Peaks at higher q-values exhibit an inverse trend: The peaks are less distinct for samples with higher alkali admixture. This is particularly noticeable for B_2O_3 samples mixed with heavier ions: K, Rb, Cs.
- It is worth mentioning that a loss of a perfect Gaussian shape for the second and third peak at $q \sim 3$ Å^{-1} and $q \sim 6$ Å^{-1} is observed for high alkali concentrations for heavy alkali samples. A lower alkali concentration causes a shoulder on the right side of the second peak to appear, whereas high alkali concentration causes a shoulder on the left side of the third peak. $15Rb_2O$ $85B_2O_3$ almost loses the Gaussian shape of its third peak and shows ripples instead. $10Cs_2O$ $90B_2O_3$ and $15Cs_2O$ $85B_2O_3$ exhibit a very distinct shoulder on the left side of the third peak around $q \sim 4$ Å^{-1}.

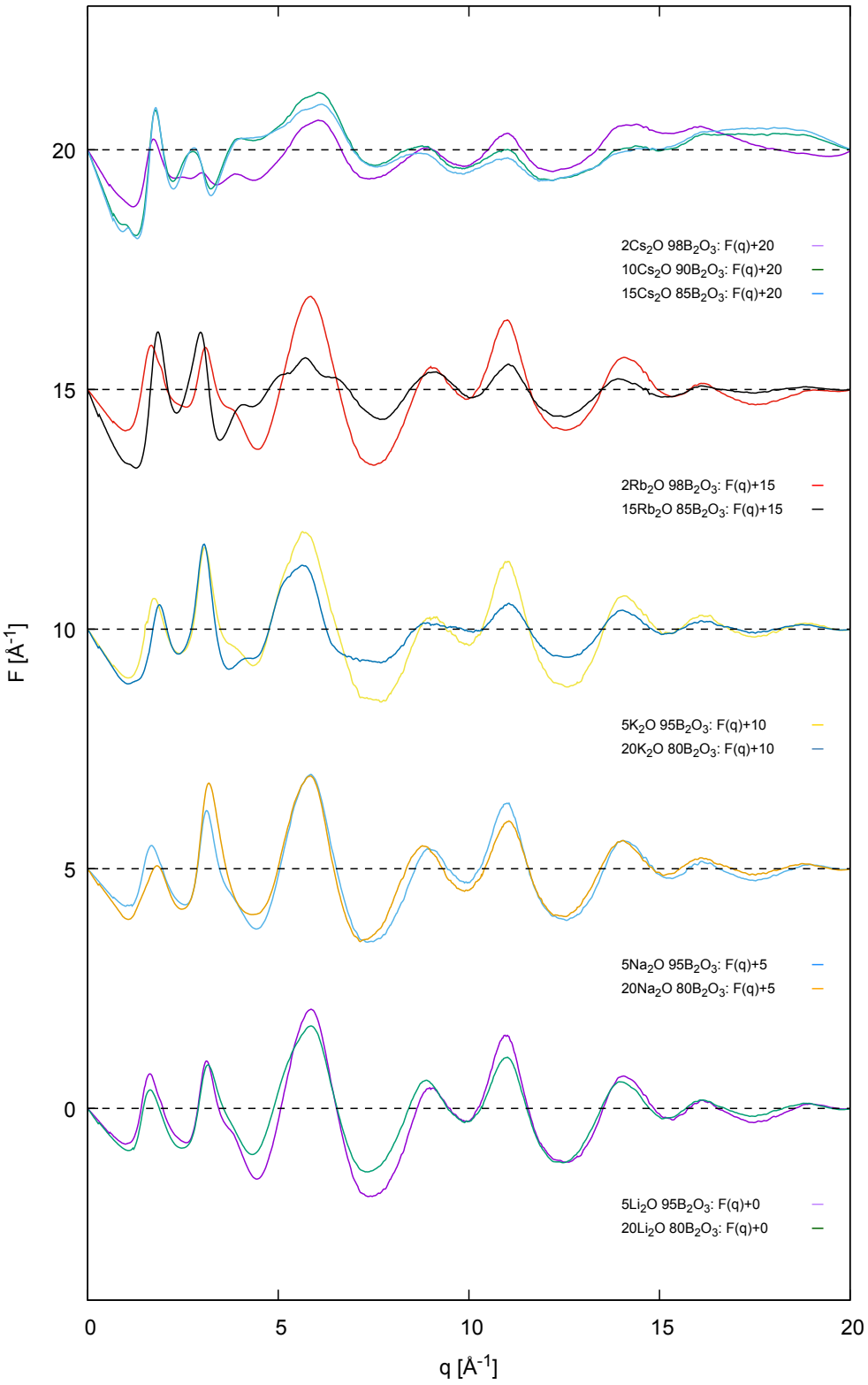

Figure 4.7: The reduced structure factor $F(q)$ of the alkali borate glasses $xA_2O\ (100-x)B_2O_3$ with A=Li, Na, K, Rb and Cs. The diagrams are shifted by 5.

4.1.4 Density function D(r)

There are still some ripples in the area between $r = 0$ Å and the first arising peak at $r \sim 1.37$ Å, which are artefacts with no physical meaning. Ideally this r-range should exhibit a negative slope of $-4\pi\rho_0$ as explained in section 3.5. The ripples are strongly pronounced in the Cs-samples.
Two vertical red lines at $r = 1.37$ Å and $r = 2.37$ Å cross the first and the second peak of all samples, which corresponds to the BO(1) and OO(1) nearest-neighbour distances as discussed in section 1.2.
After closer examination of the $D(r)$-curves one can find more features:

- Samples with higher alkali concentration show a slight shift of the first peak to higher r-values, which indicates an increase of a BO_4 molecule contribution with a larger bond distance BO(1) of 1.47 Å.
- The first and the second peak are smaller in samples with higher alkali concentration.
- The peaks at greater distances also show some slight differences between high and low alkali-concentrated samples: Samples with low alkali concentration show several distinct peaks where those with a high alkali content show only one broad peak. For instance, at a distance of approximately $r = 3$ Å a camel-backed feature is displayed for low alkali-concentrated samples, whereas for high alkali-concentrated samples there is only one peak with a slow falling slope including the distance AO(1) = 3.2 Å (see section 3.1).

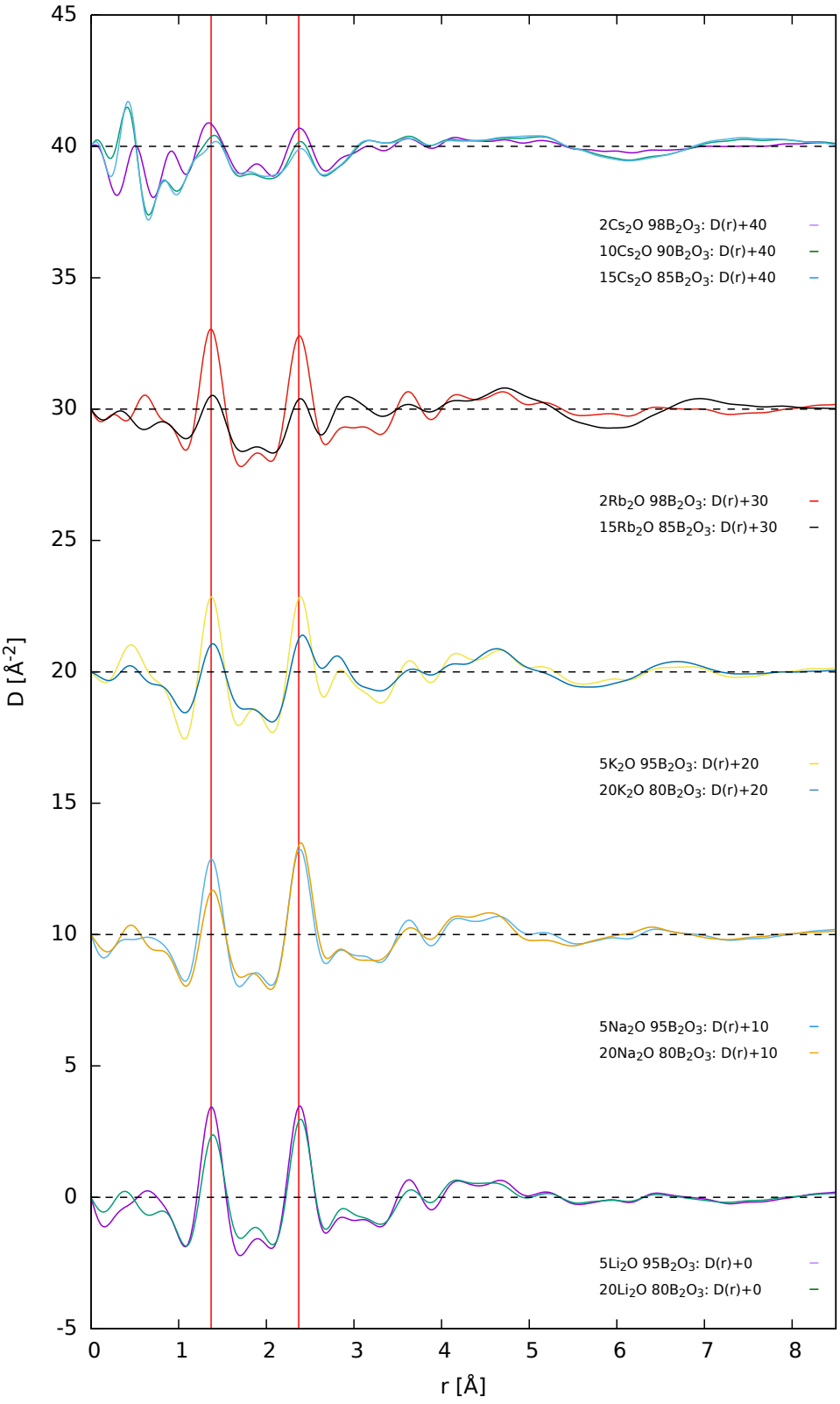

Figure 4.8: The density function $D(r)$ of the alkali borate glasses $x\mathrm{A_2O}\ (100-x)\mathrm{B_2O_3}$ with A=Li,Na,K,Rb and Cs. The two vertical red lines describe the nearest-neighbour distance BO(1) at 1.37 Å and the nearest-neighbour distance OO(1) at 2.37 Å, see table 1.1, respectively table 1.2. The diagrams are shifted by 10.

Table 4.1 shows the peak positions $r_{\max}$ between $r = 0$ Å and $r = 4.5$ Å. The assignment of the peaks to the atomic pairs is sometimes ambiguous: One peak is able to cover two atomic pairs, like BO(3) and AO(1), because the $r_{\max}$ distances of this atomic pairs lie extremely close to each other. Thus, no resolution into two distinct peaks is possible. The observed $r_{\max}$ should then be located in between the $r_{\max}$ distances of BO(3) and AO(1) from literature, see table 1.2.

Samples	BO(1)	OO(1) BB(1)	BO(2)	BO(3) AO(1)	BO(4) AO(2)	OO(2) OO(3)
$5Li_2O$	1.37	2.38	2.87	3.12	3.63	4.18
$20Li_2O$	1.39	2.39	2.88	3.15*	3.65	4.17
$5Na_2O$	1.37	2.38	2.86	3.11	3.63	4.19
$20Na_2O$	1.39	2.39	2.85	-	3.65	4.17
$5K_2O$	1.37	2.39	2.85	3.14*	3.63	4.17
$20K_2O$	1.39	2.41	2.81	3.17**	3.66	4.14
$2Rb_2O$	1.37	2.38	2.89	3.11	3.62	4.17
$15Rb_2O$	1.39	2.39	2.93	3.14**	3.62	4.16
$2Cs_2O$	1.35	2.38	2.89*	3.16	3.62	4.15
$10Cs_2O$	1.41	2.39	-	3.17	3.63	4.09
$15Cs_2O$	1.42	2.40	-	3.16	3.64	4.09

Table 4.1: Nearest-neighbour distances of atomic pairs assigned to peak positions in $D(r)$ in Å.
* A shoulder feature is visible in figure 4.8, instead of a distinct peak.
** A slow falling slope is visible in figure 4.8, instead of a distinct peak.
A hyphen denotes that no features like peaks, shoulders or slow falling slopes are visible at this atomic pair distance.

4.1.5 Total pair distribution function PDF g(r)

The total PDF $g(r)$ is similar to the density function $D(r)$. The only difference is the multiplication of r with $g(r)$, see equation 3.26. Hence, no further information could be extracted from the total PDF and the reader is referred to the previous section 4.1.4.

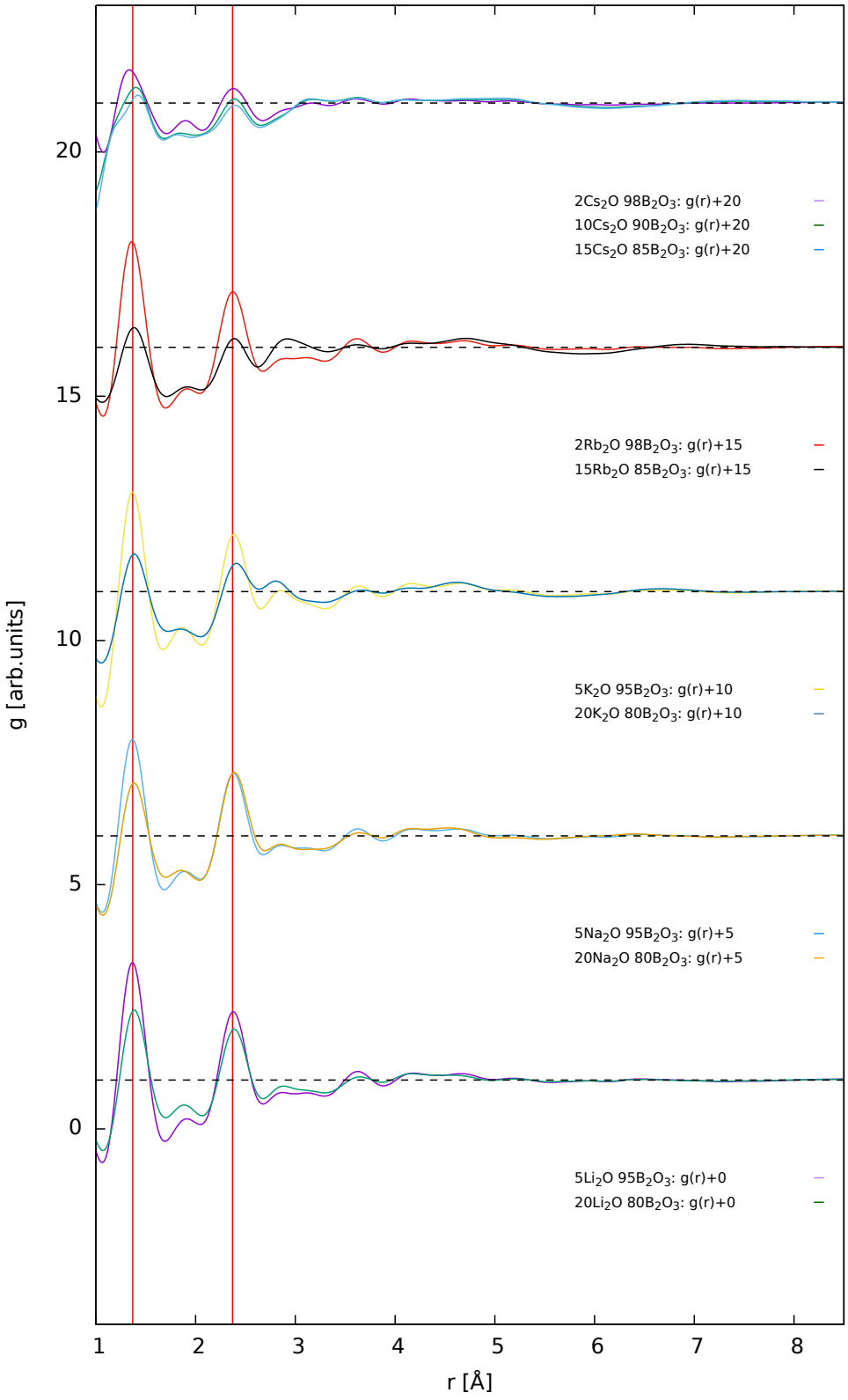

Figure 4.9: The total PDF $g(r)$ of the alkali borate glasses $x\mathrm{A_2O}\ (100-x)\mathrm{B_2O_3}$ with A=Li, Na, K, Rb and Cs. The two vertical red lines describe the nearest-neighbour distance BO(1) at 1.37 Å and the nearest-neighbour distance OO(1) at 2.37 Å, see table 1.1, respectively table 1.2. The diagrams are shifted by 5.

4.1.6 Radial distribution function RDF(r)

The RDF is another representation of the distribution of interatomic distances $r_{\max}$. An additional plot of the number density $4\pi\rho_0 r^2$ in dashed lines is also shown. For $r \to \infty$ the RDF approaches $4\pi\rho_0 r^2$.

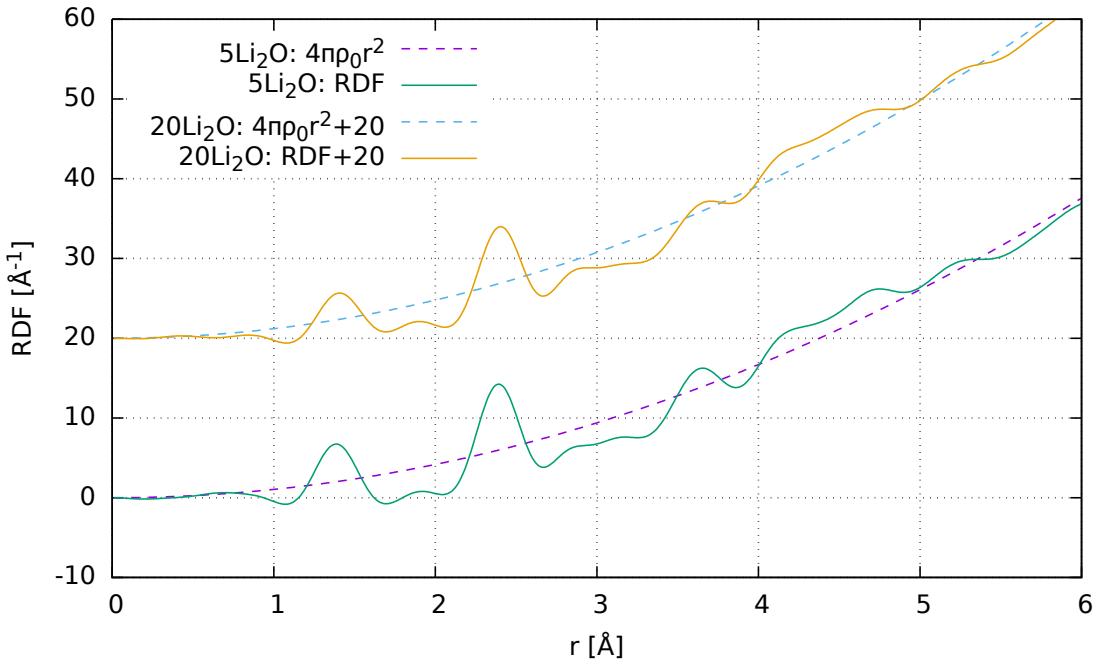

Figure 4.10: The RDF of $x\mathrm{Li_2O}$ $(100-x)\mathrm{B_2O_3}$ plotted with the corresponding number density ρ_0 multiplied with $4\pi r^2$. The 20Li-diagram is shifted by 20.

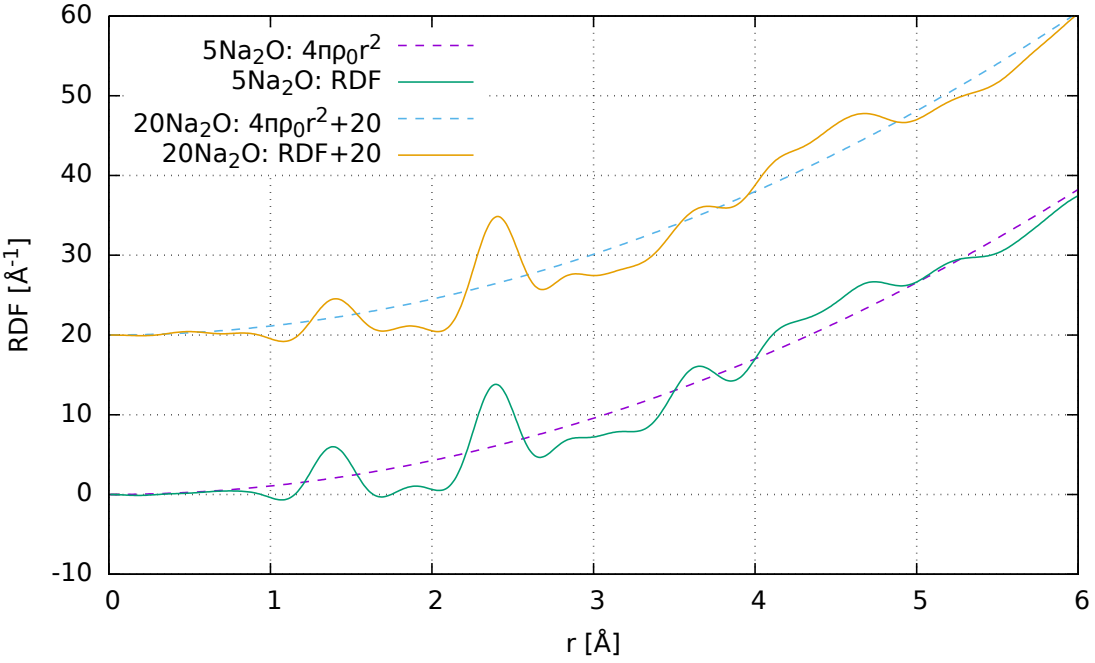

Figure 4.11: The RDF of $x\mathrm{Na_2O}$ $(100-x)\mathrm{B_2O_3}$ plotted with the corresponding number density ρ_0 multiplied with $4\pi r^2$. The 20Na-diagram is shifted by 20.

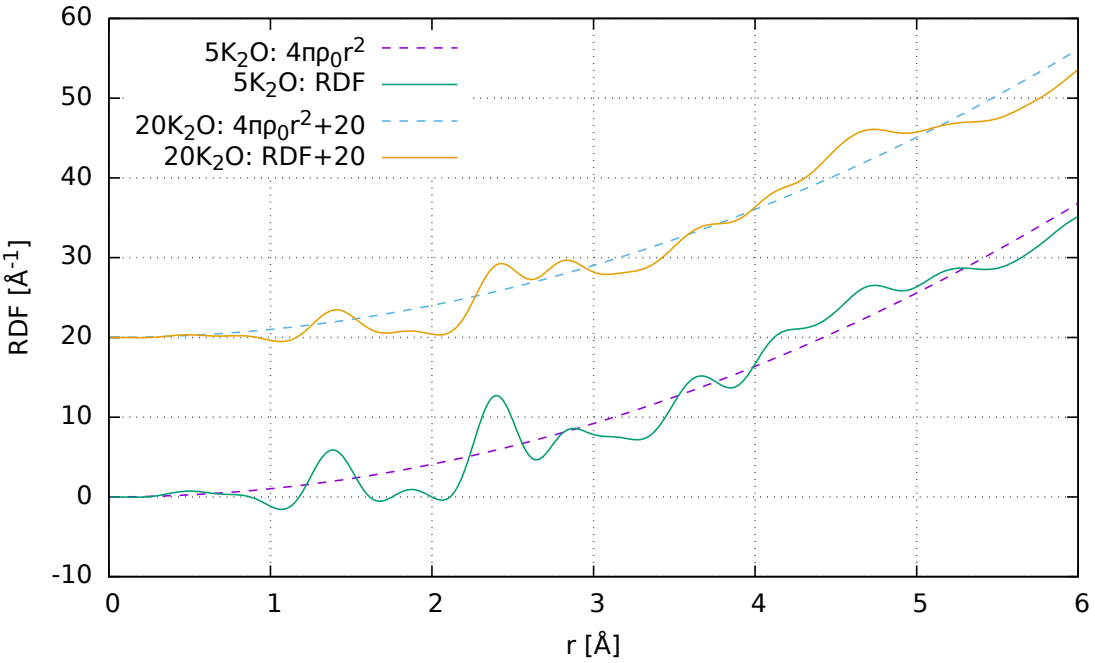

Figure 4.12: The RDF of $x\mathrm{K_2O}$ $(100-x)\mathrm{B_2O_3}$ plotted with the corresponding number density ρ_0 multiplied with $4\pi r^2$. The 20K-diagram is shifted by 20.

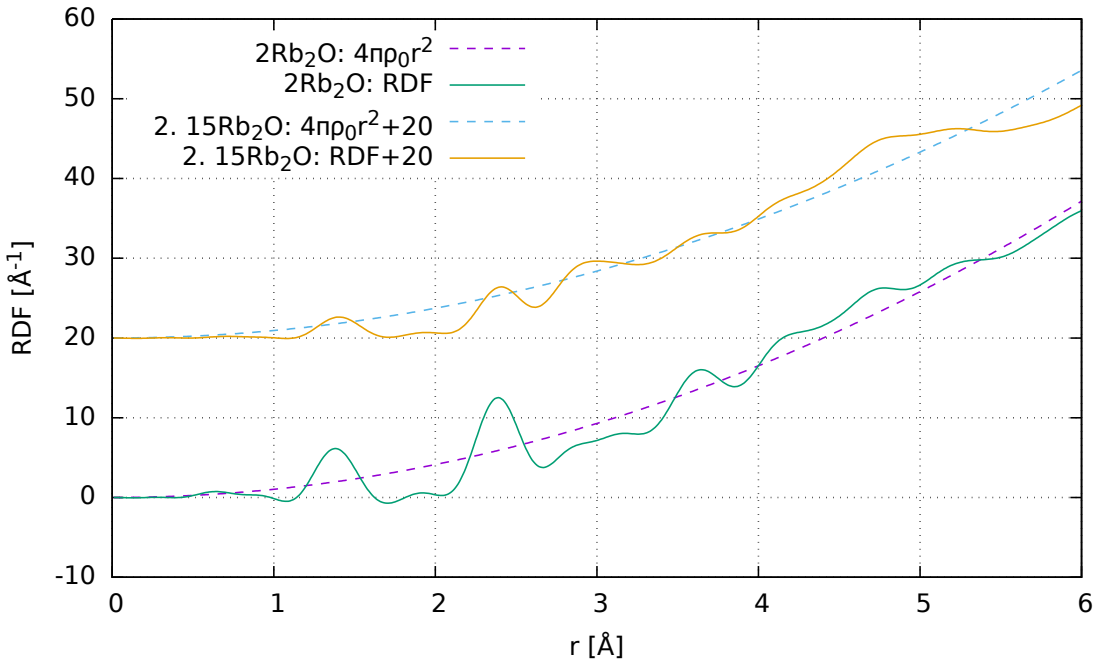

Figure 4.13: The RDF of $x\mathrm{Rb_2O}$ $(100-x)\mathrm{B_2O_3}$ plotted with the corresponding number density ρ_0 multiplied with $4\pi r^2$. The 15Rb-diagram is shifted by 20.

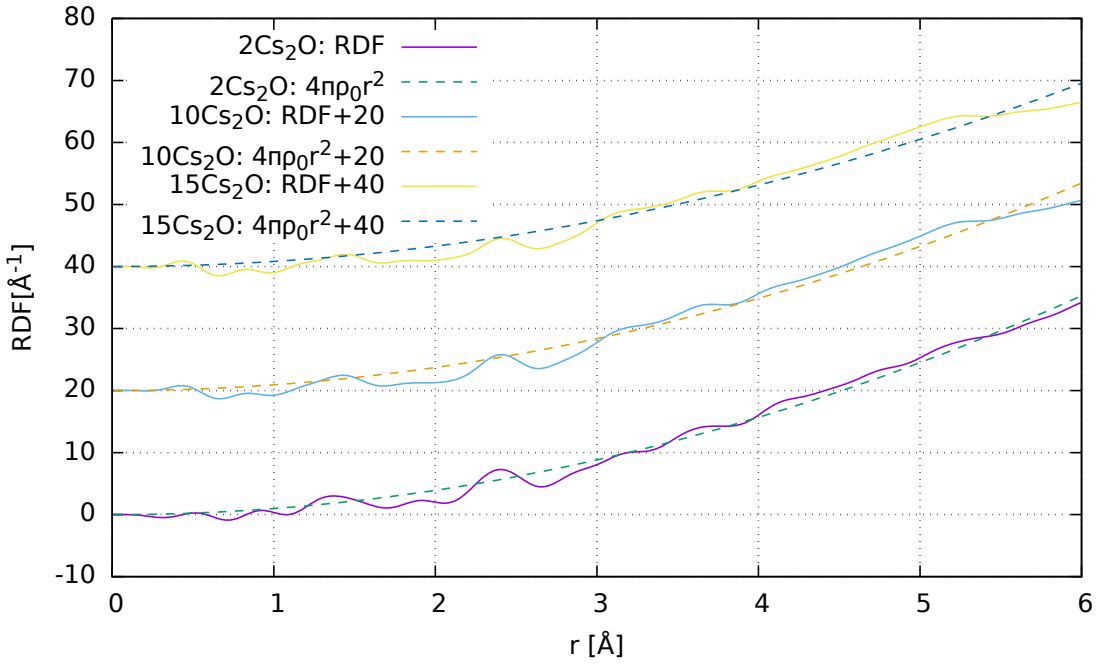

Figure 4.14: The RDF of $x\mathrm{Cs_2O}$ $(100-x)\mathrm{B_2O_3}$ plotted with the corresponding number density ρ_0 multiplied with $4\pi r^2$. The diagrams are shifted by 20.

4.1.7 Coordination number $\bar{n}$

The coordination number $\bar{n}_{\mathrm{B}}^{\mathrm{O}}$, respectively $\bar{n}_{\mathrm{O}}^{\mathrm{B}}$ of the nearest neighbours BO(1) were calculated, which refer to the integral of the first peak of $g(r)$ at $r \sim 1.37$ Å multiplied with r^2 and a prefactor that depends on the concentrations c_{B} and c_{O}, and the approximated atomic form factor $f_{\mathrm{at}}(q)_\alpha \sim Z_\alpha$ with α =A, B and O (see 2.92 and 2.93).
The atoms in the structure are assumed to be ionized, hence there exists an ionic charge z_α for every atom A, B and O (see [28]). The ionic charge z_α should be subtracted from the atomic number Z_α:

$$f_{\mathrm{at}}(q)_\alpha \sim Z_\alpha - z_\alpha. \tag{4.1}$$

An overall charge neutrality has to be guaranteed:

$$N_{\mathrm{B}} z_{\mathrm{B}} + N_{\mathrm{O}} z_{\mathrm{O}} + N_{\mathrm{A}} z_{\mathrm{A}} = 0. \tag{4.2}$$

For a pure B_2O_3 structure, where $N_{\mathrm{A}} = 0$, equation 4.2 yields an ionic charge of $z_{\mathrm{B}} = +2$ and $z_{\mathrm{O}} = -\frac{4}{3}$.
For a $x\mathrm{A_2O}$ $(100-x)\mathrm{B_2O_3}$ structure an ionic charge of $z_{\mathrm{A}} = +1$ is assumed. This implies that half of the charge, supplied by the alkali atoms, is distributed over all B atoms and the other half is distributed over all O atoms to guarantee 4.2:

$$z_{\mathrm{B}} = 2 - \frac{1}{6}\frac{N_{\mathrm{A}}}{N_{\mathrm{B}}} \tag{4.3}$$

$$z_{\mathrm{O}} = -\frac{4}{3} - \frac{1}{6}\frac{N_{\mathrm{A}}}{N_{\mathrm{O}}}. \tag{4.4}$$

stoichiometry	z_{O}	z_{B}	z_{A}
$2\mathrm{A_2O}$ $98\mathrm{B_2O_3}$	-1.336	1.997	1
$5\mathrm{A_2O}$ $95\mathrm{B_2O_3}$	-1.339	1.991	1
$10\mathrm{A_2O}$ $90\mathrm{B_2O_3}$	-1.345	1.981	1
$15\mathrm{A_2O}$ $85\mathrm{B_2O_3}$	-1.352	1.971	1
$20\mathrm{A_2O}$ $85\mathrm{B_2O_3}$	-1.359	1.958	1

Table 4.2: Ionic charges z_{O},z_{B},z_{A} of the atoms O, B and A=Li, Na, K, Rb, Cs calculated for different stoichiometries.

The results for the square of the expectation value of the approximated atomic form factor 4.1 and the coordination number $\bar{n}_{\mathrm{B}}^{\mathrm{O}}$, respectively $\bar{n}_{\mathrm{O}}^{\mathrm{B}}$, of the nearest neighbours BO(1) are given below.
The theory given in 1.3 and also the shift of the first peak towards higher r-values, visible in figure 4.8, predicts an increase of BO_4 content in the structure while increasing the alkali concentration up to 30 %, which should raise the coordination number $\bar{n}_{\mathrm{B}}^{\mathrm{O}}$ from 3 to 4. This is not reproduced by the present data (see table 4.3). One interpretation is that beside of the formation of BO_4 tetrahedrons there is also

samples	$\langle Z_\alpha - z_\alpha \rangle^2$	$\bar{n}_{\mathrm{B}}^{\mathrm{O}}$	$\bar{n}_{\mathrm{O}}^{\mathrm{B}}$
$5Li_2O\ 95B_2O_3$	45.36	3.67	2.40
$20Li_2O\ 80B_2O_3$	42.53	3.63	2.23
$5Na_2O\ 95B_2O_3$	47.58	3.42	2.24
$20Na_2O\ 80B_2O_3$	52.09	3.45	2.12
$5K_2O\ 95B_2O_3$	49.86	3.37	2.21
$20K_2O\ 80B_2O_3$	62.62	3.40	2.09
$2Rb_2O\ 98B_2O_3$	49.68	3.69	2.44
$15Rb_2O\ 85B_2O_3$	76.84	2.87	1.81
$2Cs_2O\ 98B_2O_3$	51.75	2.75	1.82
$10Cs_2O\ 90B_2O_3$	78.03	3.22	2.07
$15Cs_2O\ 85B_2O_3$	98.31	3.06	1.93

Table 4.3: The square of the expectation value of the approximated atomic form factor and the coordination numbers $\bar{n}_{\mathrm{B}}^{\mathrm{O}}$ and $\bar{n}_{\mathrm{O}}^{\mathrm{B}}$ of the nearest neighbours BO(1).

an increase of BO_2 molecules when raising the alkali concentration, which does not change the average of nearest neighbours $\bar{n}_{\mathrm{B}}^{\mathrm{O}}$.
However, one can notice a correlation between type of ion and coordination number: Heavier ions have smaller coordination numbers. This is valid for a low concentration as well as for a high concentration of alkali atoms. Only the Rb-samples are following a different trend as visible in figure 4.15 and 4.16. The explanation for this tendency, which is strongly supported by literature [28], [2], is that bigger ions do not favour to reside next to a bridging oxygen, simply due to their size and as a result they are not as efficient as lighter alkalis like lithium in supporting the formation of BO_4 molecules.

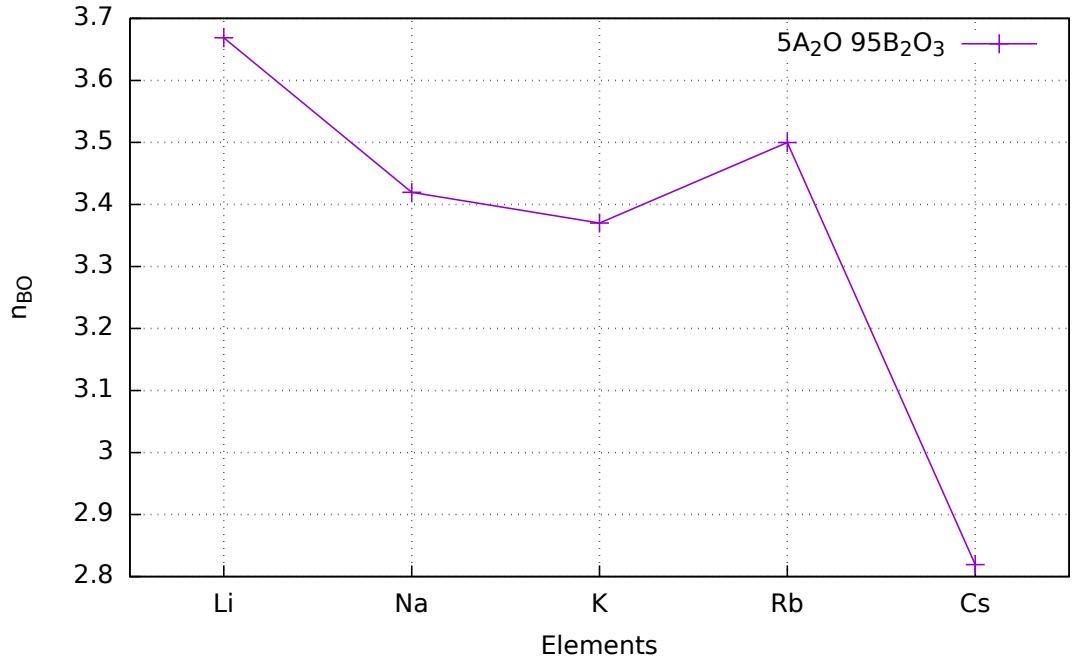

Figure 4.15: The coordination number $\bar{n}_{\mathrm{B}}^{\mathrm{O}}$ with respect to the elements for the samples with low alkali concentration. The values for Rb and Cs were extrapolated.

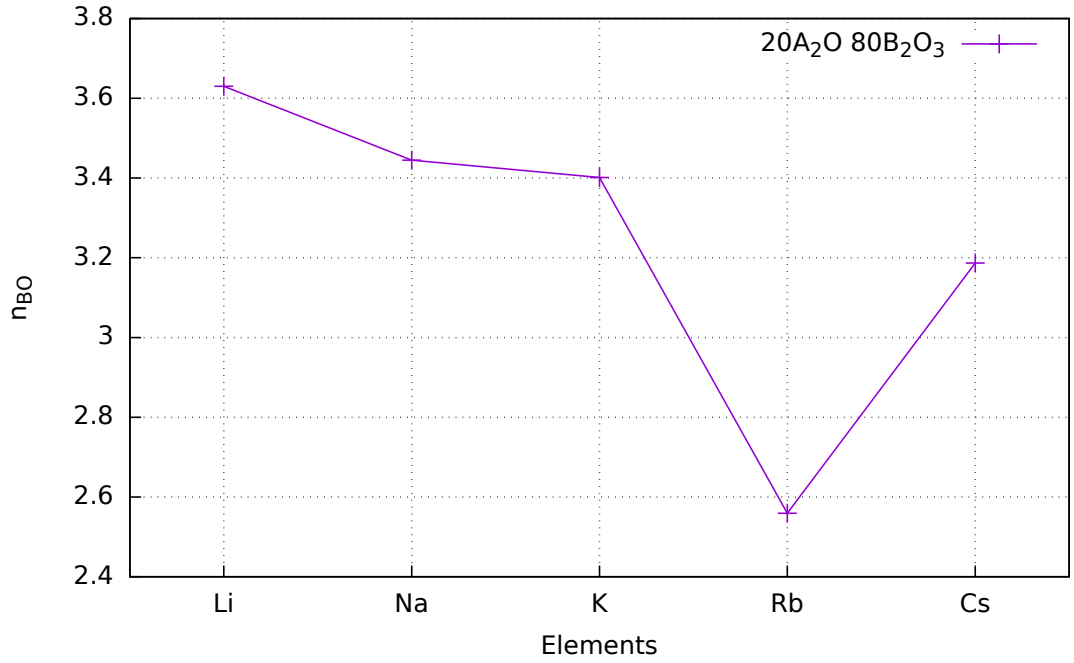

Figure 4.16: The coordination number $\bar{n}_{\mathrm{B}}^{\mathrm{O}}$ with respect to the elements for the samples with high alkali concentration. The values for Rb and Cs were extrapolated.

4.2 Measurement results with Ag-anode

In addition to the measurements with synchrotron radiation in the previous chapter, experiments on laboratory machines were performed. These experiments were done at an Empyrean PANalytical X-ray diffractometer at the TU Wien using X-rays with a wavelength of $\lambda = 0.5608$ Å from an Ag-Anode and a scintillator point detector. The samples were prepared as powder in soda-lime glass capillaries[2] with 1 mm diameter. The first measurement series were accomplished on March/May 2016.

4.2.1 Intensity I(q)

Due to the different natures of the sources the total scattered intensity at the synchrotron was much higher compared to the lab source, although the exposure time was only seconds compared to 24 h measurements and thus giving a much better signal-to-noise ratio.
Features that change with the alkali concentration are almost the same like in section 4.1.1:

- With the increase of the alkali concentration the first peak slightly shifts to higher q-values.
- The third peak of high alkali-concentrated samples gradually disappears. This is valid for heavier ions: K, Rb and Cs.

The intensities $I(q)$ are normalized by the total scattered intensity.
The $20Li_2O\ 80B_2O_3$ sample displays an additional feature in the shape of a spike at approximately $q = 1.95$ Å^{-1}, which indicates the onset of a crystallization process.

[2]Type: AR, I860, PH360

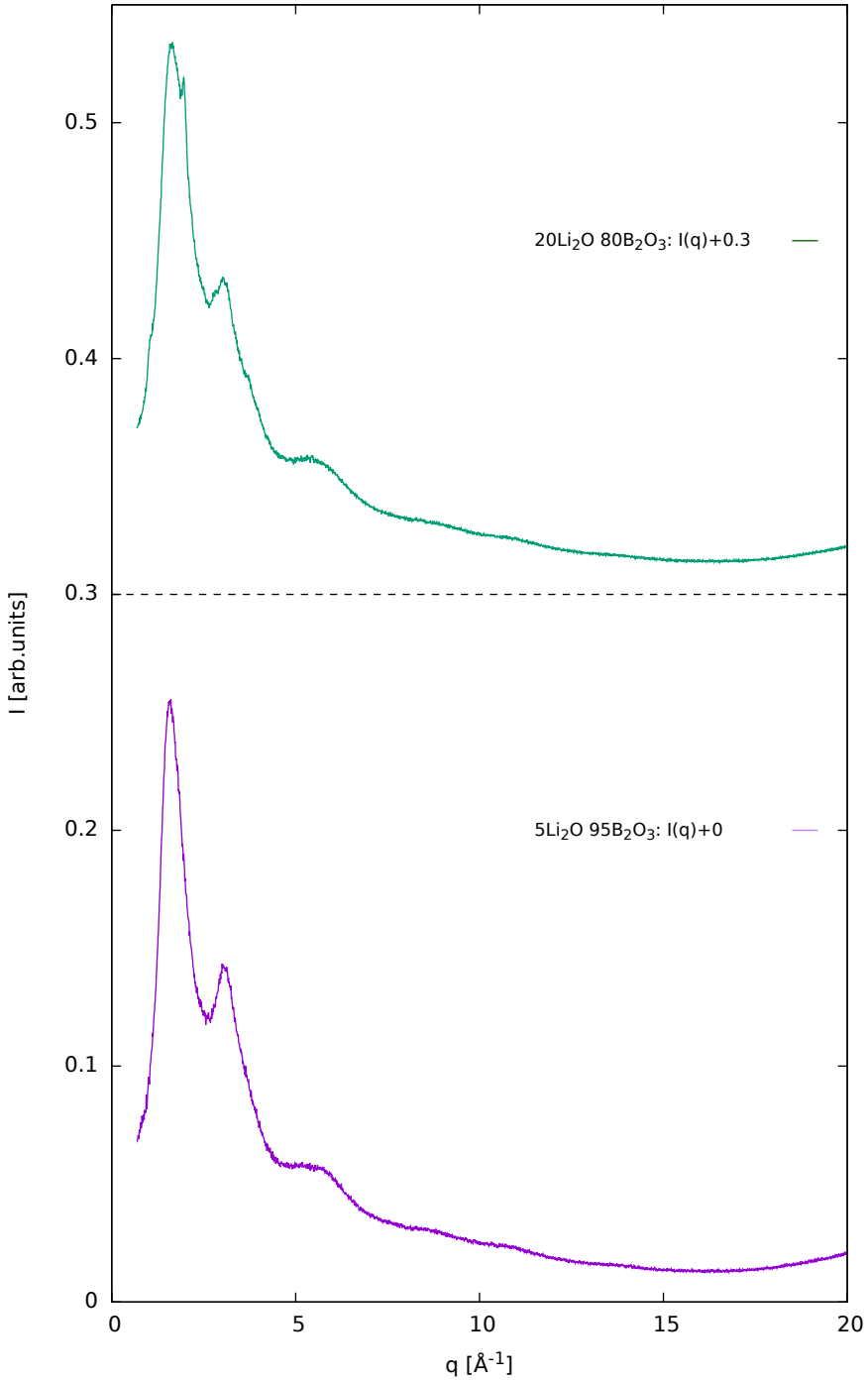

Figure 4.17: The normalized intensity $I(q)$ of $x\mathrm{Li_2O}$ $(100-x)\mathrm{B_2O_3}$ measured at the TU Wien/PANalytical machine. The 20Li-diagram is shifted by 0.3.

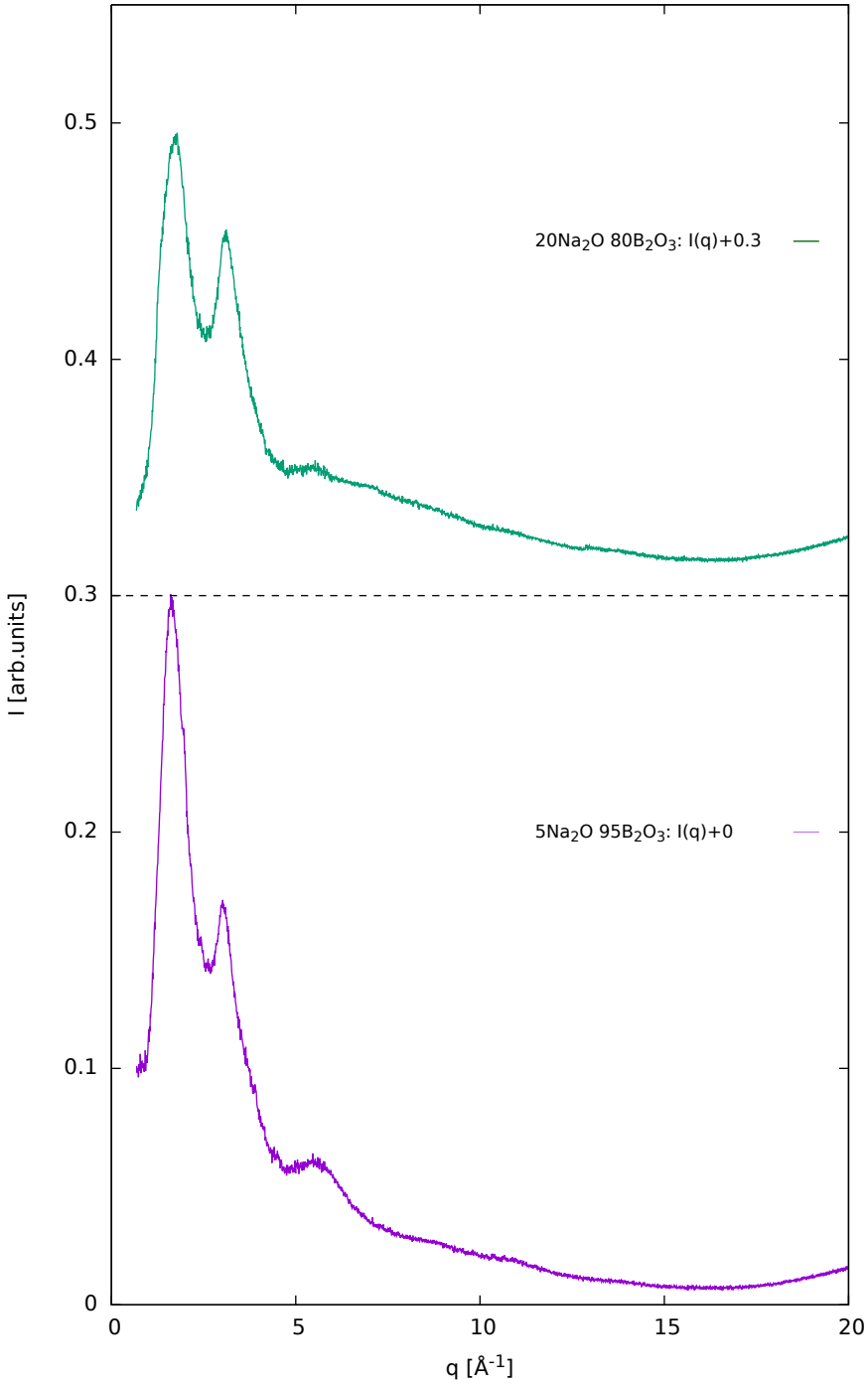

Figure 4.18: The normalized intensity $I(q)$ of $x\mathrm{Na_2O}$ $(100-x)\mathrm{B_2O_3}$ measured at the TU Wien/PANalytical machine. The 20Na-diagram is shifted by 0.3.

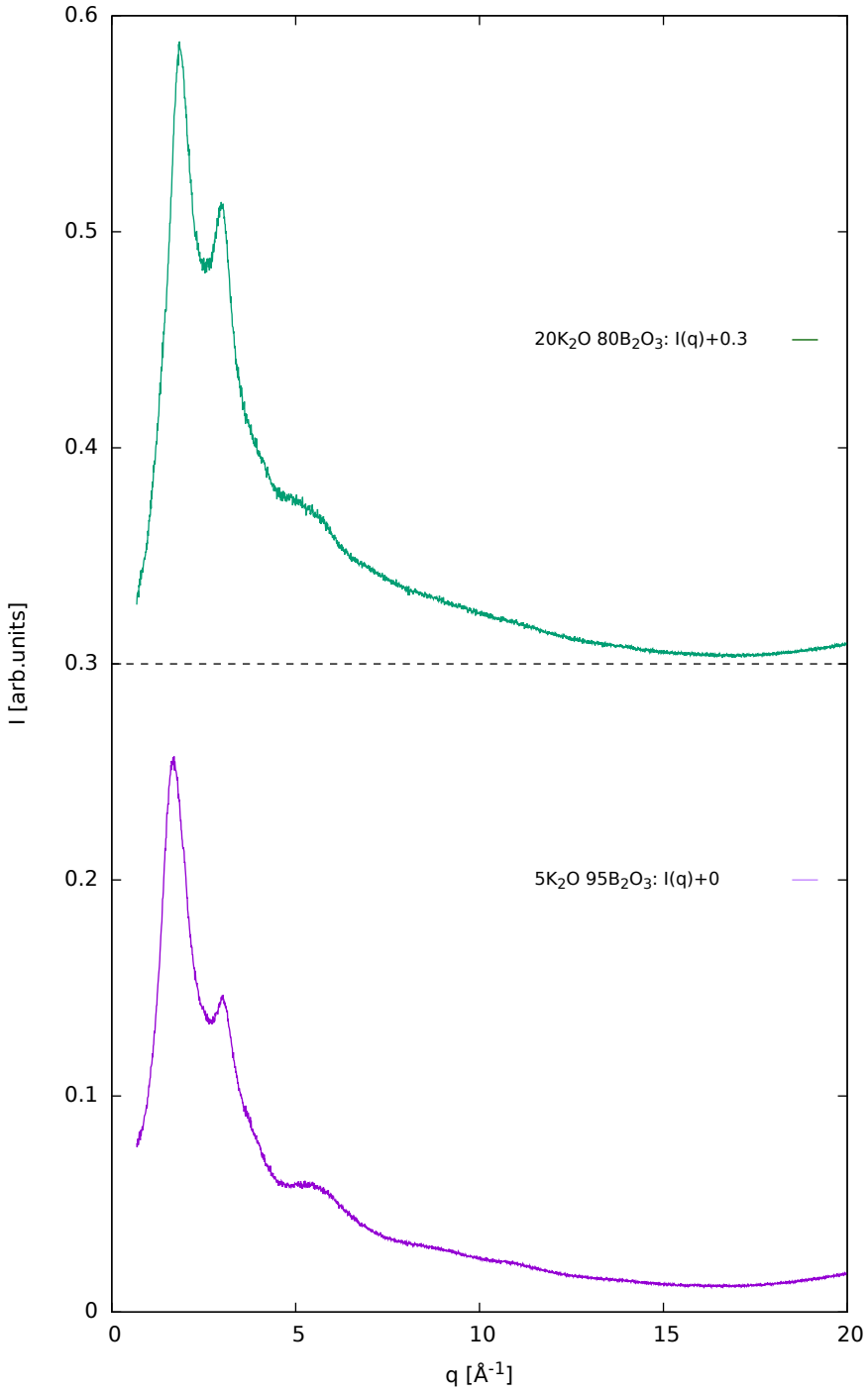

Figure 4.19: The normalized intensity $I(q)$ of $x\mathrm{K_2O}$ $(100-x)\mathrm{B_2O_3}$ measured at the TU Wien/PANalytical machine. The 20K-diagram is shifted by 0.3.

The peaks of the sample $15Rb_2O\ 85B_2O_3$ are less pronounced and show the same height, which is hardly explainable. We deduce that these results are not reliable.

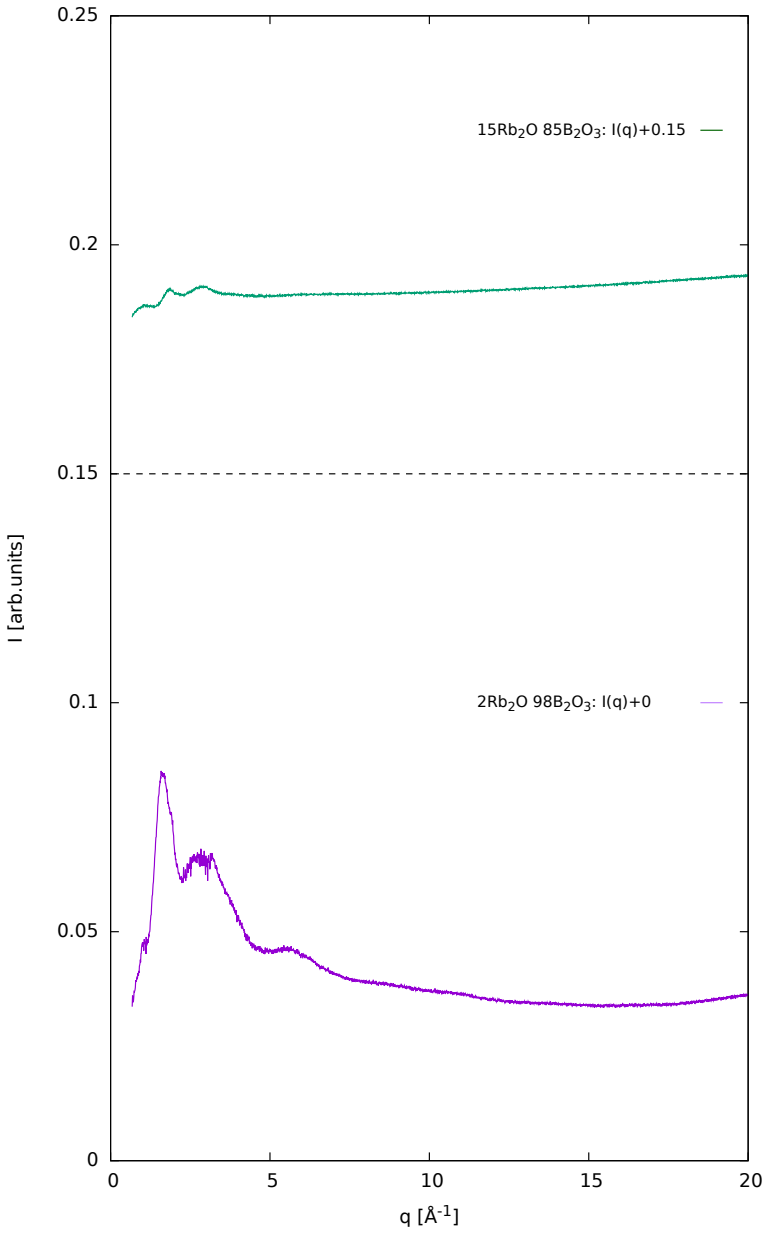

Figure 4.20: The normalized intensity $I(q)$ of $x\mathrm{Rb}_2\mathrm{O}\ (100-x)\mathrm{B}_2\mathrm{O}_3$ measured at the TU Wien/PANalytical machine. The 15Rb-diagram is shifted by 0.15.

The $I(q)$ results of $10Cs_2O\ 90B_2O_3$ and $15Cs_2O\ 85B_2O_3$ show a very noisy step at approximately $q = 5$ Å^{-1}, which adversely affects the structure factor $S_{\mathrm{FZ}}(q)$ and the total PDF $g(r)$. This artefact was found only in these two samples and can be probably explained by the moisture-crystallization (see chapter 4.3).

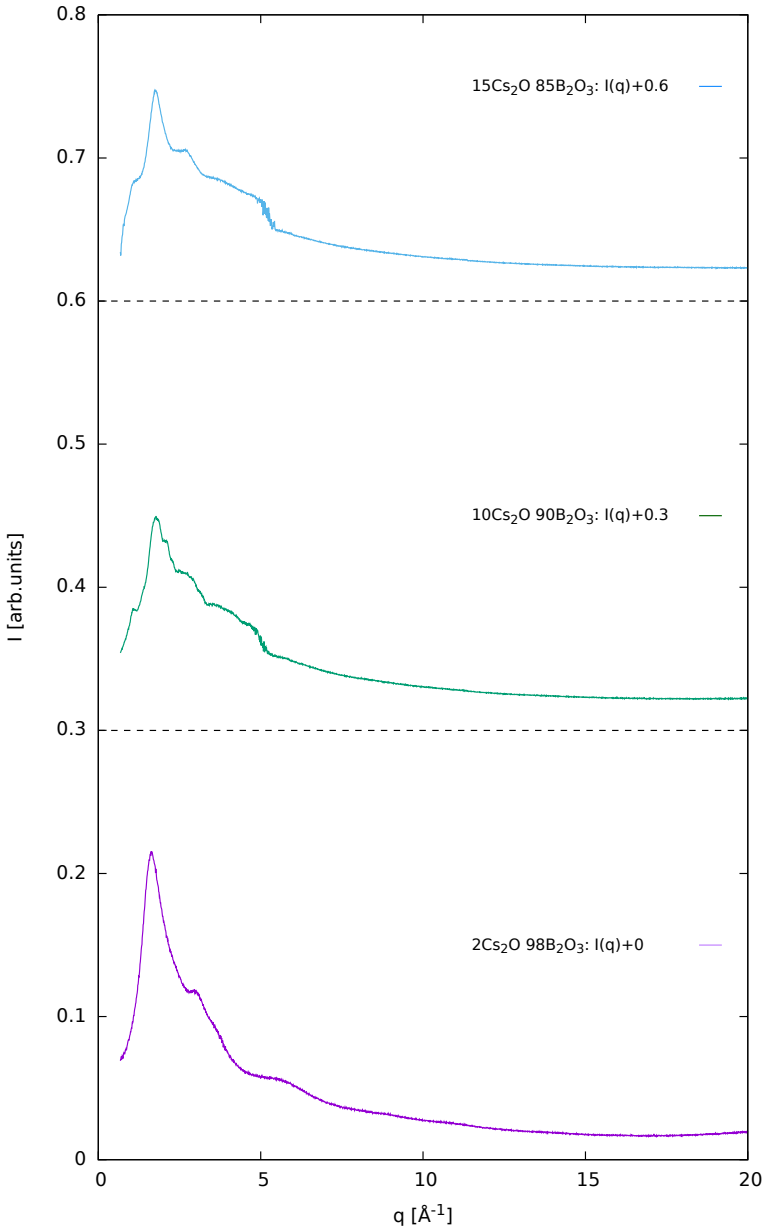

Figure 4.21: The normalized intensity $I(q)$ of $xCs_2O\ (100-x)B_2O_3$ measured at the TU Wien/PANalytical machine. The diagrams are shifted

4.2.2 Structure factor $S_{FZ}(q)$

Special features of the structure factor will be discussed together with the features of the reduced structure factor $F(q)$ in the next section 4.2.3.

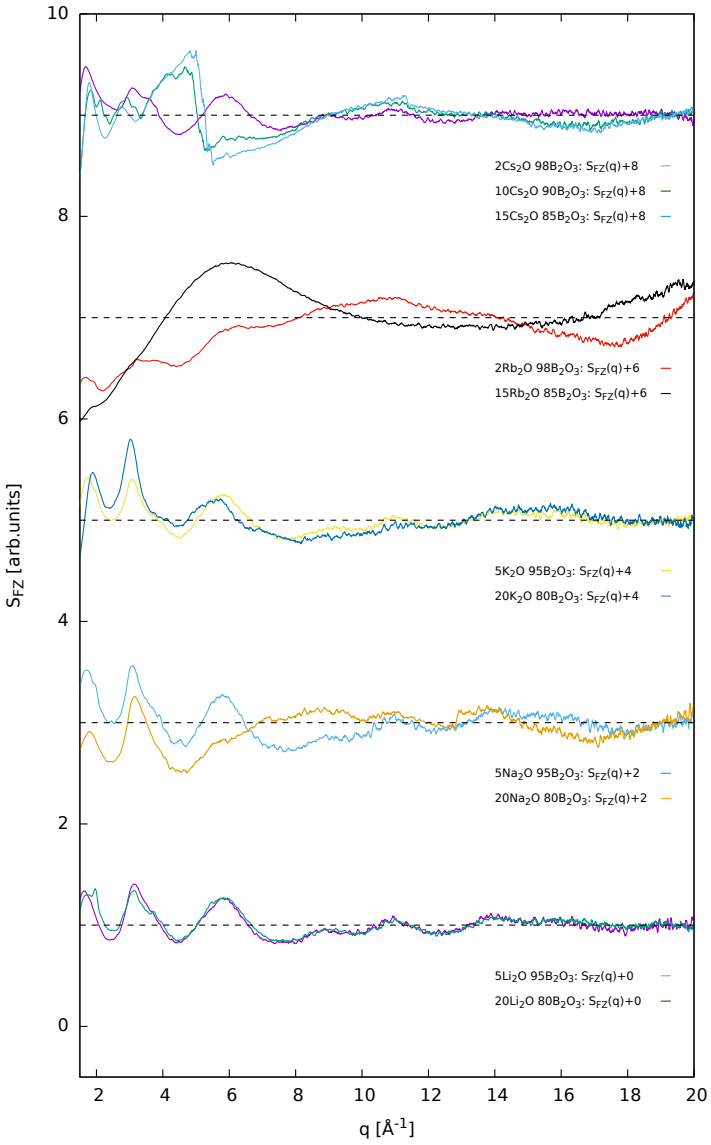

Figure 4.22: The *Faber-Ziman* structure factor $S_{\mathrm{FZ}}(q)$ of the alkali borate glasses $x\mathrm{A_2O}\ (100-x)\mathrm{B_2O_3}$ with A=Li, Na, K, Rb and Cs from measurements at the TU Wien/PANalytical machine. The diagrams are shifted by 2.

4.2.3 Reduced structure factor F(q)

Characteristics of $F(q)$ are:

- With the increase of the alkali-concentration the first peak at approximately $q \sim 1.7$ Å^{-1} slightly shifts to higher q-values, except of the unreliable measurement of $15Rb_2O$ $85B_2O_3$.
- There is no correlation between the peak height or peak position of the second peak at $q \sim 3.2$ Å^{-1} and the alkali concentration.
- The curve of $20Li_2O$ $80B_2O_3$ shows a spike at $q \sim 1.95$ Å^{-1} as observed before by the $I(q)$ evaluations 4.2.1. The failed $15Rb_2O$ $85B_2O_3$ measurement leads to a wavelike look of the curve, which has not any common features with the other samples. The steep, noisy slopes at $q \sim 5$ Å^{-1} of $10Cs_2O$ $90B_2O_3$ and $15Cs_2O$ $85B_2O_3$ also indicate either a measurement or a sample preparation error.

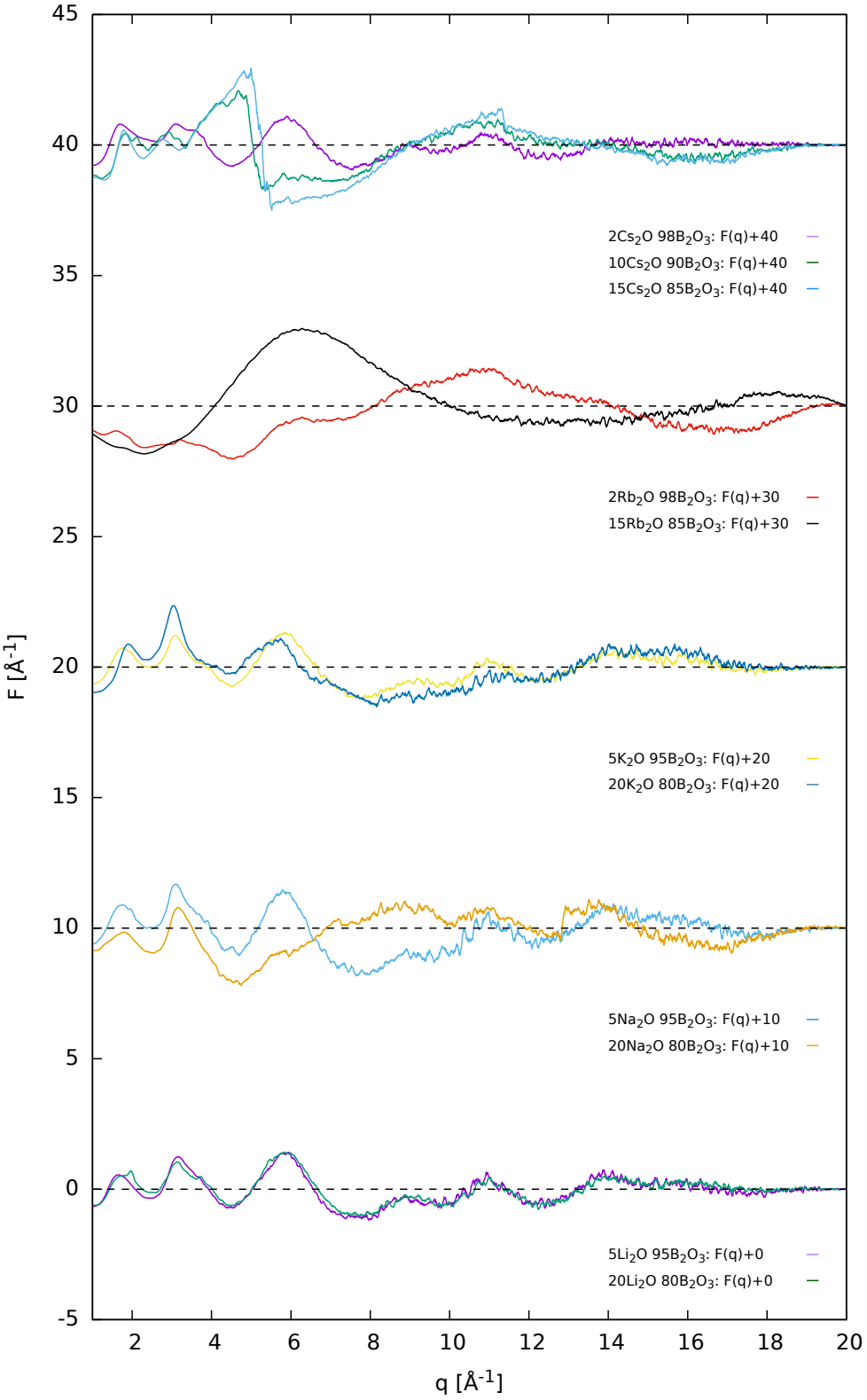

Figure 4.23: The reduced structure factor $F(q)$ of the alkali borate glasses $x\mathrm{A_2O}$ $(100-x)\mathrm{B_2O_3}$ with A=Li, Na, K, Rb, Cs measured at the TU Wien/PANalytical machine. The diagrams are shifted by 10.

4.2.4 Density function D(r)

Two vertical red lines at $r = 1.37$ Å and $r = 2.37$ Å cross the first and the second peak of almost all samples, except of $15Rb_2O$ $85B_2O_3$, $10Cs_2O$ $90B_2O_3$ and $15Cs_2O$ $85B_2O_3$ and belong to the BO(1) and OO(1) distances.

- To proof the increase of BO_4 molecule concentration, the first peak should shift to higher r-values, which is the case only for Li and Na samples. The K samples show inverse behaviour. The Rb and the Cs samples are not comparable due to the unsuccessful measurements of the higher alkali-concentrated samples of Rb and Cs.

- The second peak at $r = 2.37$ Å is higher for samples with higher alkali concentrations. The height of the first peak shows no correlation.
  Concluding, the peaks are only half as large and the FWHM of the peaks are almost the same compared with the Petra III measurements 4.1.4. Hence, calculating the coordination number is not reliable for these measurements.

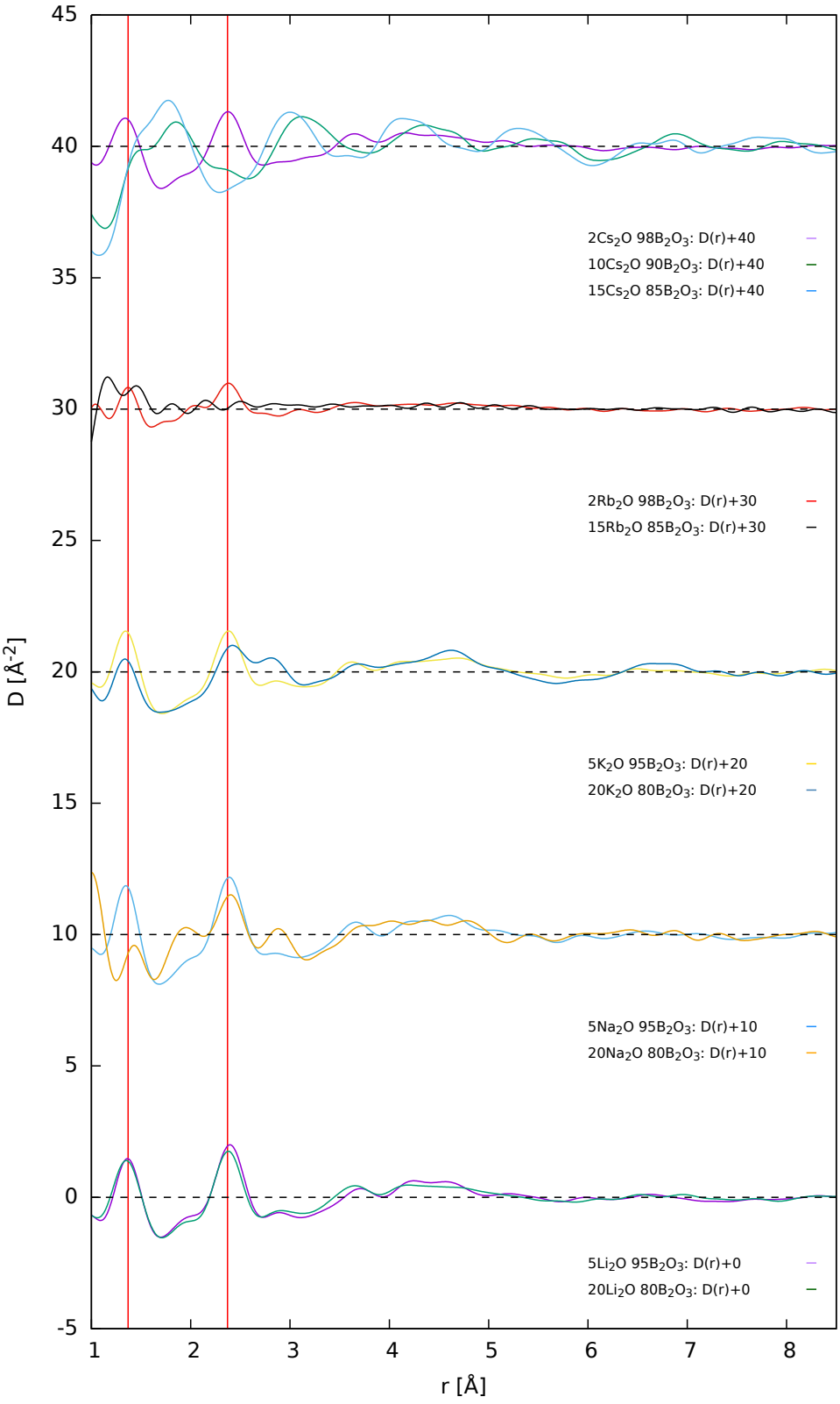

Figure 4.24: The density function $D(r)$ of the alkali borate glasses $x\mathrm{A_2O}\ (100-x)\mathrm{B_2O_3}$ with A=Li, Na, K, Rb and Cs measured at the TU Wien/PANalytical machine. The two vertical red lines describe the nearest-neighbour distance BO(1) at 1.37 Å and the nearest-neighbour distance OO(1) at 2.37 Å, see table 1.1, respectively table 1.2. The diagrams are shifted by 10.

4.2.5 Total pair distribution function PDF g(r)

The total PDF g(r) is similar to the density function D(r) due to equation 3.26, hence for a detailed discussion the reader is referred to the previous section 4.2.4.

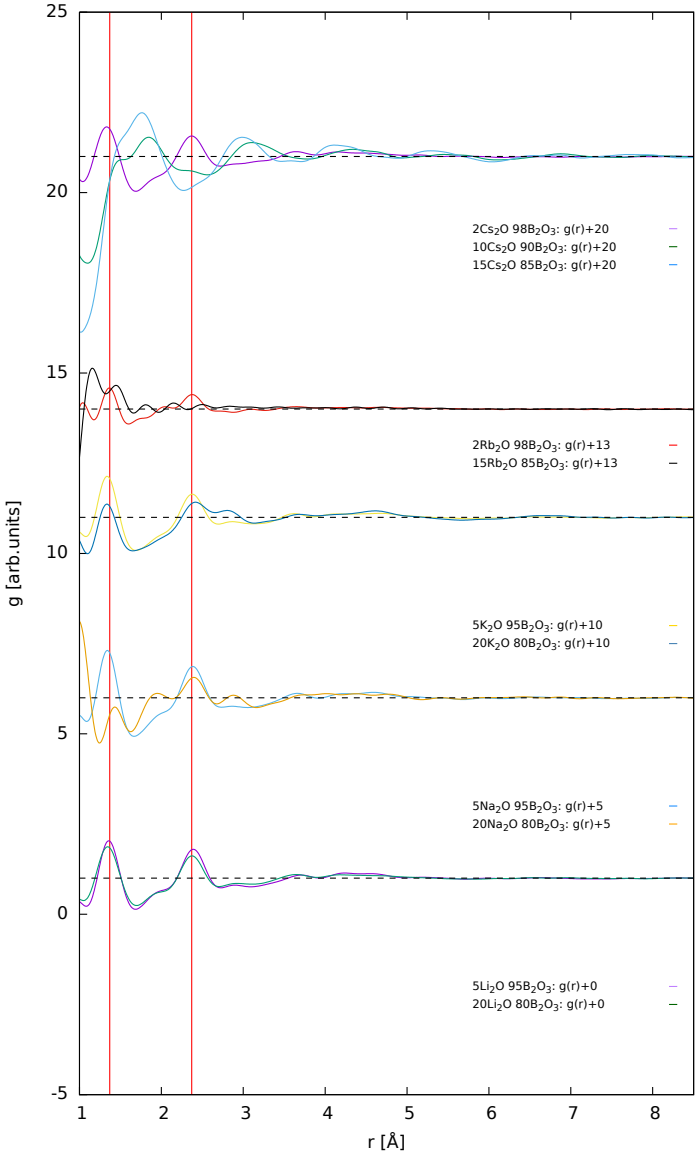

Figure 4.25: The PDF $g(r)$ of the alkali borate glasses xA_2O $(100-x)B_2O_3$ with A=Li, Na, K, Rb and Cs measured at the TU Wien/PANalytical machine. The two vertical red lines describe the nearest-neighbour distance BO(1) at 1.37 Å and the nearest-neighbour distance OO(1) at 2.37 Å, see table 1.1, respectively table 1.2. The diagrams are shifted by 5.

4.3 Measurement results with Cu-Anode

The measurements were done at an Empyrean PANalytical X-ray diffractometer at the TU Wien using X-rays with a wavelength of $\lambda = 1.5431$ Å from a Cu-Anode and a line detector. The sample were prepared as powder in soda-lime capillaries with 1 mm diameter. The measurement series with a Cu-Anode were accomplished on June 2016 and were performed in a range up to $q \sim 7$ Å^{-1} only to save time.

4.3.1 Intensity I(q)

For the measurement series with an Ag-Anode in March/May and for the measurement series with a Cu-Anode in June the same powder capillary samples were used. In the meantime an evident surface crystallization process of the $x\mathrm{A_2O}$ $(100-x)\mathrm{B_2O_3}$ structure triggered by $\mathrm{H_2O}$ molecules providing hydrogen atoms to the glass structure had occurred. The measured samples exhibit Bragg reflexes combined with the intensity distribution of the remaining amorphous part of the sample (see figure 4.26).
The measurement results performed on May 2016 of $20\mathrm{Li_2O}$ $80\mathrm{B_2O_3}$ already displayed a small prong at $q \sim 1.95$ Å^{-1}. One month later the 20Li-curve showed the strongest pronounced Bragg reflexes.

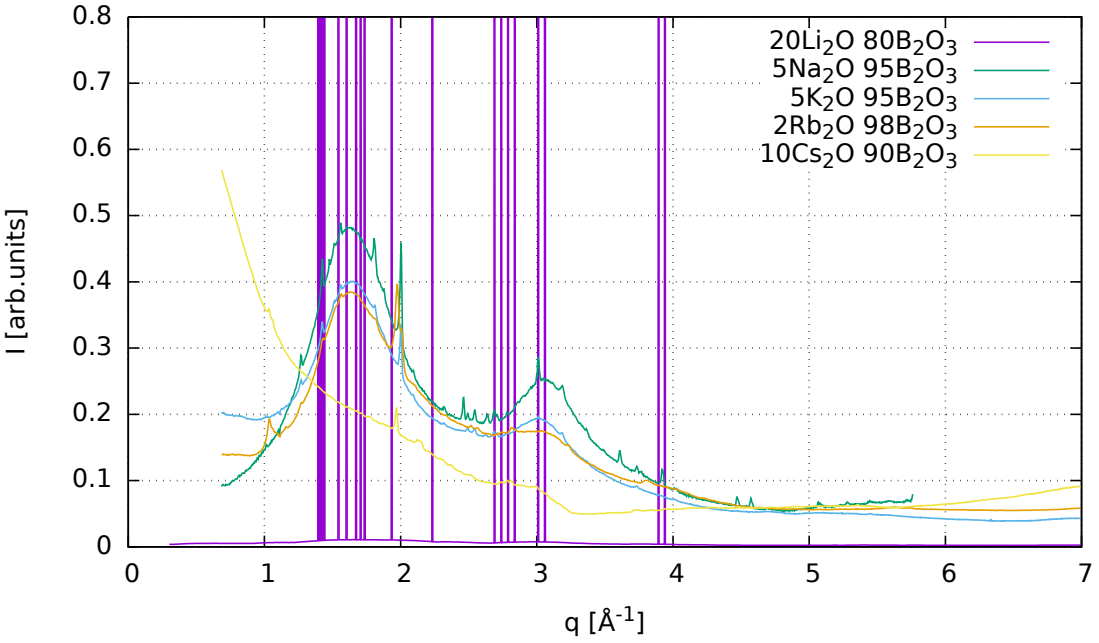

Figure 4.26: The normalized intensity $I(q)$ of $x\mathrm{A_2O}$ $(100-x)\mathrm{B_2O_3}$ with A=Li, Na, K, Rb and Cs measured at the TU Wien/PANalytical machine.

The content of potential crystalline phases was examined by the software *Highscore* (see figure 4.27). The software is able to handle the amorphous part as background intensity and subtract it from the remaining intensity as to obtain the pure information from the Bragg reflexes. Comparing the positions of the Bragg reflexes with

a database[3] of a wide range of minerals yields possible crystalline structures.

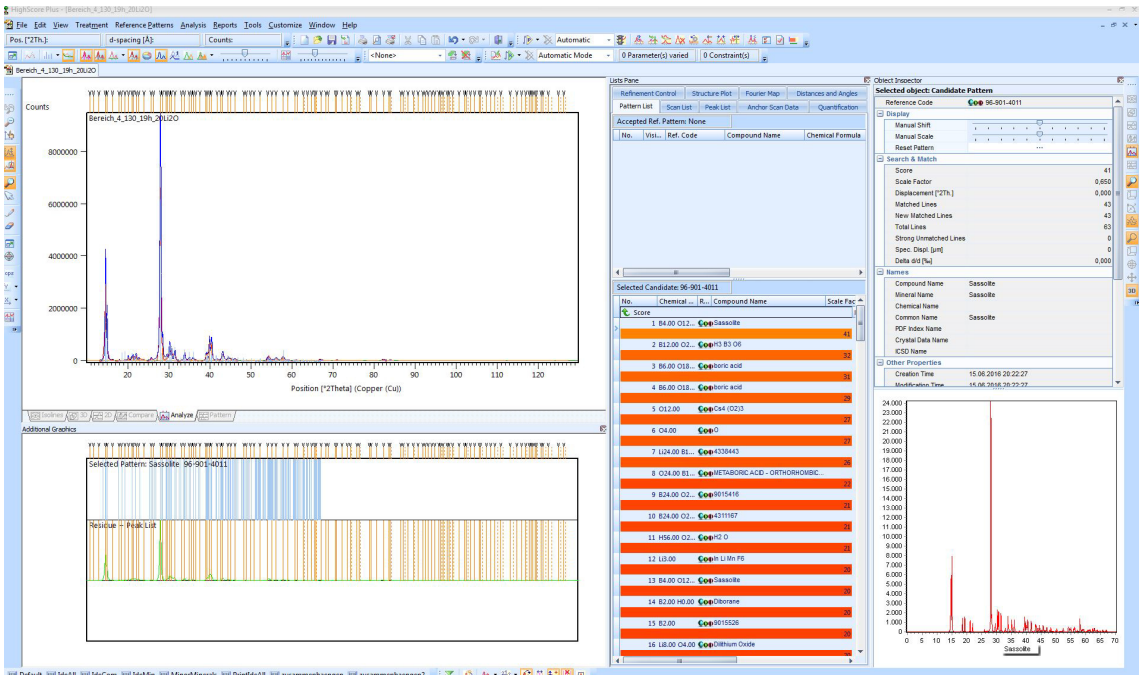

Figure 4.27: The evaluation of Bragg reflexes of $20Li_2O$ $80B_2O_3$ by the software *Highscore*.

The following crystalline structures were found in every measured sample: $B_4O_{12}H_{12}$ (sassolite), $H_3B_3O_6$ and $B_6O_{18}H_{18}$ (boric acid).
The result is a strong evidence that hydrogen atoms are responsible for changing the structure from amorphous to crystalline.

[3]Used database for evaluation: Crystallography Open Database (COD):http://www.crystallography.net/cod/

4.3.2 Structure factor $S_{FZ}(q)$

The structure factors of $20Li_2O\ 80B_2O_3$ shows Bragg reflexes.

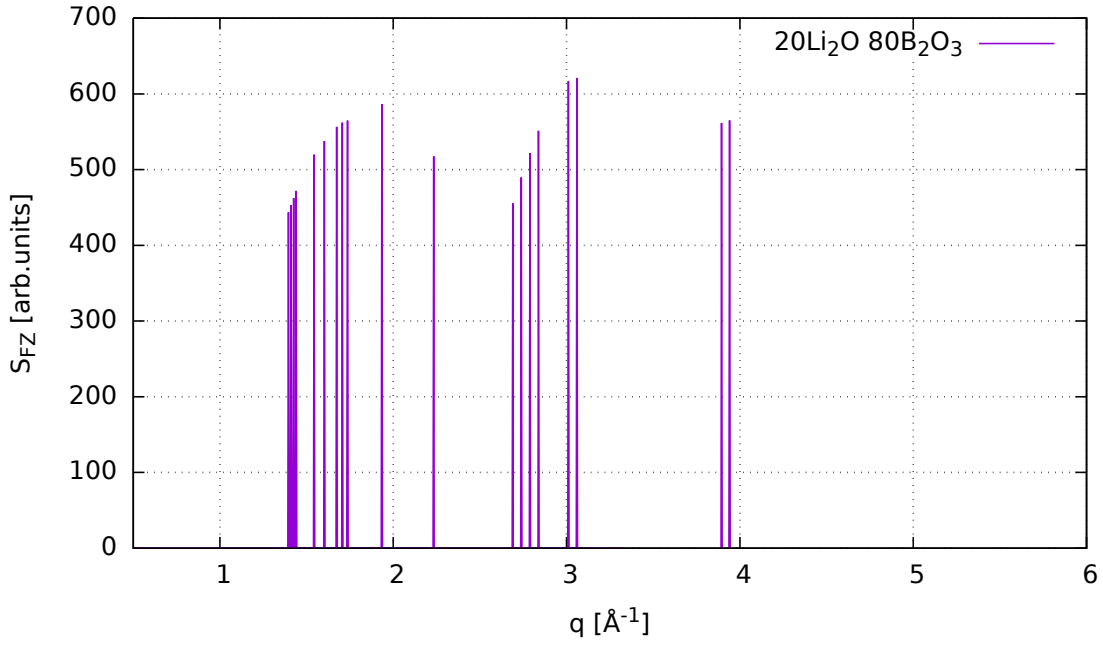

Figure 4.28: The *Faber-Ziman* structure factor $S_{\mathrm{FZ}}(q)$ of $20Li_2O\ 80B_2O_3$ measured at the TU Wien/PANalytical machine.

The structure factor of the other samples display some spikes superimposed by the amorphous curve.

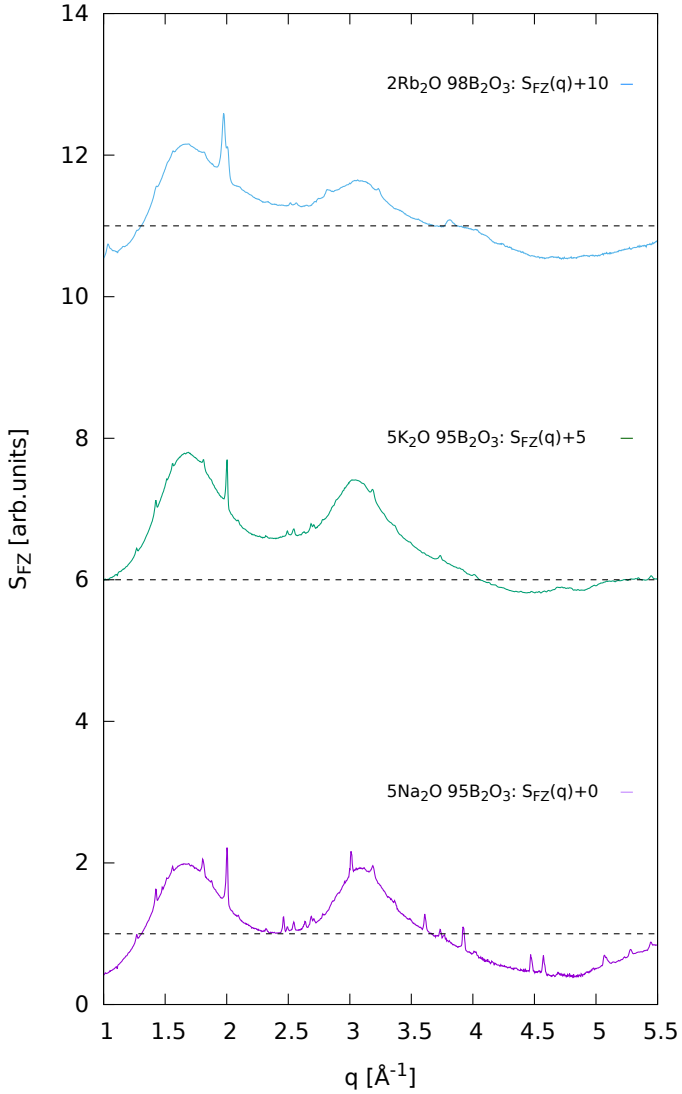

Figure 4.29: The *Faber-Ziman* structure factor $S_{\mathrm{FZ}}(q)$ of the alkali borate glasses $x\mathrm{A_2O}$ $(100-x)\mathrm{B_2O_3}$ with A=Na, K and Rb measured at the TU Wien/PANalytical machine. The diagrams are shifted by 5.

4.3.3 Reduced structure factor F(q)

The positions of the peaks are similar of all samples. The most distinct spike of all three samples is located at approximately $q = 2$ Å^{-1}.

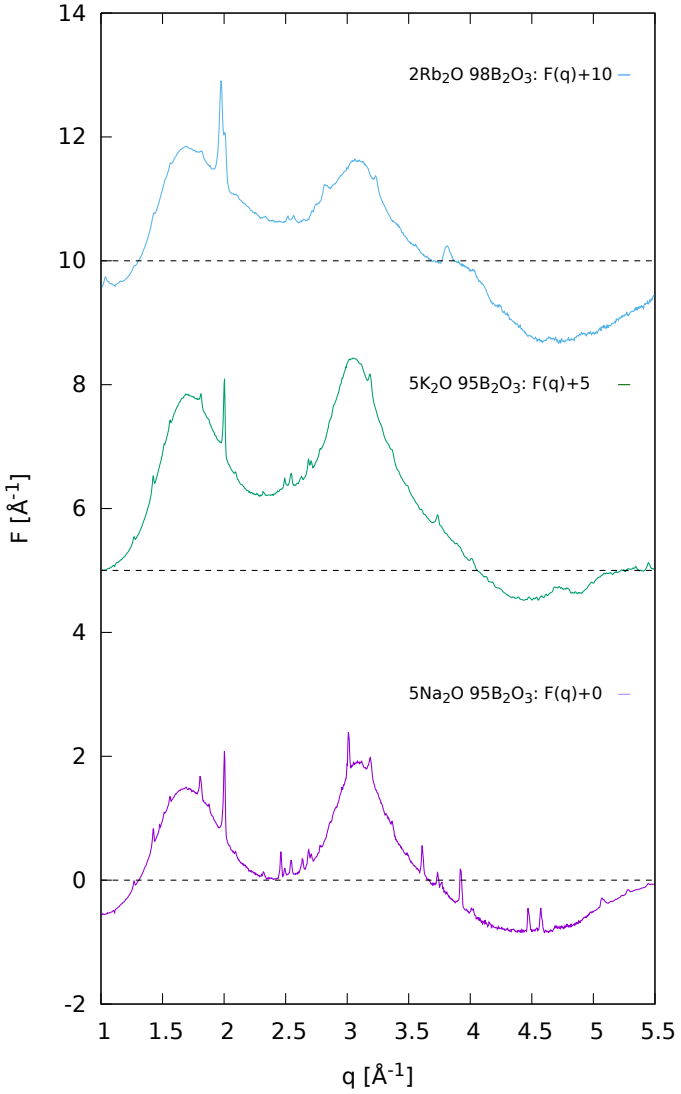

Figure 4.30: The reduced structure factor $F(q)$ of the alkali borate glasses $x\mathrm{A_2O}$ $(100-x)\mathrm{B_2O_3}$ with A=Na, K, and Rb measured at the TU Wien/PANalytical machine. The diagrams are shifted by 5.

4.3.4 Density function D(r)

Due to a very small measured q-range ($q_{\max} = 7.4$ [Å^{-1}]) low r-regions could not be evaluated correctly for the density function $D(r)$, which explains the absence of the first peak at approximately $r \sim 1.37$ [Å]. The second peak at approximately $r \sim 2.37$ [Å] is present.

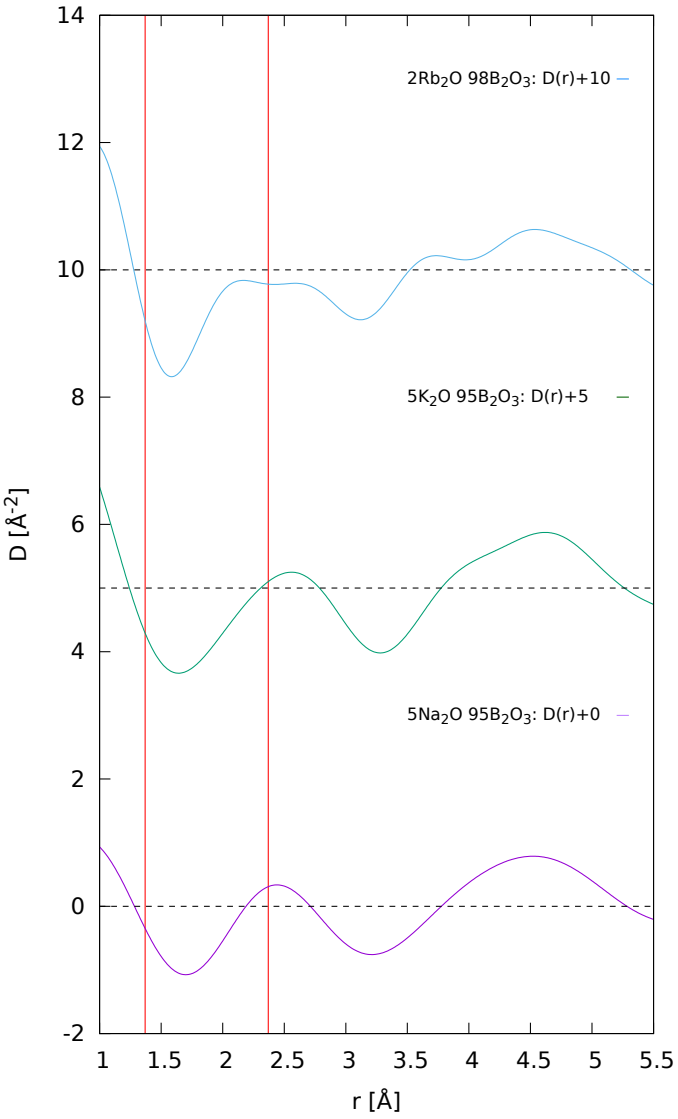

Figure 4.31: The density function $D(r)$ of the alkali borate glasses $x\mathrm{A_2O}\ (100-x)\mathrm{B_2O_3}$ with A=Na, K and Rb measured at the TU Wien/PANalytical machine. The two vertical red lines describe the first nearest-neighbour distance BO(1) at 1.37 Å and the first nearest-neighbour distance OO(1) at 2.37 Å, see table 1.1, respectively table 1.2. The diagrams are shifted by 5.

4.3.5 Total pair distribution function g(r)

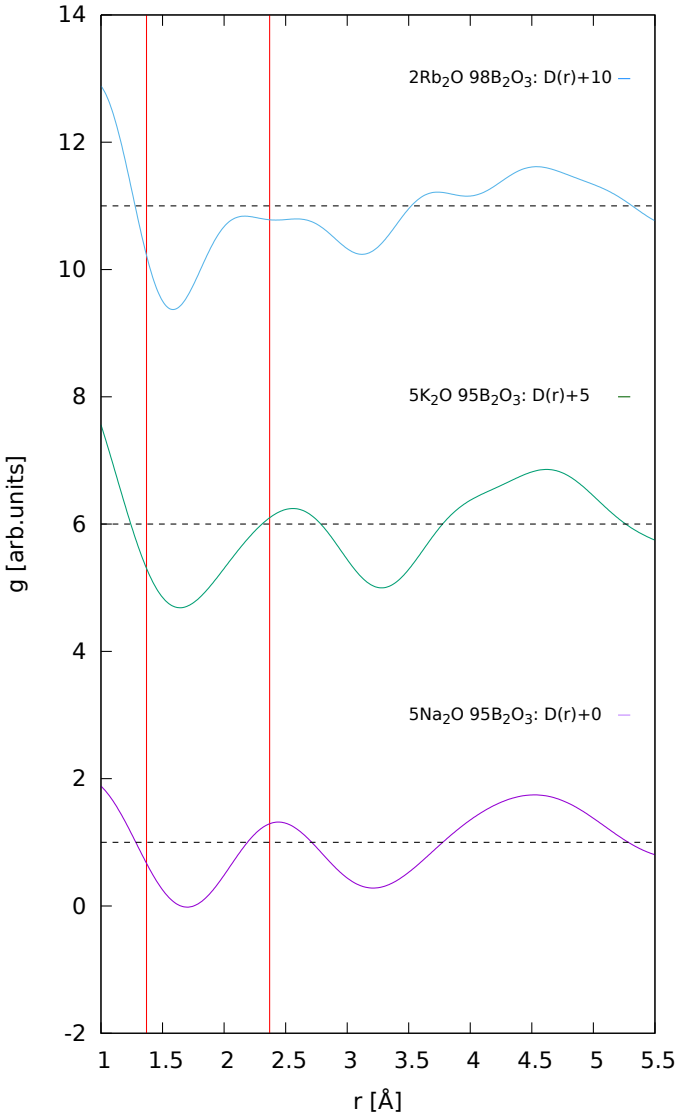

Figure 4.32: The PDF $g(r)$ of the alkali borate glasses xA_2O $(100-x)B_2O_3$ with A=Na, K and Rb measured at the TU Wien/PANalytical machine. The two vertical red lines describe the nearest-neighbour distance BO(1) at 1.37 Å and the nearest-neighbour distance OO(1) at 2.37 Å, see table 1.1, respectively table 1.2. The diagrams are shifted by 5.

4.4 PDFgetX2 versus PDFgetX3

4.4.1 Measurement results with synchrotron radiation

As an example $S_{\mathrm{FZ}}(q)$, $F(q)$ and $D(r)$ of $2Rb_2O\ 98B_2O_3$ and $10Cs_2O\ 90B_2O_3$ evaluated by PDFgetX2 and PDFgetX3 respectively, are compared.
The most striking difference is the height difference between the curves. The peaks of the density function $D(r)$ evaluated by PDFgetX3 are far too small to gain a reasonable coordination number $\bar{n}_\alpha^\beta$. In contrast to $D(r)$ evaluated by PDFgetX2 too many small peaks arise at $r > 4$ Å (see figures 4.35 and 4.38), which leads to the conclusion that every other peak is an artefact. This wavelike behaviour could not be diminished by changing the parameter r_{poly} or by truncating q_{max} to zero. Thus, the $D(r)$-curve evaluated by PDFgetX3 is only meaningful until $r \sim 4$ Å.

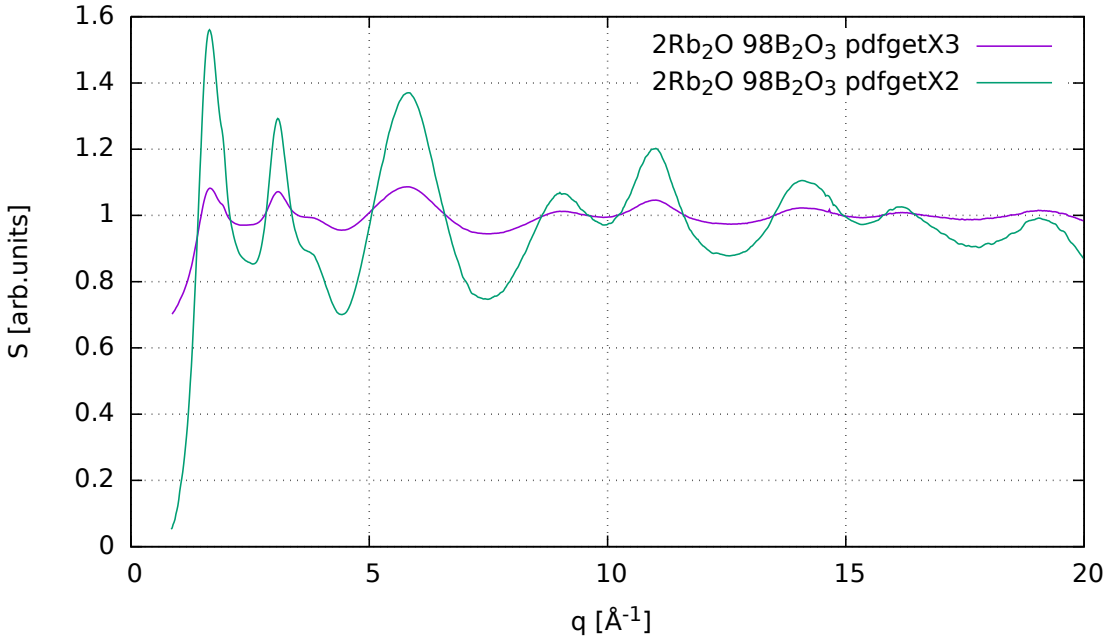

Figure 4.33: Comparison between the evaluations of $S_{\mathrm{FZ}}(q)$ of $2Rb_2O\ 98B_2O_3$ with PDFgetX2 and PDFgetxX3.

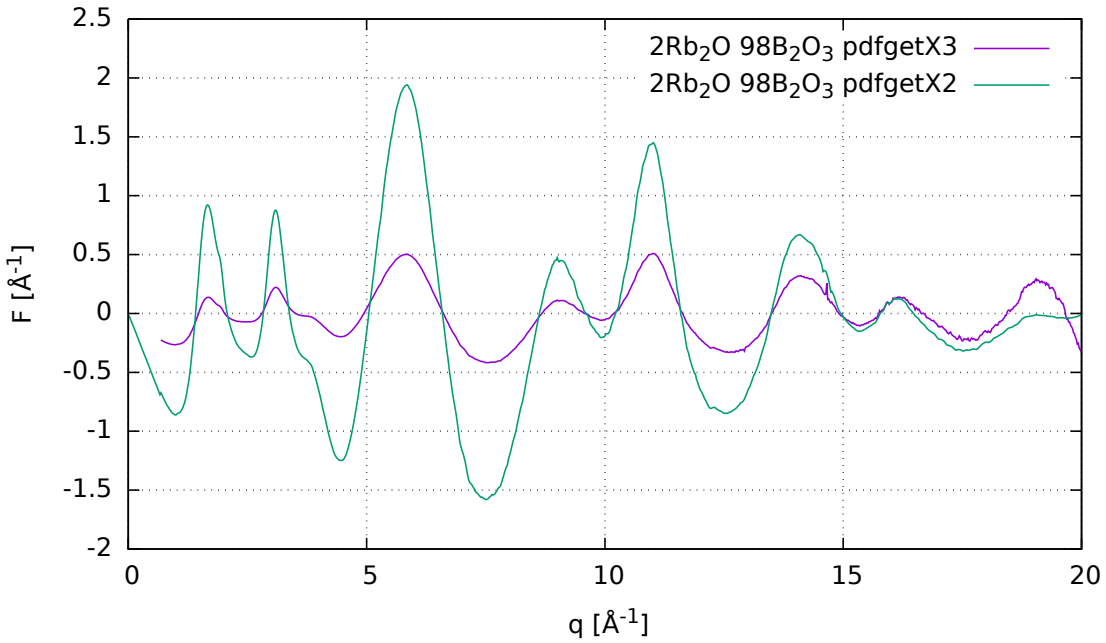

Figure 4.34: Comparison between the evaluations of $F(q)$ of $2Rb_2O$ $98B_2O_3$ with PDFgetX2 and PDFgetX3.

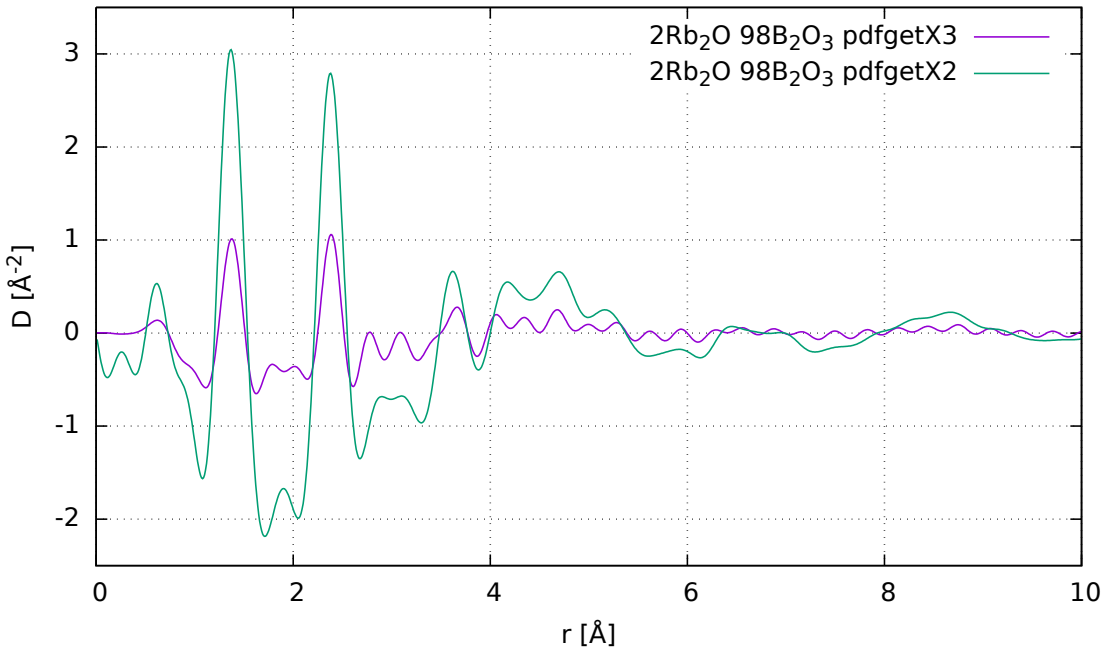

Figure 4.35: Comparison between the evaluations of $D(q)$ of $2Rb_2O$ $98B_2O_3$ with PDFgetX2 and PDFgetX3.

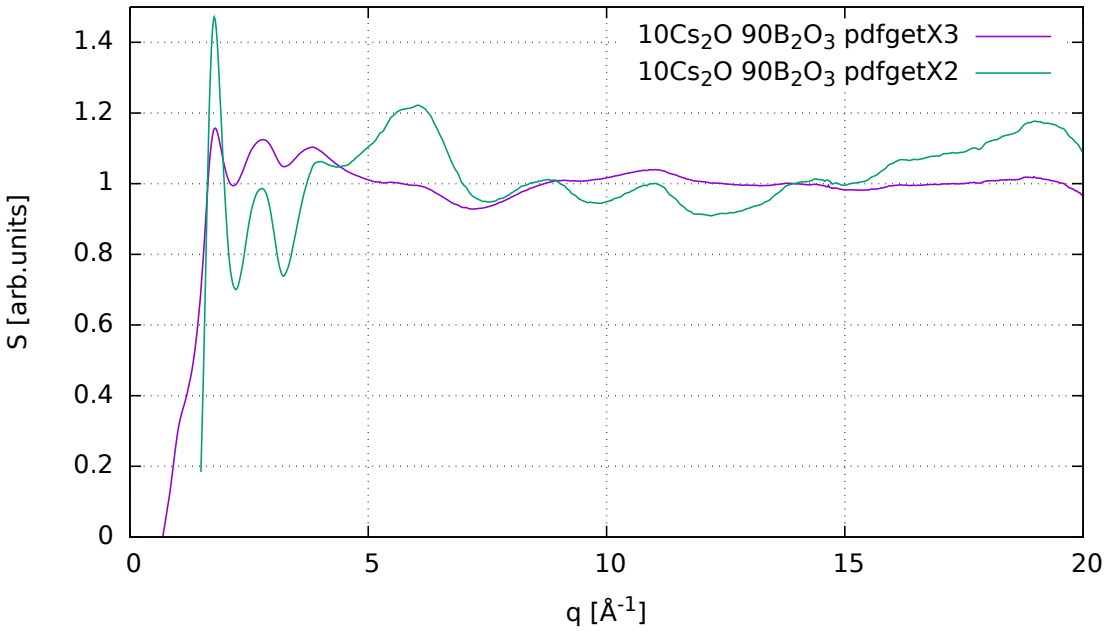

Figure 4.36: Comparison between the evaluations of $S_{\mathrm{FZ}}(q)$ of $10Cs_2O$ $90B_2O_3$ with PDFgetX2 and PDFgetxX3.

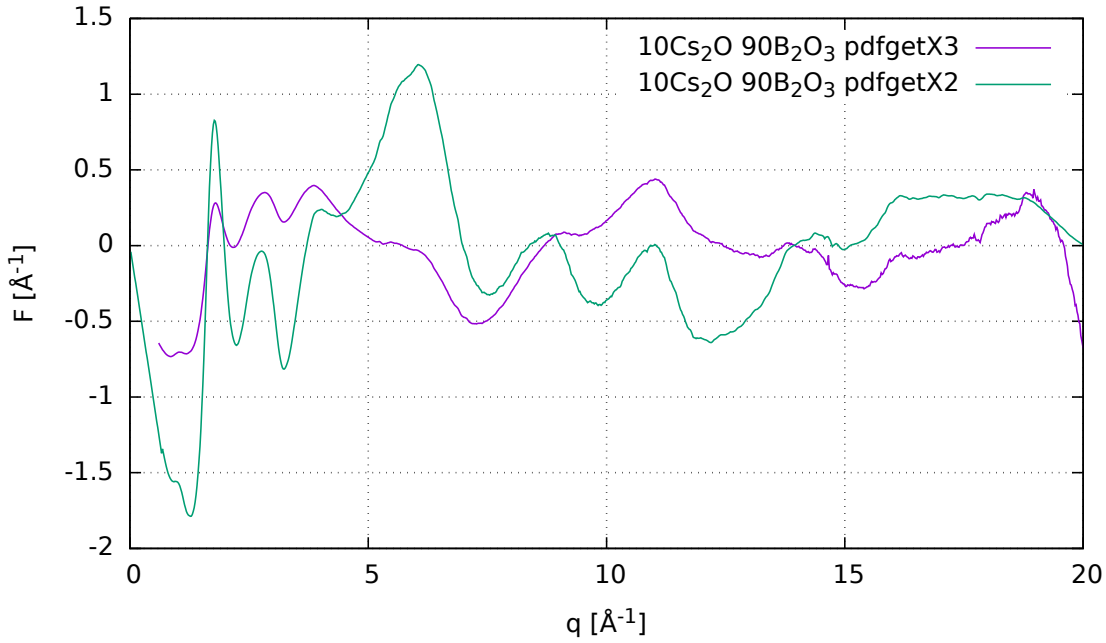

Figure 4.37: Comparison between the evaluations of $F(q)$ of $10Cs_2O$ $90B_2O_3$ with PDFgetX2 and PDFgetX3.

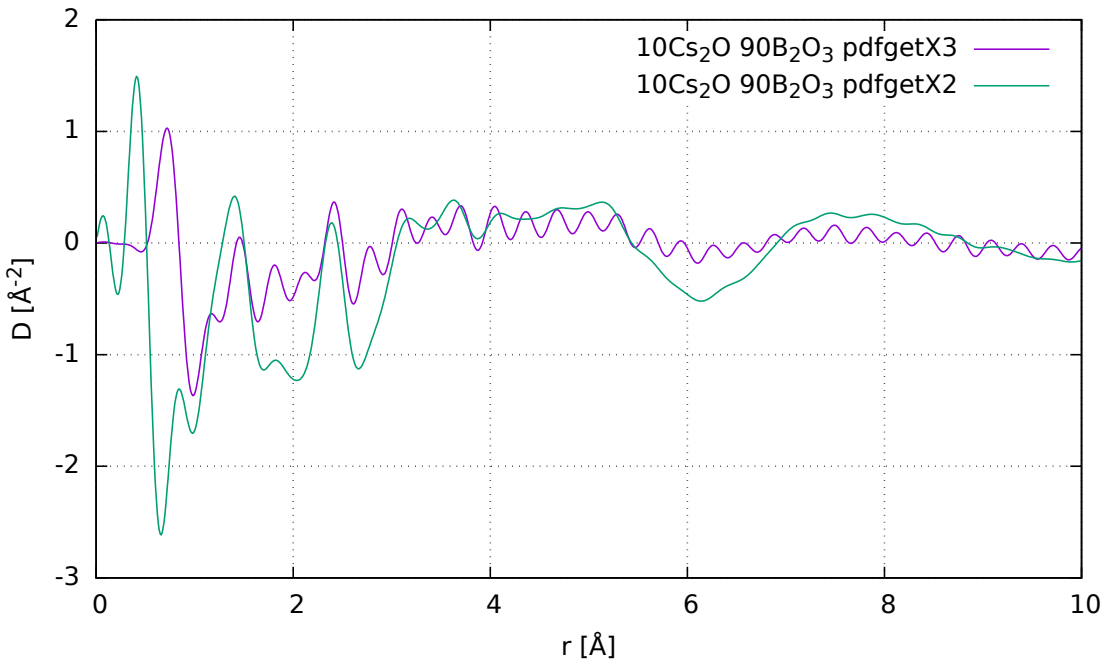

Figure 4.38: Comparison between the evaluations of $D(r)$ of $10Cs_2O\ 90B_2O_3$ with PDFgetX2 and PDFgetX3.

4.4.2 Measurement results with Ag-anode

The evaluation of the PANalytical measurements by PDFgetX2 and PDFgetX3 applied on $2Rb_2O\ 98B_2O_3$ and $10Cs_2O\ 90B_2O_3$ show similar differences as described in section [4.4.1]: Too less pronounced peaks and a too wavelike behaviour at about $r > 4$ Å for pdfgetX3 evaluations. Only the peak positions coincide.

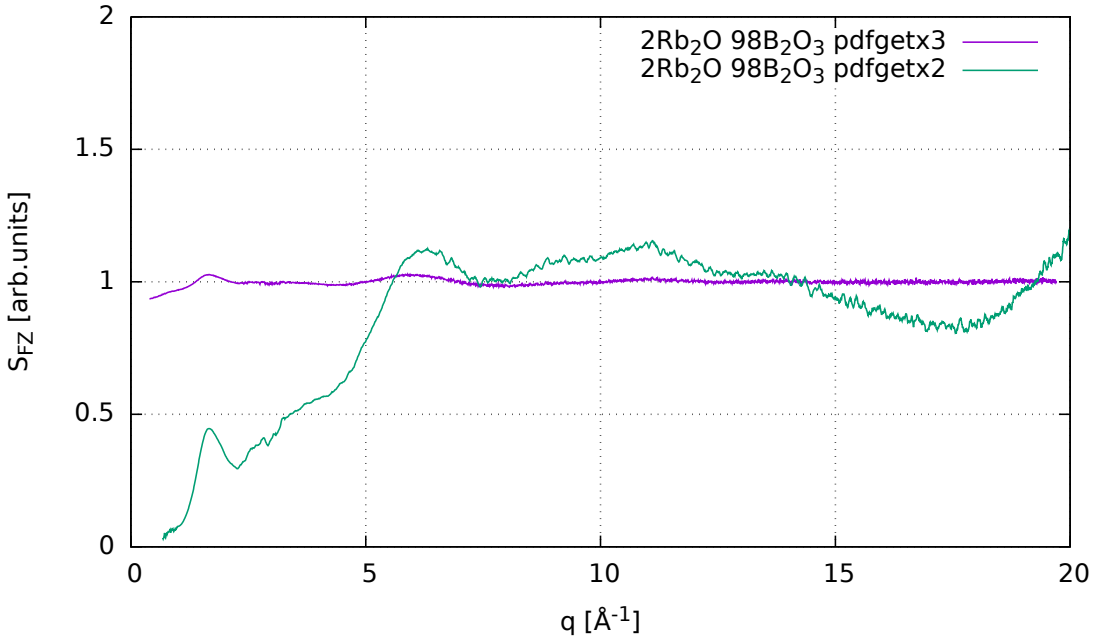

Figure 4.39: Comparison between the evaluations of $S_{\mathrm{FZ}}(q)$ of $2Rb_2O\ 98B_2O_3$ with PDFgetX2 and PDFgetX3.

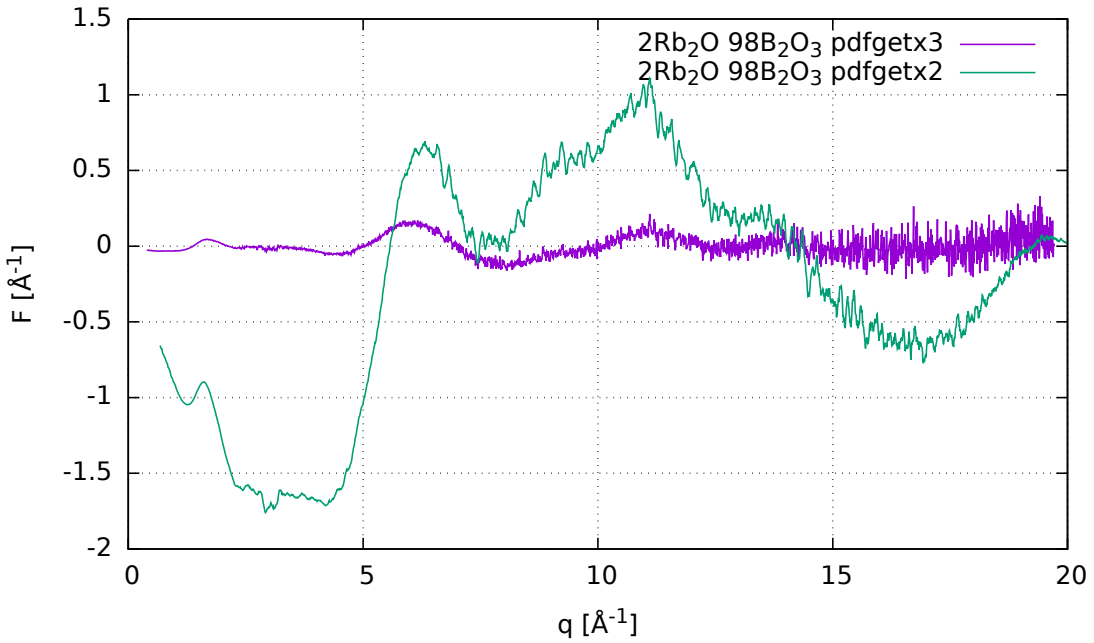

Figure 4.40: Comparison between the evaluations of $F(q)$ of $2Rb_2O$ $98B_2O_3$ with PDFgetX2 and PDFgetX3.

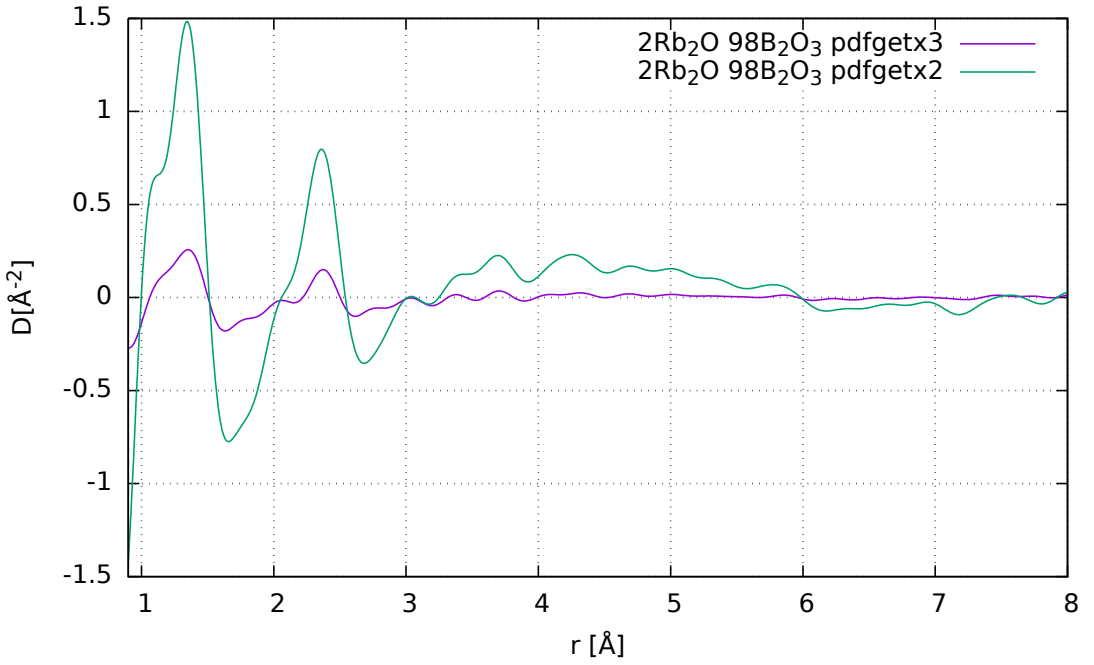

Figure 4.41: Comparison between the evaluations of $D(q)$ of $2Rb_2O$ $98B_2O_3$ with PDFgetX2 and PDFgetX3.

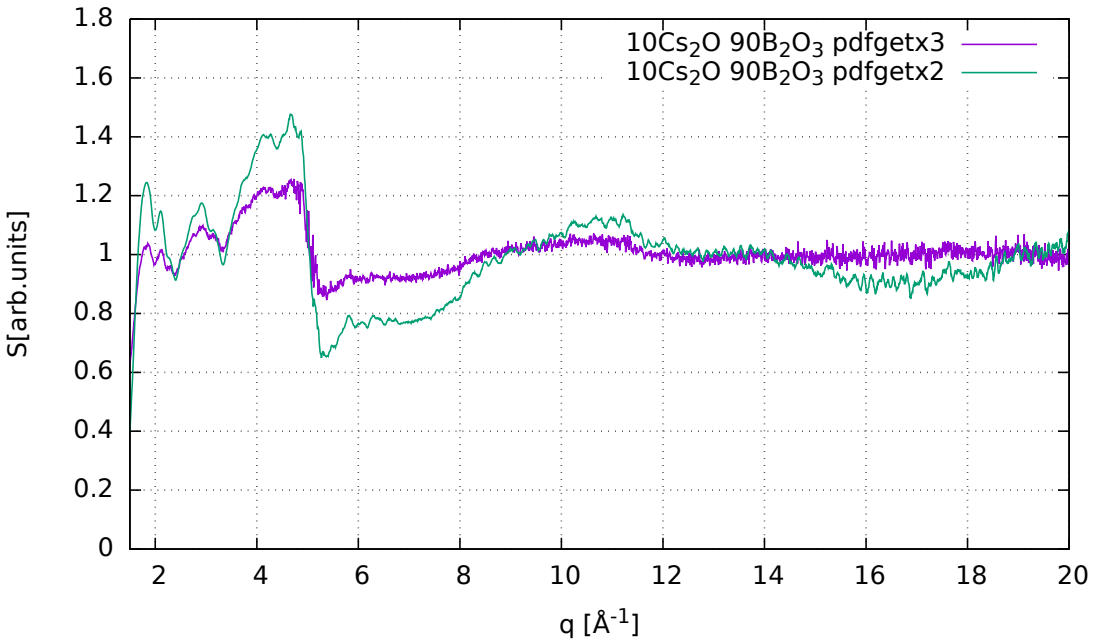

Figure 4.42: Comparison between the evaluations of $S_{\mathrm{FZ}}(q)$ of $10Cs_2O\ 90B_2O_3$ with PDFgetX2 and PDFgetX3.

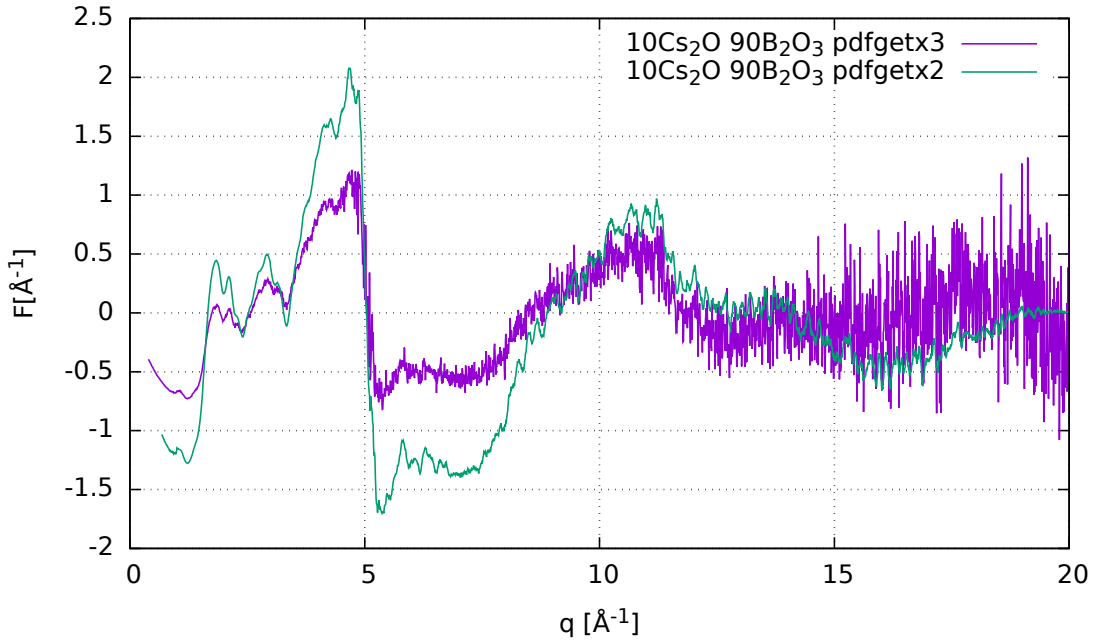

Figure 4.43: Comparison between the evaluations of $F(q)$ of $10Cs_2O\ 90B_2O_3$ with PDFgetX2 and PDFgetX3.

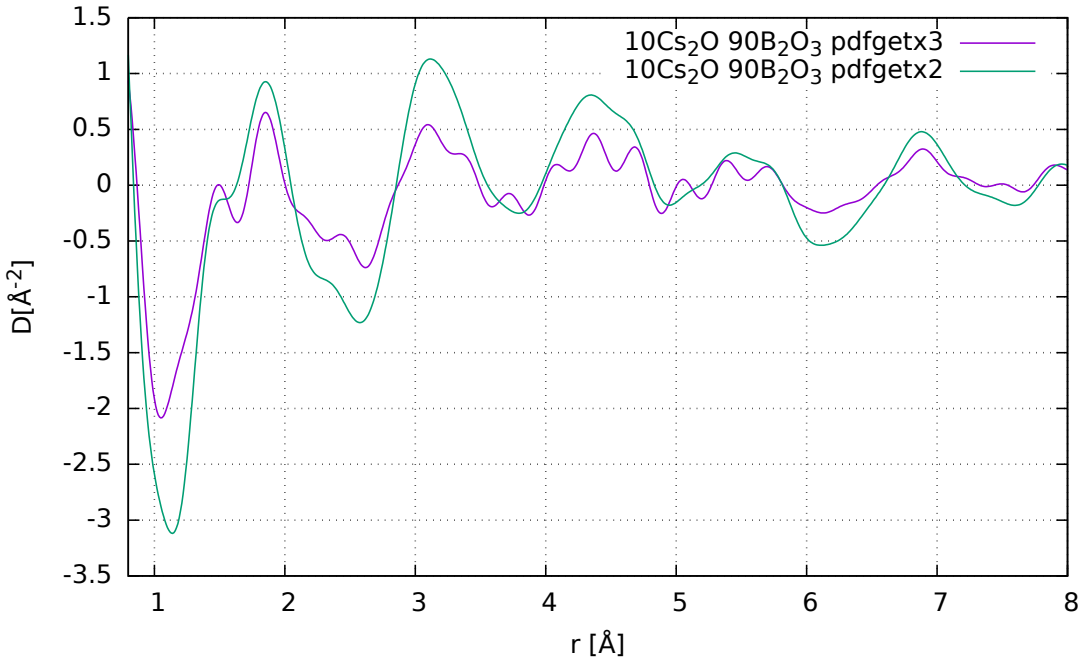

Figure 4.44: Comparison between the evaluations of $D(r)$ of $10Cs_2O\ 90B_2O_3$ with PDFgetX2 and PDFgetX3.

Chapter 5

Conclusion and outlook

In this work the structure of alkali borate glass was characterized by examining a full spectrum of alkali borate samples from lithium borate to caesium borate with different alkali concentrations.
The first coordination number, which for disordered or partly disordered systems means the average of nearest neighbours, $\bar{n}_{\mathrm{B}}^{\mathrm{O}}$, respectively $\bar{n}_{\mathrm{O}}^{\mathrm{B}}$, was determined and guides us to the insight that heavier ions are responsible for a decrease of the coordination number. When increasing the alkali concentration the shift to higher r-values of the first peak in the PDF diagram is visible, which indicates the formation of BO_4 molecules. However, the coordination number almost stays the same assuming BO_4 tetrahedrons arise as likely as BO_2 structures.
It was also shown that the highly automatable PDFgetX3 software turned out to be inappropriate for evaluating the intensity $I(q)$ from X-ray diffraction measurements in transmission geometry of alkali borate powder capillary samples or bulk samples. Only the peak positions have physical meaning and coincide with PDFgetX2 evaluations and literature. Peak heights, however, were utterly misinterpreted by PDFgetX3 leading to too small coordination numbers.
The entire knowledge of the scattering theory, the chemical compositions of the samples and the experimental setup is necessary to understand the upcoming corrections, normalization factors, damping-, and optimization functions that have to be set for an optimal application of PDFgetX2 and an optimal output of the *Faber-Ziman* structure factor, the reduced structure factor, the density function and the PDF.
Theoretically it is essential to understand that a full structural deciphering of a polyatomic system is not possible (or at least very elaborate) to access if only experimental data exist. Numerical evaluations are able to distinguish between different atomic types and thus are able to determine the partial structure factors and the partial PDFs. Combining the experimental data with the numerical ones on which our group is permanently working on, will complete the examination of the alkali borate structure.
Due to the hygroscopic property of alkali borate glasses, we also learned that preparing powder capillary samples, despite all the care taken excluding the atmosphere during the manufacturing steps, is not worthwhile. The more surface the specimen is offering, the more crystalline structures are able to emerge, which impairs the

experimental results. On that account, we think that preparing bulk samples in the case of $x\mathrm{A_2O}$ $(100-x)\mathrm{B_2O_3}$ is more appropriate. They offer less surface and are easier to manufacture.

In the future our group will foucs on diffusion processes of alkali borate glasses (and other kinds of glasses). Via aXPCS (atomic-scale X-ray Photon Correlation Spectroscopy) measurements we will obtain the so-called correlation time τ_{exp}, which relates to the diffusion constant D [29]:

$$\tau_{\mathrm{exp}}^{-1} = q^2 D. \tag{5.1}$$

Besides the aXPCS experiments our group is working on a theoretical model of the correlation time τ_{model} that predicts the relation [19]:

$$\tau_{\mathrm{exp}}^{-1} = \frac{\tau_{\mathrm{model}}^{-1}}{S_{\mathrm{FZ}}(q)}. \tag{5.2}$$

Hence, the *Faber-Ziman* structure factor $S_{\mathrm{FZ}}(q)$ is required, which is now already well-elaborated in this thesis.
The diffusion constant D is furthermore correlated with the conductivity σ via the *Nernst-Einstein* equation [2]:

$$D = \frac{\sigma k_{\mathrm{B}} T}{z_{\mathrm{A}} \rho_0}, \tag{5.3}$$

where k_{B} is the Boltzmann constant, T the temperature, z_{A} the ionic charge and ρ_0 the number density.
We will also perform conductivity measurements and compare both results.

Eventually it is important to state that the full knowledge of the structure and the diffusion process is an essential requirement of manufacturing optimal alkali borate glasses with a maximum of power for technological applications.

Appendix A

Derivation of the Archimedes' method

Due to the complex shapes of the glass samples a straightforward volume determination is not feasible. Hence, the Archimedes' method for determining the density was applied.

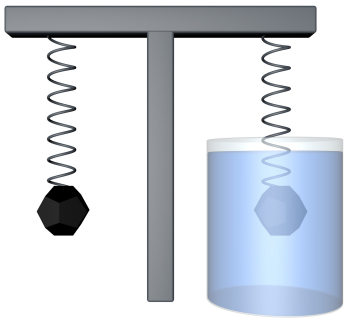

Figure A.1: Illustration of the Archimedes' method. The sample is weighted in air and in liquid.

Based on Archimedes' method (see figure A.1), a glass sample was measured twice: In air and in a liquid with unknown density ρ_l. In our case we used decahydronaphthalene[1], which exhibits low surface tension.
The balance measures the difference between the weight force and the lift force:

$$F_\mathrm{sl} = m_\mathrm{s} g - F_\mathrm{ll}. \tag{A.1}$$

F_sl is the actual measured weight force of the sample in liquid, m_s is the mass of the sample and F_ll is the lift force of the sample in liquid.
During the measurement it is necessary to bring the sample in a stable condition: On a balance a suspension device was prepared, which holds the sample on a nylon thread. The sample was then carefully immersed in a glass beaker filled with decahydronaphthalene. If it does not hover in the liquid we had to change the size of the glass sample.

[1] $C_{10}H_{18}$ (decahydronaphthalene), mixture of cis and trans, 98%.

According to Archimedes' principle the lift force F_{ll} is equal to the volume of the displaced liquid V_{dl} multiplied with the density of the liquid ρ_{l} and the gravitational acceleration g:

$$F_{\mathrm{sl}} = m_{\mathrm{s}}g - V_{\mathrm{dl}}\rho_{\mathrm{l}}g. \tag{A.2}$$

The volume of the sample V_{s} equals to the volume of the displaced liquid V_{dl} and because of $V_{\mathrm{s}} = \frac{m_{\mathrm{s}}}{\rho_{\mathrm{s}}}$ equation A.2 changes to:

$$F_{\mathrm{sl}} = m_{\mathrm{s}}g\Big(1 - \frac{\rho_{\mathrm{l}}}{\rho_s}\Big). \tag{A.3}$$

For a higher accuracy the measurement in air requires the same considerations as above:

$$F_{\mathrm{sa}} = m_{\mathrm{s}}g - F_{\mathrm{la}}. \tag{A.4}$$

F_{sa} is the actual measured weight force of the sample in air and F_{la} is the lift force of the sample in air.
Following the same steps from equation A.2 to equation A.3 yields to:

$$F_{\mathrm{sa}} = m_{\mathrm{s}}g\Big(1 - \frac{\rho_{\mathrm{a}}}{\rho_{\mathrm{s}}}\Big). \tag{A.5}$$

The density of air is $\rho_{\mathrm{a}} = 0.001251\,\mathrm{g/cm^3}$ in accordance with $20°C$ room temperature and 180 m over sea level (location: university of Vienna/physics department).
Combining both equations A.3 and A.5 gives:

$$\frac{F_{\mathrm{sa}}}{1 - \frac{\rho_{\mathrm{a}}}{\rho_{\mathrm{s}}}} = \frac{F_{\mathrm{sl}}}{1 - \frac{\rho_{\mathrm{l}}}{\rho_{\mathrm{s}}}}$$

$$\rho_{\mathrm{s}} = \frac{F_{\mathrm{sa}}\rho_{\mathrm{l}} - F_{\mathrm{sl}}\rho_{\mathrm{a}}}{F_{\mathrm{sa}} - F_{\mathrm{sl}}}. \tag{A.6}$$

The balance measures the masses m_{sa} and m_{sl} of the sample in air and in liquid and not the weight forces. Due to $F_{\mathrm{sa}} = m_{\mathrm{sa}}g$ and $F_{\mathrm{sl}} = m_{\mathrm{sl}}g$ equation A.6 turns to:

$$\rho_{\mathrm{s}} = \frac{m_{\mathrm{sa}}\rho_{\mathrm{l}} - m_{\mathrm{sl}}\rho_{\mathrm{a}}}{m_{\mathrm{sa}} - m_{\mathrm{sl}}}. \tag{A.7}$$

The unknown density of the liquid ρ_{l} is calculated by a reference densitiy of silicon $\rho_{\mathrm{si}} = 2.336\,\mathrm{g/cm^3}$, hence the density of liquid ρ_{l} can be determined by rearranging equation A.7:

$$\rho_{\mathrm{l}} = \frac{\rho_{\mathrm{si}}\,(m_{\mathrm{sa}} - m_{\mathrm{sl}}) + m_{\mathrm{sl}}\rho_{\mathrm{a}}}{m_{\mathrm{sa}}} \tag{A.8}$$

From equation A.7 the following density results were calculated:

sample	density ρ [g/cm^3]	sample	density ρ [g/cm^3]
$5Li_2O\,95B_2O_3$	1.90 ± 0.02	$20Li_2O\,80B_2O_3$	2.117 ± 0.003
$5Na_2O\,95B_2O_3$	1.984 ± 0.002	$20Na_2O\,80B_2O_3$	2.199 ± 0.004
$5K_2O\,95B_2O_3$	1.95 ± 0.02	$20K_2O\,80B_2O_3$	1.990 ± 0.002
$2RB_2O\,98B_2O_3$	1.979 ± 0.002	$15RB_2O\,85B_2O_3$	2.395 ± 0.004
$2Cs_2O\,98B_2O_3$	1.929 ± 0.005	$10Cs_2O\,90B_2O_3$	2.364 ± 0.003
$15Cs_2O\,85B_2O_3$	2.544 ± 0.006		

Table A.1: Measured densities ρ of glass samples in $[g/cm^3]$.

Bibliography

[1] LV Azaroff, R Kaplow, N Kato, RJ Weiss, AJC Wilson, and RA Young. X-ray diffraction, 1974.

[2] Frank Berkemeier, Stephan Voss, Árpád W Imre, and Helmut Mehrer. Molar volume, glass-transition temperature, and ionic conductivity of na-and rb-borate glasses in comparison with mixed na–rb borate glasses. *Journal of non-crystalline solids*, 351(52):3816–3825, 2005.

[3] Frank Hugo Berkemeier. Ionenleitende borat-und silikatglasschichten. 2008.

[4] Simon JL Billinge and Christopher L Farrow. Towards a robust ad hoc data correction approach that yields reliable atomic pair distribution functions from powder diffraction data. *Journal of Physics: Condensed Matter*, 25(45):454202, 2013.

[5] Stefan Blugel. A 2 scattering theory: Born series. 2012.

[6] PJ Brown, AG Fox, EN Maslen, MA O'Keefe, and BTM Willis. *Intensity of diffracted intensities*. Springer, 2006.

[7] A-C Dippel, H-P Liermann, Jan Torben Delitz, Peter Walter, Horst Schulte-Schrepping, Oliver H Seeck, and Hermann Franz. Beamline p02. 1 at petra iii for high-resolution and high-energy powder diffraction. *Journal of synchrotron radiation*, 22(3):675–687, 2015.

[8] Takeshi Egami and Simon JL Billinge. *Underneath the Bragg peaks: structural analysis of complex materials*, volume 16. Elsevier, 2003.

[9] Christopher L Farrow and Simon JL Billinge. Relationship between the atomic pair distribution function and small-angle scattering: implications for modeling of nanoparticles. *Acta Crystallographica Section A: Foundations of Crystallography*, 65(3):232–239, 2009.

[10] Henry E Fischer, Adrian C Barnes, and Philip S Salmon. Neutron and x-ray diffraction studies of liquids and glasses. *Reports on Progress in Physics*, 69(1):233, 2005.

[11] Brent Fultz and James M Howe. *Transmission electron microscopy and diffractometry of materials*. Springer Science & Business Media, 2012.

[12] GN Greaves and S Sen. Inorganic glasses, glass-forming liquids and amorphizing solids. *Advances in Physics*, 56(1):1–166, 2007.

[13] Rudolf Gross and Achim Marx. *Festkörperphysik*. Walter de Gruyter GmbH & Co KG, 2014.

[14] Yasuhiko Iwadate, Kazuo Igarashi, Takeo Hattori, Shin Nishiyama, Kazuko Fukushima, Junichi Mochinaga, Naoki Igawa, and Hideo Ohno. Short range structure of b2o3–cs2o glasses analyzed by x-ray diffraction and raman spectroscopy. *The Journal of chemical physics*, 99(9):6890–6896, 1993.

[15] Pavol Juhás, Timur Davis, Christopher L Farrow, and Simon JL Billinge. Pdfgetx3: a rapid and highly automatable program for processing powder diffraction data into total scattering pair distribution functions. *Journal of Applied Crystallography*, 46(2):560–566, 2013.

[16] Junichi Kawamura, Ryo Asayama, Naoaki Kuwata, and Osamu Kamishima. Ionic transport in glass and polymer: Hierarchical structure and dynamics. *Phys. Solid State Ionics*, pages 193–246, 2006.

[17] H Kenmotsu, T Hattori, S Nishiyama, K Fukushima, Y Iwadate, M Misawa, T Fukunaga, T Nakazawa, and K Noda. Short range structure of b 2 o 3–rb 2 o glasses by neutron diffraction. *Journal of Physics and Chemistry of Solids*, 60(8):1461–1464, 1999.

[18] James N Lapherty. *New trends in chemical physics research*. Nova Science Publ., 2011.

[19] Michael Leitner. *Studying atomic dynamics with coherent X-rays*. Springer Science & Business Media, 2012.

[20] HA Levy, MD Danford, and AH Narten. Data collection and evaluation with an x-ray diffractometer designed for the study of liquid structure. Technical report, Oak Ridge National Lab., Tenn., 1966.

[21] R_ L Mozzi and BE Warren. The structure of vitreous boron oxide. *Journal of Applied Crystallography*, 3(4):251–257, 1970.

[22] CJ Pings and J Waser. Analysis of scattering data for mixtures of amorphous solids or liquids. *Journal of Chemical Physics*, 48:3016–3018, 1968.

[23] Xiangyun Qiu, Jeroen W Thompson, and Simon JL Billinge. Pdfgetx2: a gui-driven program to obtain the pair distribution function from x-ray powder diffraction data. *Journal of Applied Crystallography*, 37(4):678–678, 2004.

[24] Konrad Sagel. *Tabellen zur Röntgenstrukturanalyse*, volume 8. Springer-Verlag, 2013.

[25] A Takada, CRA Catlow, and GD Price. 'computer synthesis' of b2o3 polymorphs. *Physics and Chemistry of Glasses*, 44(2):147–149, 2003.

[26] Christoph Tietz. *Investigation of the structure of lithium borate ionic glasses*. 2015.

[27] AH Verhoef and HW Den Hartog. A molecular dynamics study of b 2 o 3 glass using different interaction potentials. *Journal of non-crystalline solids*, 146:267–278, 1992.

[28] AH Verhoef and HW Den Hartog. Structure and dynamics of alkali borate glasses: a molecular dynamics study. *Journal of non-crystalline solids*, 182(3):235–247, 1995.

[29] Stefan Will and Alfred Leipertz. Determination of the dynamic viscosity of transparent fluids by using dynamic light scattering. *Applied optics*, 32(21):3813–3821, 1993.

[30] G Zhang, FH Stillinger, and S Torquato. The perfect glass paradigm: Disordered hyperuniform glasses down to absolute zero. *Scientific Reports*, 6, 2016.

Abbreviations

AXS Anomalous X-ray Scattering

BMH Born-Mayer-Huggins

BO Bridging Oxygen

EXAFS Extended X-ray Absorption Fine Structure

MAS-NMR Magic Angle Spinning Nuclear Magnetic Resonance

MC Monte Carlo

MD Molecular Dynamics

NBO Non-Bridging Oxygen

NDIS Neutron Diffraction Isotopic Substitution

NMR Nuclear Magnetic Resonance

RDF Radial Distribution Function

RMC Reverse Monte Carlo

SAXS Small-Angle X-ray Scattering

SRO Short-Range Order

WAXS Wide-angle X-ray Scattering

Danksagung

An diesem Punkt möchte ich mich bei meinem Betreuer Bogdan Sepiol bedanken, der mich für dieses Projekt ausgesucht hat und mir jederzeit mit Rat und Tat zur Seite gestanden ist.
Ein großer Dank gebührt auch Christoph Tietz, der mir sowohl bei den theoretischen und experimentellen Fragen als auch beim Korrekturlesen der Masterarbeit zur Verfügung stand. Durch seine Vorkenntnisse wurde mir der Einstieg in das Thema leichter gemacht und ich fühlte mich das Jahr über sehr gut aufgehoben.
Weiters bedanke ich mich bei Stephan Puchegger für den wertvollen technischen Support, bei Yvonne Simon für ihr administratives Knowhow und bei Herwig Peterlik, unserem Gruppenleiter, der unschätzbar viel für und rund um die Gruppe erledigt.
Es war ein sehr spannendes, lehrreiches Jahr, das nun letzten Endes diese Masterarbeit hervorgebracht hat, die ohne die großartige Unterstützung unserer gesamten Gruppe nicht zustande gekommen wäre.